TAMPEREEN TEKNILLINEN YLIOPISTO
TAMPERE UNIVERSITY OF TECHNOLOGY

Piotr Ryczkowski

Novel Interferometric and Correlation Optical Imaging Techniques

Julkaisu 1417 • Publication 1417

Tampere 2016

Tampereen teknillinen yliopisto. Julkaisu 1417
Tampere University of Technology. Publication 1417

Piotr Ryczkowski

Novel Interferometric and Correlation Optical Imaging Techniques

Thesis for the degree of Doctor of Science in Technology to be presented with due permission for public examination and criticism in Konetalo Building, Auditorium K1702, at Tampere University of Technology, on the 28th of September 2016, at 12 noon.

Tampereen teknillinen yliopisto - Tampere University of Technology
Tampere 2016

ISBN 978-952-15-3815-5 (printed)
ISBN 978-952-15-3821-6 (PDF)
ISSN 1459-2045

To Joanna

Abstract

The ability to image objects with high precision is central to our every-day life and to the progress in understanding of fundamental phenomena. It is thus natural that a wide range of imaging techniques have been the subject of intense research and developments in the past decades. Whilst imaging is generally thought from the spatial domain perspective, imaging or detecting ultra fast time-varying signals is also of prime importance. This work reports on novel, proof-of-concept, optical imaging techniques both in the spatial and time domains. All the proposed techniques are experimentally validated and their current limitations discussed. It is expected that the work presented in this thesis will open up new perspectives and opportunities for high precision imaging of objects as well as the detection of ultrafast waveforms.

High in-depth precision optical imaging in the spatial domain relies on indirect phase measurements. Measurements are typically performed using interferometric techniques where the phase of a light wave that has interacted with the object to be imaged is compared with a reference wave. Interferometric detection can be carried out either in the time domain where the reference wave is delayed in time between subsequent data acquisition points, or in the frequency domain where the relative phase of different frequency components is recorded. Both techniques have advantages but they are intrinsically limited by several factors, such as dispersion which limits the overall resolution or long acquisition times which prevent imaging of fast moving objects.

Stroboscopic white-light interferometry is a technique that enables precise three-dimensional (3D) measurements of rapidly oscillating objects. The recent development of high speed micromechanical machines calls for the need of precise and fast measurement techniques enabling performance and quality control. In this work, we report on a new supercontinuum light source with tunable repetition rate enabling stroboscopic measurements with nanometer accuracy of objects oscillating at speeds in excess of MHz frequencies.

Optical coherence tomography is another powerful 3D imaging technique widely employed for biological imaging. The axial resolution of conventional optical coherence tomography is limited by the spectral bandwidth of the light source and the dispersion of optical components and/or of the sample under test. In this work we demonstrate the novel concept of intensity-based optical coherence tomography using a classical

broadband light source and a Mach-Zehnder interferometer. The technique exhibits built-in even-order dispersion cancellation and a point spread function with reduced full-width at half maximum compared to standard optical coherence tomography.

Ghost imaging uses the correlation between spatially incoherent light scattered by an object and the spatially-resolved intensity pattern of the incident light to construct a ghost image of the original object. The unique aspect of ghost imaging is that an accurate image of the object can be obtained from the correlation, despite the fact that neither of the single measurements carry any meaningful information about the object. The concept of ghost imaging has been truly influential in the past few years. Originally developed to test the Einstein-Podolsky-Rosen paradox using entangled photon sources, the concept has been expanded to classical light sources and impacted on many fields and applications such as, microscopy, compressive sensing, and imaging in the presence of turbulence or high loss. We transpose the concept of ghost imaging into the time domain to produce the image of an ultrafast signal by correlating in time the intensity of two light beams, neither of which independently carried information about the signal. We further demonstrate a method based on the dispersive Fourier transform of an incoherent supercontinuum to generate a magnified ghost image of an ultrafast waveform, allowing to improve significantly the temporal resolution of imaging in the time-domain.

Preface

This work was carried out in the Optics Laboratory of the Tampere University of Technology during the years 2010-2016. I would like to acknowledge the financial support form Graduate School of Modern Optics and Photonics, Tekniikan edistämissäätiö foundation and Academy of Finland.

I would like thank my supervisor Goëry Genty for allowing me to start my scientific carrier in Optics Laboratory. I am really grateful for the amount of trust he placed in me, guidance and support. Only his unmeasured enthusiasm, motivating for bigger effort, and great amount of patience allowed me to carry this work till the end.

I would like to express my gratitude to prof. Edvard Hæggström dr. Ivan Kassamakov and Anton Nolvi from Helsinki University of technology, whose group helped me to carry out first measurements and to prof. Ari Friberg, from the University of Eastern Finland, whose theoretical work was a base to my later experiments.

I would like to thank Margaux for her help in experimental and reporting work, Juha and Johan for so-needed electronic advisory and Antti, who started the infrared supercontinuum light source project in our laboratory. I am grateful for endless discussions kept with Mariusz, Alessandro, Kalle, my room-mates Hanu, Mikko and Robert who always was an oasis of tranquillity and reason in the laboratory. I am happy to have been able to spend all those years with good spirited Godofredo and team leading Caroline. Thank you Leo and Samu for weekly badminton games which I was let to win only once.

Finally I would like to thank my wife Joanna for supporting me through all the years.

Tampere, April 2016

Piotr Ryczkowski

Contents

List of Figures

List of Publications

Paper 1 P. Ryczkowski, A. Nolvi, I. Kassamakov, G. Genty, and E. Hæggström. High-speed stroboscopic imaging with frequency-doubled supercontinuum. Optics Letters, **38**, 658 (2013).

Paper 2 P. Ryczkowski, J. Turunen, A. T. Friberg, and G. Genty. Experimental Demonstration of Spectral Intensity Optical Coherence Tomography. Scientific Reports, **6**, 22126 (2016).

Paper 3 P. Ryczkowski, M. Barbier, A. T. Friberg, J. M. Dudley, and G. Genty. Ghost imaging in the time domain. Nature Photonics, **10**(3), 167–170 (2016).

Paper 4 P. Ryczkowski, M. Barbier, A. T. Friberg, J. M. Dudley, and G. Genty. Magnified Time-Domain Ghost Imaging. submitted to Optica.

Nomenclature

x, y, z	Cartesian coordinates
3D	Three-dimensional
$A(\omega)$	Complex amplitude in spectral domain
$\hat{\boldsymbol{A}}$	Angular spectrum complex amplitude
$\boldsymbol{A}$	Electric field amplitude in complex notation
A-scan	Signle in-dpeth line interferometric scan
B-scan	Cross-sectional interferometric scan of the sample
$\widetilde{\boldsymbol{B}}$	Magnetic induction vector
Cor	Correlation
Cov	Covariance
$C(t)$	Correlation function
$\widetilde{\boldsymbol{D}}$	Electric displacement vector
$\widetilde{\boldsymbol{E}}$	Electric field vector
FWHM	Full width af half maximum
GVD	Group Velocity Dispersion
$\widetilde{\boldsymbol{H}}$	Magnetic field vector
I	Light intensity
IOCT	Intensity Optical Coherence Tomography
$I_{\mathrm{ref}}(t)$	Recorded intensity of a reference beam
I_{test}	Bucket detector signal

$\widetilde{\boldsymbol{J}}$	Electric free current density vector
LED	Light emitting diode
$\widetilde{\boldsymbol{M}}$	Material magnetization vector
N	Number of measurement realizations
OCT	Optical Coherence Tomography
$\widetilde{\boldsymbol{P}}$	Material polarization vector
$S(\omega)$	Spectral intensity (Spectrum) of the light
SHG	Second Harmonic Generation
SMF	Single-mode fiber
SNR	Signal to noise ratio
SOCT	Spectral-domain optical coherence tomography
SWLI	Stroboscopic White Light Interferometry
$SE(\dots)$	Standard error
$T_D(t)$	Temporal response function fo a photodetector
TGI	Temporal Ghost Imaging
$T_{obj}(t)$	Transmission of the temporal object
$T_S(t)$	Fourier transform of a light source spectrum
$I_{\mathrm{src}}(t)$	Source temporal intensity
Var	Variance
WLI	White Light Interefometry
c	Speed of light in vacuum
c.c.	Complex conjugate
$g^{(1)}$	First order coherence function
i	Immaginary unit $\sqrt{-1}$
$\boldsymbol{k}$	Wave vector
n	Refractive index
t	Time
$\beta^{(m)}$	M-th order dispersion coefficient

χ_e	Electric susceptibility
χ_m	Magnetic susceptibility
$\frac{\partial}{\partial x}$	Partial derivative with respect to the x-parameeter
ϵ	Medium electric permittivity
ϵ_0	Vacuum electric permittivity
λ	Wavelenght in a given medium
λ_0	Wavelenght in vacuum
μ	Medium magnetic permeability
μ_0	Vacuum magnetic permeability
ω	Angular frequency
ω_0	Center angular frequency, carrier frequency
ρ	Electric free charge density
τ	Time-delay

Chapter 1

Introduction

Optics has played a major role in our lives over the last centuries. Every major discovery in the field has changed our understanding of the world around us: telescopes have transformed our perception of the universe, microscopes have revolutionized biology and medicine, the spectral analysis of a black body has led to the development of quantum physics which explains the nature of matter and energy at the atomic scale and forms the basis of modern physics. Light sources such as light emitting diodes (LED) and lasers are ever increasingly present in medicine [1], telecommunication, industrial production [2], sensing and metrology [3,4].

The human eye has a limited accuracy and the ability to produce images of objects with a high precision is important to advances in many domains of research. A wide range of imaging techniques have been developed either in the form of direct methods where light scattered from and object is detected with a photodetector (or an array of photodetectors) combined with an imaging system to resolve fine details of the object, or in the form of indirect methods where the interference pattern generated from the light scattered by the object and a reference beam allows to reconstruct an image with high accuracy. In general, the resolution of direct imaging techniques is limited by diffraction to half of the wavelength of the light source employed whereas interferometric methods can be significantly more accurate and precision at the nanometer scale can be achieved. Besides precision, speed is another important characteristics of imaging techniques which determines the types of moving objects that can be imaged.

White light Interferometry (WLI) and Optical Coherence Tomography (OCT) are two interferometric techniques that are widely used to obtain images with high resolution.

WLI is often used for the characterization of mechanical elements[5–10], for which it offers a fast and precise quality control with the possibility of scanning a broad area in a short time. OCT is commonly employed for biological and medical applications[11–15] as it allows resolution imaging of living tissue at the micrometer scale without the need of using contrast chemicals or dye injections. Both techniques offer the possibility to create high resolution three-dimensional (3D) image of an object. The lateral resolution is determined by the numerical aperture of the optical system. The in-depth scan resolution on the other hand depends on the light source parameters, sources with higher brightness and broader bandwidth enabling more sensitive and precise detection. Yet, in this case, dispersion which reflects the dependence of the refractive index of a material on the wavelength of light can limit the performance. The development of light sources with tailored characteristics and techniques to limit the influence of dispersion are thus important to improve the longitudinal precision of interferometric measurement techniques. Extending the measurement capabilities of interferometric methods to rapidly moving objects is also of significant interest for many practical applications.

Whilst imaging techniques are generally envisaged from the spatial domain perspective to measure the physical dimensions of an object, imaging phenomena that occur on short time scales is also very important. For example, ultra-fast light intensity variations, emission decay rates, fluorescence, absorption or transmission changes within a medium can all be probed and measured with light. In this case, the temporal resolution of the imaging scheme depends on the properties of the light source and characteristics of the photodetectors that are used. Whilst direct detection techniques using high speed photodetectors are most commonly used, they typically fail when the signal to be imaged is severely distorted due to the presence of strong attenuation, dispersion, or nonlinearity. Furthermore, because the speed of currently available electronics is limited, the temporal resolution may not be sufficient and detailed temporal variation not fully captured. There is thus a need to develop imaging techniques capable of both restoring signals that have been distorted and allowing for magnifying or stretching waveforms in time to enable the use of standard electronics.

1.1 Aim and Scope of This Work

The overall rationale behind this thesis is to design and perform experiments validating new concepts, alternative to current existing techniques, in optical imaging, both in the spatial and in the time domain. The first goal of this work is to develop a broadband light source for interferometric measurements. It is characterized by unique capability of on demand generation of short, powerful pulses, that makes it a particularly promising light source for stroboscopic white light interferometry. The motivation is to develop a cost-effective, robust device which can easily be to operated and maintained. The source should allow to reach manometer level precision for measurements of samples oscillating at a broad range of frequencies from sub kHz to single MHz. A source of this kind can find applications in fast, non-contact product testing and quality control of imaging micro-electromechanical machines. The second objective is to experimentally test a newly proposed intensity correlation measurement technique with built-in dispersion cancellation and increased density of points in the image. Both theoretical claims are tested in proof-of-concept experiments. The technique is an alternative approach to existing dispersion handling methods, opening new possibilities for ultra-high precision imaging of biological samples with broadband interferometric techniques. The last aim is to transfer the concept of ghost imaging from the spatial to the temporal domain by using the space-time duality of light propagation. In the ghost imaging measurement the total amount of light transmitted through the temporal object is correlated with the temporal intensity of the light source in order to create the image. Such a set-up is insensitive to any time-related distortions present between the object and the detector. The objective is to experimentally demonstrate, for the first time, the possibilities of ghost imaging scheme in the time domain and show its capability for measuring ultra-fast time-varying waveforms. A study of implementing temporal magnification in to the measurement scheme, for increased image resolution, is also provided.

1.2 Structure of the Thesis

This work consist of six chapters allowing to understand the basics of interferometric and correlation imaging techniques and describe the obtained results.

Chapter 2 describes the basic concepts of linear optics and introduces the naming convention used in subsequent chapters. A brief description of dispersion and nonlinear effects is also given.

Chapter 3 introduces white light interferometry. The coherence properties of light are discussed and example of light sources used for white light interferometry are presented. The possibility of imaging oscillating objects through stroboscopic white light interferometry is then discussed and experimental demonstration using a tailored supercontinuum source is reported.

In Chapter 4, we present the operating principle of Optical Coherence Tomography in the spectral domain. Modification of the technique in the form of Intensity Optical Coherence Tomography is subsequently described, its benefits and experimental performance are discussed.

In Chapter 5 the concept of Ghost Imaging in the time-domain is described and demonstrated. Different configurations are discussed together with experimental constraints. An approach to magnify the temporal object to be imaged is also presented.

Chapter 6 summarizes the results obtained and suggest future perspectives.

1.3 Author's Contribution

This thesis consists of a number of publications which introduce novel optical imaging techniques in the spatial and temporal domains. A short description of each publication along with the author's contribution is provided below.

Paper 1 This paper demonstrates the experimental realization of Stroboscopic While Light Interferometry using a frequency-doubled supercontinuum light source with tunable repetition rate. The continuously-tunable repetition rate and short duty cycle of the broadband pulsed source, combined with proposed sub-harmonic laser triggering allow high precision measurements of microelectromechanical systems oscillating at MHz frequencies. The author contributed to the experimental demonstration by developing, testing and implementing the light source used in the interferometric characterization setup. The author also proposed the sub-harmonic triggering measurement scheme and contributed to the experiment performed in collaboration with the University of Helsinki. He took the leading role in the manuscript preparation.

Paper 2 This paper reports on the first experimental demonstration of Intensity Optical Coherence Tomography, validating the theoretically predicted benefits of the technique: second-order dispersion cancellation and point spread function with reduced width. An approach to eliminate the presence of artefacts in the image in the case of multiple interfaces is also demonstrated. The author designed and constructed the experimental setup, performed all the measurements and data analysis. He took the leading role in reporting and contributed to the manuscript preparation.

Paper 3 In this paper first experimental demonstration of the Ghost Imaging in time domain is presented. The correlation between incoherent source intensity fluctuations, measured by fast detector and the total light transmitted through the temporal object, measured by slow detector, is used to generate the ghost image. The insensitivity of the technique to signal distortions is presented with the example of significant modal dispersion introduced in the system. The author designed and constructed the experimental setup, performed the measurements and analyzed the data together with co-workers. He also took a significant role in reporting.

Parer 4 In this paper an experimental demonstration of Temporal Ghost Imaging with 5-time magnification is reported. The magnification scheme is based on the tem-

poral equivalent of shadow imaging, using frequency-to-time conversion of the spectral fluctuations of an incoherent supercontinuum light source. The author proposed the concept, and designed and constructed the experimental setup. He performed the measurements and took significant role in the data analysis and participated in results reporting.

The results obtained in this work are the product of collaborations and team effort. The author's contribution to each of the Papers is presented in Table 1.1. The contribution is divided into three categories; **Preparation**, **Experiments**, and **Reporting**. Preparation consists of theory, design and evaluation of the experimental method, experiments includes the implementation of the experimental method and the actual experimental work. Reporting contains the data analysis and the preparation of the manuscript.

Table 1.1.: Summary of author's contribution to articles included in this Thesis.

Paper	Preparation	Experiments	Reporting
Paper 1	90%	50%	80%
Paper 2	80%	100%	70%
Paper 3	90%	80%	50%
Paper 4	100%	70%	30%

Chapter 2

Light Propagation in Matter

Light is an electromagnetic wave[16,17] of wavelengths spreading from about 10 nm deep UV to 1 mm of far infrared and corresponding frequency span from 30 PHz to 300 MHz. The visible part of the light spectrum is much narrower starting at about 400 nm (blue) and ending at 700 nm (red). Propagating electromagnetic waves can interact with surrounding mater in a variety of ways. A light beam can be attenuated or amplified, diffracted, dispersed or even change its frequency due to nonlinear effects. In this chapter the basics of light propagation are introduced using a classical formalism that is suitable for understanding the following chapters of this thesis.

2.1 Maxwell equations

Electromagnetic forces are one of the four fundamental interactions known to exist in nature. The interaction of the electric field $\widetilde{\boldsymbol{E}}$ and magnetic induction $\widetilde{\boldsymbol{B}}$, associated with a light beam, and interacting with a surrounding medium is governed by

Maxwell's equations:

$$\nabla \cdot \widetilde{\boldsymbol{E}} = \frac{1}{\epsilon_0}\rho_{total} \tag{2.1}$$

$$\nabla \cdot \widetilde{\boldsymbol{B}} = 0 \tag{2.2}$$

$$\nabla \times \widetilde{\boldsymbol{E}} = -\frac{\partial \widetilde{\boldsymbol{B}}}{\partial t} \tag{2.3}$$

$$\nabla \times \widetilde{\boldsymbol{B}} = \mu_0 \left(\widetilde{\boldsymbol{J}}_{total} + \epsilon_0 \frac{\partial \widetilde{\boldsymbol{E}}}{\partial t} \right) \tag{2.4}$$

where $\widetilde{\boldsymbol{J}}_{total}$ is the electric current density of all present charged particles , $\widetilde{\rho}_{total}$ is the total electric charge density, and ϵ_0 and μ_0 are the electric permittivity and the magnetic permeability of vacuum, respectively. The vectorial differential operator ∇ is defined as $\nabla = \left(\frac{\partial}{\partial x}, \frac{\partial}{\partial y}, \frac{\partial}{\partial z}\right)$, where x, y and z are Cartesian space coordinates. The "$\cdot$" is the scalar product and "$\times$" is the vectorial product. The time coordinate is noted by t. Both the electric and the magnetic field vary in time and space interacting with charges present in the medium modifying and being modified by their densities.

Macroscopic description

Solving Maxwell equations in the above form generally requires to include all the charges and currents in the medium. To simplify the problem, an approximated macroscopic response of the material can be included in the form of a polarization vector $\widetilde{\boldsymbol{P}}$ and a magnetization vector $\widetilde{\boldsymbol{M}}$, which describe the overall behaviour of bounded charges (electrons bounded to the atom cores and particles), such that only free charges and currents need to be dealt with separately. With this approximation Maxwell's equations can be written as:

$$\nabla \cdot \widetilde{\boldsymbol{D}} = \widetilde{\rho} \tag{2.5}$$

$$\nabla \cdot \widetilde{\boldsymbol{B}} = 0 \tag{2.6}$$

$$\nabla \times \widetilde{\boldsymbol{E}} = -\frac{\partial \widetilde{\boldsymbol{B}}}{\partial t} \tag{2.7}$$

$$\nabla \times \widetilde{\boldsymbol{H}} = \mu_0 \left(\widetilde{\boldsymbol{J}} + \frac{\partial \widetilde{\boldsymbol{D}}}{\partial t} \right) \tag{2.8}$$

where $\widetilde{\rho}$ is the electric free charge density and $\widetilde{\boldsymbol{J}}$ is the electric free current density.

The electric displacement vector $\widetilde{\boldsymbol{D}}$ is the sum of the electric field and material polarization $\widetilde{\boldsymbol{P}}$:

$$\widetilde{\boldsymbol{D}} = \epsilon_0 \widetilde{\boldsymbol{E}} + \widetilde{\boldsymbol{P}}, \tag{2.9}$$

while the magnetic field vector $\widetilde{\boldsymbol{H}}$ arises for the presence of magnetic induction and material magnetization $\widetilde{\boldsymbol{M}}$

$$\widetilde{\boldsymbol{H}} = \frac{1}{\mu_0} \widetilde{\boldsymbol{B}} - \widetilde{\boldsymbol{M}}. \tag{2.10}$$

The polarization and magnetization vectors may be complex quantities, accounting for attenuation. For linear materials with small attenuation and no free charges or currents, the polarization and magnetization vectors can be described as linear functions of the electric field and magnetic induction:

$$\widetilde{\boldsymbol{P}} = \epsilon_0 \chi_e \widetilde{\boldsymbol{E}}, \tag{2.11}$$

$$\widetilde{\boldsymbol{M}} = \chi_m \widetilde{\boldsymbol{H}}. \tag{2.12}$$

Here χ_e and χ_m represent the electric and magnetic susceptibilities - complex tensor values describing the material response to the presence of the electric and magnetic fields. With this linear approximation, the electric displacement and magnetic field can be expressed directly as a function of the electric field and magnetic induction:

$$\widetilde{\boldsymbol{D}} = \left(\epsilon_0 + \epsilon_0 \chi_e\right) \widetilde{\boldsymbol{E}} = \epsilon \widetilde{\boldsymbol{E}} \tag{2.13}$$

$$\widetilde{\boldsymbol{H}} = \frac{1}{\mu_0 + \mu_0 \chi_m} \widetilde{\boldsymbol{B}} = \frac{1}{\mu} \widetilde{\boldsymbol{B}}, \tag{2.14}$$

where ϵ and μ denoting permittivity and permeability of the medium. Substituting the polarization and magnetization vectors by their linear approximation into the Maxwell equations and assuming that there are no free charges or currents in the propagation medium (as it is the case in most dielectrics) one obtains the simplified form:

$$\nabla \cdot \epsilon \widetilde{\boldsymbol{E}} = 0 \tag{2.15}$$

$$\nabla \cdot \widetilde{\boldsymbol{B}} = 0 \tag{2.16}$$

$$\nabla \times \widetilde{\boldsymbol{E}} = - \frac{\partial \widetilde{\boldsymbol{B}}}{\partial t} \tag{2.17}$$

$$\nabla \times \frac{1}{\mu} \widetilde{\boldsymbol{B}} = \epsilon \frac{\partial \widetilde{\boldsymbol{E}}}{\partial t}. \tag{2.18}$$

Equations (2.15-2.18) govern the propagation of light in a linear medium with no free charges or currents.

Wave equation

By taking the curl of both sides of equation 2.17 and substituting $\nabla \times \widetilde{\boldsymbol{B}}$ from Eq. (2.18) the evolution of the electric field is governed by:

$$\nabla^2 \widetilde{\boldsymbol{E}} = \epsilon\mu \, \frac{\partial^2 \widetilde{\boldsymbol{E}}}{\partial t^2} \tag{2.19}$$

and similarly for the magnetic flux $\widetilde{\boldsymbol{B}}$.

Equation (2.19) is a second order differential equation with respect to time and space which describes the propagation of the electric field associated with a light wave in a linear medium. Any electric field $\widetilde{\boldsymbol{E}}$, defined in time and space that satisfies the wave equation (and all Maxwell equations) can be treated as a wave that travels with the phase velocity defined by the medium permittivity ϵ and permeability μ:

$$v = \frac{1}{\sqrt{\epsilon\mu}} = \frac{1}{n} \cdot c, \tag{2.20}$$

where $c = \frac{1}{\sqrt{\epsilon_0 \mu_0}}$ is the speed of light in vacuum and n is the refractive index of the material defined as:

$$n = \sqrt{(\chi_e + 1)(\chi_m + 1)}. \tag{2.21}$$

It is thus clear that the refractive index of a medium modifies the speed of the waves propagating through this medium. Magnetic effects are usually negligible in optical (dielectric) materials such that $\chi_m \approx 0$ and the refractive index depends only on the electric susceptibility χ_e.

Light intensity

Due to the fact that optical frequencies are too high, none of the existing detectors can measure the amplitude of light waves directly. Rather, to measure light quantitatively we utilize the fact that both the electric and magnetic fields are associated with energy which can be detected. The average density of the energy flux carried by light is

referred to as the light intensity I, a quantity that describes how much energy a light beam carries per unit of time and area. If there is more than one electromagnetic wave, they all contribute to the total recorded light intensity and their time varying fields $\widetilde{\boldsymbol{E}}_i$ have to be added, including their phase relations:

$$I = \epsilon_0 c n \left\langle \left(\sum_i \widetilde{\boldsymbol{E}}_i \right)^2 \right\rangle \tag{2.22}$$

where $\langle ... \rangle$ denote average over time.

2.2 Plane wave

The simplest solution of the wave equation (2.19) is the plane wave whose electric field representation is given by:

$$\widetilde{\boldsymbol{E}} = \boldsymbol{A'} \cos(\boldsymbol{k} \cdot \boldsymbol{r} - \omega t), \tag{2.23}$$

where $\boldsymbol{A'}$ is the amplitude of the electric field, $\boldsymbol{r}$ and t are the spatial and time coordinates. The field oscillates in time with angular frequency ω and in space with a frequency defined by the wave vector $\boldsymbol{k}$. In a homogeneous, a medium plane wave travels along the direction of the wave vector with the speed $v = \omega/k$. The amplitude of the wave vector $\boldsymbol{k}$ is determined by the wavelength λ of the wave in the medium:

$$k = \frac{2\pi}{\lambda} = \frac{2\pi}{\lambda_0/n} = \frac{n\omega}{c}, \tag{2.24}$$

where λ_0 is the wavelength that would be measured in vacuum. The plane wave can only exist in theory, as it has to be of infinite size and perfectly monochromatic. Yet, it is extremely useful to describe many practical situations, since light fields can be decomposed into a set of plane waves as described later in this chapter.

For convenience, the cosine function may be expanded in the form of complex notation:

$$\widetilde{\boldsymbol{E}} = \boldsymbol{E}(t) + \boldsymbol{E}^*(t) = \boldsymbol{A} e^{i(\boldsymbol{k}\cdot\boldsymbol{r} - \omega t)} + \boldsymbol{A^*} e^{-i(\boldsymbol{k}\cdot\boldsymbol{r} - \omega t)} = \boldsymbol{A} e^{i(\boldsymbol{k}\cdot\boldsymbol{r} - \omega t)} + c.c., \tag{2.25}$$

where $\boldsymbol{E}(t)$ is the electric field vector in complex notation. The "*" symbol denotes the complex conjugate of the quantity to which it is applied and c.c. stands for complex

conjugate of the term before the + sign. The arbitrary phase of the light wave can be included in the complex amplitude $\boldsymbol{A}$.

The correspondence between the real and complex variables requires that the absolute value of the complex amplitude is equal to the of the values the real field value:

$$\left|\widetilde{\boldsymbol{E}}\right| = 2|\boldsymbol{A}|. \tag{2.26}$$

Injecting Eq. (2.25) into the wave Eq. (2.19) leads to the Helmholtz equation that describes the evolution of the complex amplitude $\boldsymbol{A}$ associated with the electric field of a plane wave:

$$\nabla^2 \boldsymbol{A} = -k^2 \boldsymbol{A}. \tag{2.27}$$

2.3 Angular spectrum representation

A plane wave described by a wave vector $\boldsymbol{k}$ can be treated as an element of a spatial frequency base and a wave of any spatial shape and amplitude can therefore be described by a sum of plane waves. For any given electromagnetic wave amplitude $\boldsymbol{A}(x, y, z)$, defined at a plane z=0, spatial components of the spectrum can be calculated by Fourier transform:

$$\hat{\boldsymbol{A}}(k_x, k_y, z = 0) = \frac{1}{4\pi^2} \iint_{-\infty}^{+\infty} \boldsymbol{A}(x, y, z = 0) e^{i(k_x x + k_y y)}\, dx\, dy \tag{2.28}$$

where $\hat{\boldsymbol{A}}$ is the angular spectrum representation of the electromagnetic wave. The evolution of the wave propagating in $\pm z$ direction is govern by Helmholtz Eq. (2.27). The angular spectrum representation is defined in two-dimensional angular frequency space (k_x, k_y), the k_z component not given by Fourier transform is calculated as:

$$k_z = \sqrt{k^2 - k_x^2 - k_y^2}. \tag{2.29}$$

The amplitude of the spatial components can be calculated at a specific distance by propagating each spectral component. To calculate the spatial field amplitude at a

distance, each individual spectral component needs to be propagated:

$$\hat{\boldsymbol{A}}(k_x, k_y, z) = \hat{\boldsymbol{A}}(k_x, k_y, z = 0)\ e^{ik_z z}. \tag{2.30}$$

For light propagating mostly in the z direction $kz \approx k_z z$. In order to obtain the amplitude of the field at a distance z, one can simply perform the inverse Fourier transform:

$$\boldsymbol{A}(x, y, z) = \iint_{-\infty}^{+\infty} \hat{\boldsymbol{A}}(k_x, k_y, z = 0) e^{i(k_x x + k_y y + k_z z)}\, dk_x\, dk_y. \tag{2.31}$$

Substituting this result into the Helmholtz Eq. (2.27) and introducing the paraxial approximation:

$$\left|\frac{\partial^2 \boldsymbol{A}(x,y,z)}{\partial z^2}\right| << \left|\frac{\partial^2 \boldsymbol{A}(x,y,z)}{\partial x^2}\right|, \left|\frac{\partial^2 \boldsymbol{A}(x,y,z)}{\partial y^2}\right|, \left|2k\frac{\partial \boldsymbol{A}(x,y,z)}{\partial z}\right|, \tag{2.32}$$

one obtains the equation describing the free-space diffraction of a monochromatic beam

$$\frac{\partial}{\partial z}\boldsymbol{A}(x, y, z) = -\frac{i}{2k}\left(\frac{\partial^2}{\partial x^2} + \frac{\partial^2}{\partial y^2}\right)\boldsymbol{A}(x, y, z). \tag{2.33}$$

2.4 Light spectrum

The amplitude of a plane wave is constant at any point in space and time. A plane wave is characterized by a single angular frequency and oscillation frequency, it is monochromatic. The amplitude of a plane wave is constant at any point in space and time. To represent any variation in the field spatial amplitude one can superimpose several plane waves with different angular frequencies $\boldsymbol{k}$ and amplitudes $\boldsymbol{A}(\boldsymbol{k})$ as described in the previous section. If the oscillation frequency of all the plane waves is identical, the field amplitude remains constant in time. Temporal variations of the electric field amplitude $\widetilde{\boldsymbol{E}}(t)$ results from the presence of multiple spectral components $\boldsymbol{E}(\omega)$ individually associated with plane waves that add to each other, interfering depending on their relative phase and position in time. With this approach, the time varying field is just a sum of many monochromatic plane waves with different ampli-

tudes and oscillation frequencies:

$$\widetilde{\boldsymbol{E}}(t) = \sum_{\omega_i} \boldsymbol{E}(\omega_i).\cos(\omega_i t). \tag{2.34}$$

Where $\boldsymbol{E}(t)$ and ω_i are the amplitude and angular frequency associated with plane wave i. It is useful to think of a time-varying electric field as a time-dependent envelope modulating a monochromatic wave:

$$\widetilde{\boldsymbol{E}}(t) = \boldsymbol{A'}(t)\cos(\omega_0 t) = \boldsymbol{A}(t)\,\mathrm{e}^{i\omega_0 t} + \boldsymbol{A^*}\,(t)\,\mathrm{e}^{-i\omega_0 t}\,. \tag{2.35}$$

The temporal modulation imposed by the envelope $\boldsymbol{A}(t)$ is a manifestation of the presence of multiple frequencies in the electric field and the frequency spectrum can be calculated by Fourier transform:

$$\boldsymbol{E}(\omega) = \frac{1}{2\pi}\int_{-\infty}^{+\infty} \widetilde{\boldsymbol{E}}(t)e^{-i\omega t}\,dt. \tag{2.36}$$

The electric field spectrum $\boldsymbol{E}(\omega)$ is a complex value including the amplitude and phase of a given frequency component. The spectrum can also be described as the sum of two spectral amplitudes $\boldsymbol{A}(\omega)$ centred around the field carrier frequency ω_0:

$$\boldsymbol{E}(\omega) = \boldsymbol{A}(\omega-\omega_0) + \boldsymbol{A}^*(-\omega+\omega_0), \tag{2.37}$$

with

$$\boldsymbol{A}(\omega-\omega_0) = \frac{1}{2\pi}\int_{-\infty}^{+\infty} \boldsymbol{A}(t)e^{i\omega_0 t}e^{-i\omega t}\,dt. \tag{2.38}$$

Here $\boldsymbol{A}(t)$ describes the time-varying envelope that is modulating the carrier frequency. The frequency spectrum is therefore shifted by the carrier frequency ω_0. The spectral intensity $S(\omega)$ carried by each spectral component of frequency ω is proportional to the modulus squared of the amplitude of this spectral component:

$$S(\omega) = 2\epsilon_0 cn\,|A(\omega)|^2\,. \tag{2.39}$$

The factor 2 includes the fact that both $\boldsymbol{A}(\omega-\omega_0)$ and $\boldsymbol{A}^*(-\omega+\omega_0)$ contribute to the intensity. The full width af half maximum (FWHM) of the spectrum $S(\omega)$ is referred as the light spectral bandwidth.

2.5 Dispersion

The macroscopic description of light propagation in a medium accounts for the average response of all the electrons present in the medium. The strength of the interaction between the field and the electrons in the medium depends on the field frequency and increases when it is near the resonance frequency of the medium energy levels. This causes the electric susceptibility to be dependent on the type of medium and wavelength of the propagating light. The refractive index follows the changes of the electrical susceptibility, modifying the wave vector and thus the propagation speed of the wave. To deal with this problem the value of the propagation constant k can be expanded into a Taylor-series function of the angular frequency ω around the carrier frequency of the electric field ω_0:

$$k(\omega) = \beta^{(0)} + \beta^{(1)}(\omega - \omega_0) + \frac{1}{2}\beta^{(2)}(\omega - \omega_0)^2 + ... + \frac{1}{m!}\beta^{(m)}(\omega - \omega_0)^m + ..., \quad (2.40)$$

where

$$\beta^{(m)} = \left.\frac{\partial^m k}{\partial \omega^m}\right|_{\omega_0} = \beta^{(m)}(\omega_0). \quad (2.41)$$

The $\beta^{(m)}$ coefficients vary not only for different materials but also depend on the Taylor expansion center frequency and in that sense they can be treated as functions of ω_0.

Pulse propagation in a dispersive medium

A light field with a time-varying amplitude can be described by a spectrum of monochromatic waves that have a correlated phase. When a large fraction of the waves are in phase, positive interference in time occurs and one can observe a high electric field amplitude at a particular time instant. On the other hand, when waves are out of phase, they interfere destructively and the field amplitude is close to zero. Changing the phase relation between monochromatic waves leads to a change in the temporal envelope shape and its position in time. When propagating in a dispersive medium, the phase of each spectral component changes as:

$$\boldsymbol{A}(\omega - \omega_0, z) = \boldsymbol{A}(\omega - \omega_0, z = 0) \cdot e^{k(\omega)z}. \quad (2.42)$$

The different orders of $\beta^{(m)}$ have a different impact on the phase of a propagating field with a time-varying envelope. The influence of the three first dispersion orders can be easily described.

The zero-order dispersion coefficient $\beta^{(0)}(\omega_0)$ characterizes the phase velocity of the electric field, the speed at which the carrier frequency wave propagates:

$$\beta^{(0)}\left[\frac{1}{m}\right] = k|_{\omega_0} = \frac{n\omega_0}{c} = \frac{\omega_0}{v_{phase}}. \tag{2.43}$$

The first order dispersion coefficient $\beta^{(1)}(\omega_0)$ represents the linear approximation of how the phases of different frequency components are changing with respect to each other:

$$\beta^{(1)}\left[\frac{s}{m}\right] = \left.\frac{\partial\beta^{(0)}(\omega)}{\partial\omega}\right|_{\omega_0} = \left.\left(\frac{\partial n}{\partial\omega}\cdot\frac{\omega}{c} + \frac{n}{c}\right)\right|_{\omega_0} = \frac{1}{v_g}. \tag{2.44}$$

The first-order dispersion modifies the occurrence time of positive interference of spectral components and thus modifies the speed of the temporal envelope. This speed, called the group velocity v_g generally differs from that of the carrier frequency phase velocity.

One can also define the group refractive index n_g related to the group-velocity as:

$$n_g = \frac{c}{v_g} = n + \omega\cdot\frac{\partial n}{\partial\omega}. \tag{2.45}$$

The second-order dispersion coefficient $\beta^{(2)}$ is the quadratic term of the expansion which describes the linear approximation of the group-velocity variation with frequency:

$$\beta^{(2)}\left[\frac{s}{m\cdot Hz}\right] = \left.\frac{\partial\beta^{(1)}(\omega)}{\partial\omega}\right|_{\omega_0} = \frac{1}{c}\left[\frac{\partial^2 n}{\partial\omega^2}\cdot\omega + 2\frac{\partial n}{\partial\omega}\right]\Bigg|_{\omega_0}. \tag{2.46}$$

It describes the change in delay between the carrier frequency component and other spectral components per propagation distance and frequency difference. The frequency-dependence of the group velocity causes the temporal shape of the electric field envelope to change with propagation.

The dispersion parameter is also a function of frequency $\beta^{(2)}(\omega)$ and includes all the higher-order dispersion effects that can further contribute to the change of the temporal shape of the electric field envelope. The second-order dispersion, also called

the group-velocity dispersion (GVD) is often presented as a parameter D that describes dispersion as a function of wavelength:

$$D\left[\frac{s}{nm \cdot km}\right] = -\frac{2\pi c}{\lambda^2}\beta^{(2)}. \tag{2.47}$$

When the spectral bandwidth of the electric field envelope is relatively narrow it is generally sufficient to limit the Taylor-series expansion to the second order dispersion coefficient. In this case, and neglecting diffraction, the Helmholtz equation can be written in the spectral domain as:

$$\frac{\partial A(\omega-\omega_0,z)}{\partial z} = -i\left[\beta^{(1)}(\omega-\omega_0) + \frac{1}{2}\beta^{(2)}(\omega-\omega_0)^2\right]A(\omega-\omega_0,z). \tag{2.48}$$

Going back to the time domain by applying inverse Fourier transform gives:

$$\left(\frac{\partial}{\partial z} + \frac{1}{v_g}\frac{\partial}{\partial t}\right)A(t,z) = \frac{i\beta^{(2)}}{2}\frac{\partial^2}{\partial t^2}A(t,z). \tag{2.49}$$

Changing the coordinates $T = t - z/v_g$, where T represents the time in a frame of reference moving at the group velocity of the carrier frequency ω_0, one obtains the equation describing the dispersive propagation of light in the time domain.

$$\frac{\partial}{\partial z}A(T,z) = \frac{i\beta^{(2)}}{2}\frac{\partial^2}{\partial T^2}A(T,z). \tag{2.50}$$

The temporal evolution of the electric field envelope depends mainly on by the second-order dispersion, making it a crucial parameter in governing light propagation in a medium.

2.6 Nonlinear effects

The description of electromagnetic wave propagation through a medium using the susceptibility formalism provides a very useful tool that explain most of classical light propagation phenomena. However, the assumption that a medium polarization is linearly proportional to the electric field of a propagating wave as stated in Eq. (2.11) is not always fulfilled. The material response to the propagating electromagnetic wave can also depend on the field strength [18]. In this case, the material polarization can be

described by a Taylor-series expansion of the electric field powers:

$$\boldsymbol{P}_{NL} = \boldsymbol{P}^{(0)} + \boldsymbol{P}^{(1)} + \boldsymbol{P}^{(2)} + \boldsymbol{P}^{(3)} + ... + \boldsymbol{P}^{(q)} + ... \,, \tag{2.51}$$

where:

$$P_k^{(1)} = \epsilon_0 \; \chi_{e,kl}^{(1)} \cdot E_l, \tag{2.52}$$

$$P_k^{(2)} = \epsilon_0 \; \chi_{e,klm}^{(2)} \cdot E_l E_m, \tag{2.53}$$

$$P_k^{(3)} = \epsilon_0 \; \chi_{e,klmn}^{(3)} \cdot E_l E_m E_n, \tag{2.54}$$

$$....$$

$$P_k^{(q)} = \epsilon_0 \; \chi_{e,klmn...}^{(q)} \cdot E_l E_m E_n ..., \tag{2.55}$$

where $k, l, m, n = \{x, y, z\}$ and $\chi_e^{(q)}$ is a q-th order material susceptibility tensor. Due to the presence of higher-order polarization terms a new source term needs to be included in the propagation equation:

$$\nabla \times \nabla \tilde{\boldsymbol{E}} + \frac{1}{c^2} \frac{\partial^2 \tilde{\boldsymbol{E}}}{\partial t^2} = -\mu_0 \frac{\partial^2 \boldsymbol{P}_{NL}}{\partial t^2}. \tag{2.56}$$

The nonlinear polarization P_{NL} enables the interaction of propagating waves, allowing energy transfer between different angular and frequency components of the light spectrum.

Nonlinear effects in optical fibers

The magnitude of nonlinear interactions depends on the medium properties, the strength of the electromagnetic field and the interaction length. The development of optical fibers with low attenuation [19] has enabled to enhance the nonlinear effects by confining light over long distances. The freedom in the design of fiber structures and materials enables tailoring the nonlinear and dispersive properties to enhance the desired effects. The light propagation in optical fibers is dominated by dispersive effects and the third-order nonlinear effects, as the second-order nonlinearity is forbidden in centrosymetric materials. The temporal evolution of the electromagnetic field propagating in a single-mode fiber [20,21] (here along the z direction) is described by the

generalized Nonlinear Schrödigner equation[21]:

$$\frac{\partial A}{\partial z} + \frac{\alpha}{2}A - i\sum_{m\geq 2}\left(\frac{i^m}{m!}\beta^{(m)}\frac{\partial^m}{\partial T^m}A\right) = i\gamma A(z,T)\int_{-\infty}^{\infty} R(T')\times|A(z,T-T')|^2 dT'. \tag{2.57}$$

Here, $A \equiv A(z,T)$ is the complex envelope of the electric field normalized such that $|A(z,T)|^2$ gives the instantaneous power of the light propagating in the fiber, α is the linear loss coefficient, γ is the nonlinear coefficient and $R(T)$ is the nonlinear response function including the instantaneous electric and delayed Raman contributions[22,23]. The generalized Nonlinear Shrödinger Equation can be solved numerically with the use of a split-step Fourier Method[21]. It describes a range of nonlinear effects including self phase modulation, cross-phase modulation, soliton dynamics[24–29], shock formation and others.

Modulation Instability

An important nonlinear phenomenon occurring in fibers is modulation instability[31–34]. In this process a perturbed monochromatic wave propagating through the fiber is unstable for a range of perturbation frequency determined by $g(\omega-\omega_0)$ around the light carrier frequency ω_0:

$$g = \frac{1}{2}\sqrt{-{\beta^{(2)}}^2(\omega-\omega_0)^4 - 4\beta^{(2)}(\omega-\omega_0)^2\gamma P_0}, \tag{2.58}$$

where P_0 is the power of the propagating wave.
Modulation instability can only occur in the anomalous dispersion regime (when $\beta^{(2)} < 0$) and leads to the energy transfer from the pump to any other frequency component[35] present under the gain curve g. Modulation instability can be seeded by injecting a second wave into the fiber or it can occur spontaneously from the noise present in the carrier wave intensity.

Chapter 3

White Light Interferometry

This chapter introduces the basic concepts of white light interferometry along with the different light sources suitable for the technique. We then focus on the description of stroboscopic white light interferometry showing how broadband supercontinuum sources are particularly adapted to high speed and high resolution measurements.

3.1 Coherence of light

Coherence is a fundamental quantity that describes light behaviour in interferometric experiments[36]. It can be quantified by the first order degree of coherence function $g^{(1)}$ defined as

$$g^{(1)}(\boldsymbol{r}_1, t_1, \boldsymbol{r}_2, t_2) = \frac{\langle \boldsymbol{E}^*(\boldsymbol{r}_1, t_1) \cdot \boldsymbol{E}(\boldsymbol{r}_2, t_2) \rangle}{\left[\left\langle |\boldsymbol{E}(\boldsymbol{r}_1, t_1)|^2 \right\rangle \left\langle |\boldsymbol{E}(\boldsymbol{r}_2, t_2)|^2 \right\rangle \right]^{1/2}}, \tag{3.1}$$

where $\langle ... \rangle$ denotes a statistical ensemble average. When calculated at a single spatial location $\boldsymbol{r}_1 = \boldsymbol{r}_2$ for a statistically stationary field, one can simplify the coherence function by introducing the time difference $\tau = t_1 - t_2$:

$$g^{(1)}(\tau) = \frac{\langle \boldsymbol{E}^*(t) \cdot \boldsymbol{E}(t+\tau) \rangle}{\left\langle |\boldsymbol{E}(t)|^2 \right\rangle}, \tag{3.2}$$

where $\langle ... \rangle$ denotes the average over time t.

The first degree of coherence is a normalized, complex function whose modulus is limited by 1 and depends on how the phase of the electric field is preserved when the electric field is delayed in time. If, for a given time delay τ, the relative phases of the electric field and its time-delayed replica remains constant at every time point t, the magnitude to the complex degree of coherence is equal to 1. On the other hand, if the phases are uncorrelated with increasing time shift, the degree of coherence drops to 0. It is worth pointing out that the degree of coherence is always equal to 1 for zero-delay. It is useful to consider the modulus of the degree of coherence to determine the behaviour of a light source in the interferometric system. One can then determine the coherence time parameter τ_{coh} which characterizes the time interval over which the phase of the electric field is stable and thus how long the light field remains coherent:

$$\tau_{coh} = \int_{-\infty}^{+\infty} \left| g^{(1)}(\tau) \right|^2 d\tau. \tag{3.3}$$

The degree of coherence is directly linked to the light source spectrum such that, in general, the spectral bandwidth and the coherence time can be related as:

$$\tau_{coh} \sim \frac{1}{\Delta\nu}. \tag{3.4}$$

The proportionality factor depends on the exact spectrum shape. All light sources have a limited coherence time. It can vary from seconds for monochromatic lasers, to microseconds for typical semiconductor lasers, picoseconds for diodes, and femtoseconds for broadband LEDs, white light sources and incandescent bulbs [37,38]. The notion of coherence of a light source is relative to the specific experiment it is used in. For example, if the source coherence time exceeds the measurement time, the source may be treated as fully coherent although it is not if one considers longer measurement times.

3.2 Interferometry

Interference is a phenomenon where (at least) two light waves are superimposed. Depending on the phase relation between the electric field associated with each wave at a given location and time, the amplitude of the resulting field can increase (constructive

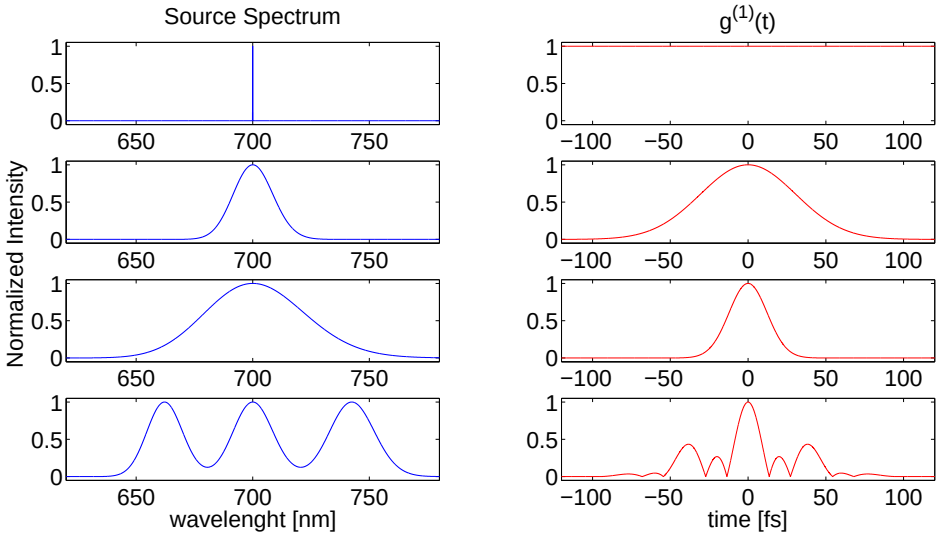

Figure 3.1: (a) normalized source spectrum and (b) first order coherence function of given source, calculated for a monochromatic source, 20 nm FWHM bandwidth LED, 50 nm FWHM bandwidth LED and source composed of three 20 nm bandwidth diodes centered at 660 nm 700 nm and 740 nm wavelength.

interference) or decrease (destructive interference), when compared to the intensity of the interfering waves. Of course, electromagnetic waves interfere all the time but since, in linear propagation, they do not exchange energy with each other, the interference effect is only observed when the intensity of light is recorded or scattered from an object. The basic interferometric measurement set-up is the Michelson interferometer presented in Fig. 3.2(a). The light beam from the source is divided between the two arms of the interferometer. In one arm, the beam is reflected from a reference mirror, while in the other it is reflected from a sample. After reflection, both beams are enter the beam splitter again and are divided for the second time. The part of the sample beam that was transmitted straight through the beam splitter interferes with the part of the reference beam that was reflected from the beam splitter, the same happens with other parts of beams. The other common interferometer set-up is the Mirau interferometer presented in Fig. 3.2(b). In this configuration the beam splitter is placed behind the focusing lens of the objective. The reference mirror is fixed at the center of the optical axis. The light reflected from the mirror and the sample is collected by the lens also used for focusing. This design is particularly useful for microscopy

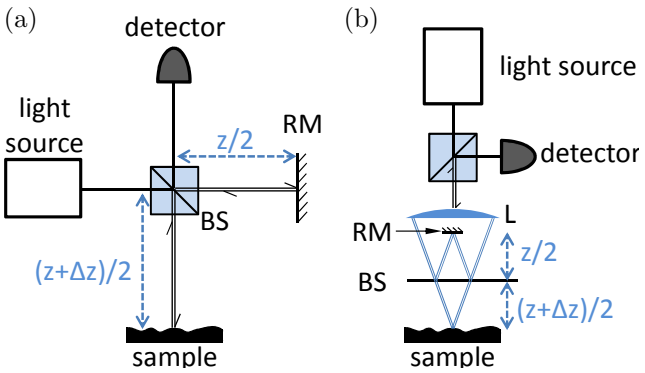

Figure 3.2: Most common interferometric setups: (a) Michelson interferometer, (b) Mirau interferometer

applications.

Due to the interference, the energy of the light source can be directed to one or both directions, depending on the relative phase between the input beams. In a Michelson interferometer this means that the energy can be directed to the detector of the interferometer or back to the light source. The phase acquired by the light beam depends on the wavelength of the light, the distance it has travelled and the refractive index of the medium. For simplicity, we omit the vectorial nature of the field and assume that the polarization of light is linear and constant. For a sample consisting of a single reflective interface the fields can be easily described by the following equations:

$$E_r(t) = \frac{1}{2} E_0 \left(t + \frac{z}{c} \right), \tag{3.5}$$

$$E_s(t) = \frac{r}{2} E_0 \left(t + \frac{z + \Delta z}{c} \right), \tag{3.6}$$

where E_s and E_r are the electric fields arriving at the beam-splitter from the sample and the reference mirror. Here, E_0 represents the field of the light source, z describes optical path length in the reference arm, Δz is the difference between the optical paths lengths in the reference and sample arms, and r is the reflection coefficient of the sample. For simplicity the vectorial form of the field was omitted with assumption of constant linear polarization of light. Elements in the optical path common for both beams do not affect the relative phase difference and thus do not need to be taken into consideration. The output field of the interferometer E_{out} is the sum of the interfering

fields:

$$E_{out}(t) = \frac{1}{2}\left[E_r(t) + E_s(t)\right]. \tag{3.7}$$

The detector records the light intensity as a function of the position of the reference mirror, or equivalently as a function of the optical path difference Δz:

$$\begin{aligned} I(\Delta z) &= \epsilon_0 cn \int |E_{out}(t)|^2 dt \\ &= \frac{\epsilon_0 cn}{4} \int |E_r|^2 + |E_s|^2 + (E_r E_s^* + c.c.) dt \\ &= \frac{\epsilon_0 cn}{4} \int |E_0(t)|^2 (1 + r^2) dt + 2\Re\left[\frac{\epsilon_0 cnr}{4} \int E_0(t') E_0^*(t' + \tau) dt'\right], \end{aligned} \tag{3.8}$$

where $\tau = \Delta z/c$, $t' = t + z/c$ and $\Re$ stands for the real part.

Introducing the average source intensity as $I_0 = \epsilon_0 cn \left\langle |E_0|^2 \right\rangle$, one can rewrite Eq. (3.8) as:

$$I(\Delta z) = \frac{1 + r^2}{4} I_0 + \frac{r}{2} I_0 \Re\left[g^{(1)}\left(\frac{\Delta z}{c}\right)\right]. \tag{3.9}$$

The interference signal consists of a constant term (independent of Δz) and a Δz-varying term proportional to the real part of the first order degree of coherence of the light source used in the experiment. The largest intensity is recorded when the coherence function reaches its maximum, i.e. when Δz is equal to zero. The interferogram recorded as a function of Δz provides information about the depth of the sample. A single line scan perpendicular to the sample is called A-scan. A scan that provides a cross-section image of the sample, for example by performing a series of A-scans along a line parallel to the sample surface, is called B-scan. It is also possible to perform a C-scan, in which data are collected from a whole at given Δz position with a CCD camera instead of a single detector. A schematic illustration of each scan area is presented in Fig. 3.3.

With WLI it is relatively straightforward to make a C-scan by using a 2D camera. Each pixel of the camera generates an A-scan line when the reference mirror is moved. Only a single scan is then required to obtain a full 3D image of the sample.

For high precision measurement it is important to use a light source with a short coherence time as it allows to identify the modulation peak more accurately and enables to distinguish multiple closely spaced interfaces within the sample. Examples of simulated interferograms measured with different light sources are shown in Fig. 3.4.

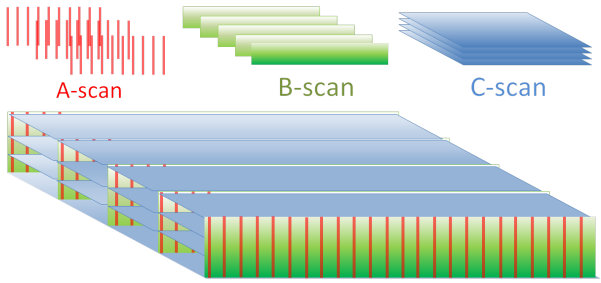

Figure 3.3: Modes of data acquisition in interferometric measurements

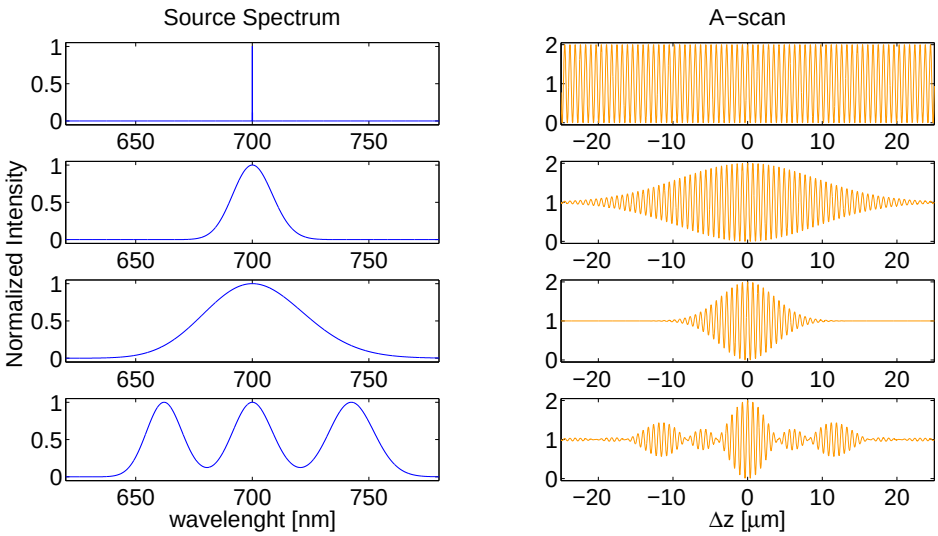

Figure 3.4: Comparison of A-scans of a single interface sample obtained for different light source spectra. (a) Source spectrum and (b) corresponding A-scan.

3.3 Stroboscopic White Light Interferometry

Stroboscopic White Light Interferometry [39–41] allows to image samples that are in periodic movement . This technique is generally implemented by modifying a standard WLI, such that the sample is periodically illuminated. The light source in this case produces pulses synchronized with the sample movement such that it is always the same phase of movement that is probed. Therefore, although the sample may be moving rapidly, the detector records interference only at a single position of the sample

enabling to generate a sharp image and making it appear as if the sample movement was frozen in time. The principle of this process is illustrated in Fig. 3.5. SWLI can be used to measure the influence of rapid changes in sample shape caused, for example, by periodic temperature variations, electric field or mechanical strain modulation applied to the sample. The requirements placed on the light source are similar as for

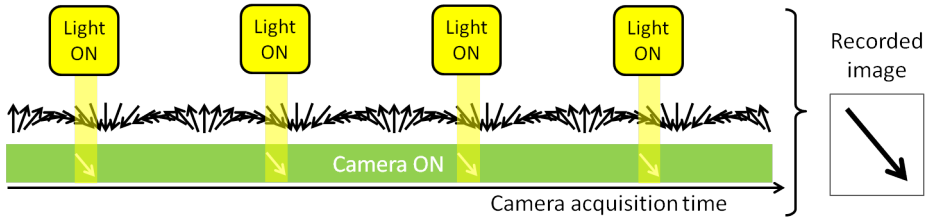

Figure 3.5: Principle of stroboscopic measurement. The pulsed light is synchronized with the period of the object movement (arrow rotation), illuminating only a given, single movement phase. This allows to record a sharp image of the moving object even though the camera acquisition time is much longer than the movement period.

conventional WLI. It should be of low coherence but it should also emit light pulses on demand. This can be achieved by modulating continuous light sources with temporal gate filters or by using light sources that already create pulses. Both approaches have their drawbacks and related technical difficulties. Applying temporal filters to obtain a short illumination time (in relation to the pulse period) results in a small duty cycle of the filter, which can significantly decrease the power output of the source. Furthermore, for high oscillation frequencies, it is hard to find a filter with proper speed and high extinction ratio while operating over a broad spectrum range. Short pulse light sources on the other hand, lack the optical bandwidth, like the laser diodes, or the possibility of tuning the pulse repetition rate, as is the case of mode-locked lasers.

3.4 Supercontinuum light source for Stroboscopic White-light Interferometry

We have developed a supercontinuum light source for SWLI[42–44] presented in publication P1 which allows to overcome the problems associated with modulated continuous diodes or mode-locked lasers. Extensive numerical simulations, using the split-step Fourier method, shows that it is possible to obtain a significant spectrum broad-

ening by injecting 1-ns long pulses with several kW peak power into a single-mode dispersion-shifted fiber[45–51]. In that case, noise-seeded modulation instability[52–54] leads to the generation of a train of randomly distributed solitons that experience the Raman frequencu-shift[55–57] and emit dispersive waves. The operating source was built from a gain-switched, fiber-coupled laser, generating 0.5ns long pulses[58] at 1550-nm wavelength with up to 4-kW peak power and tunable repetition rate. These pulses were injected into a 6-m long dispersion-shifted fiber. Because of the relatively short distance of propagation in the fiber compared to the long pulse duration, its duration does not exceed 1-ns at the fiber output, allowing to maintain the duty cycle. Yet,

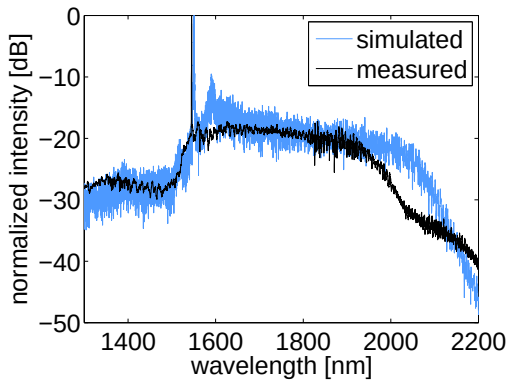

Figure 3.6: Comparison between simulated and measured spectra of our developed supercontinuum source.

the source is not ideal, due to the presence of a high pump residue that influences its temporal coherence properties. The pump peak has a narrow bandwidth and thus its coherence time is long, decreasing the source performance in WLI experiments. Furthermore, nearly all the frequency component lies in the near-infra-red, outside the detection band of the most common silicon type detectors. Both of these problems can be solved by use of wave mixing in a nonlinear crystal[59,60]. In this process, presented in Fig. 3.7(a), the light is focused into a nonlinear crystal where due to the strong second order nonlinearity its frequency is doubled. Due to the simultaneous presence of many spectral components it is more correct to talk about sum frequency generation that allows interaction of multiple frequency pairs. The benefit of sum frequency generation is two-fold, part of the spectrum is converted to the operating range of silicon-based cameras and the pump residue is filtered out. The spectra of the light measured before and after the nonlinear crystal are presented in Fig. 3.7(b) and 3.7(c). Indeed, spectral components corresponding to the pump residue is spread over

entire duration of the initial pump pulse with a much lower peak power than other SC spectral components and thus does not produce efficient second harmonic light.

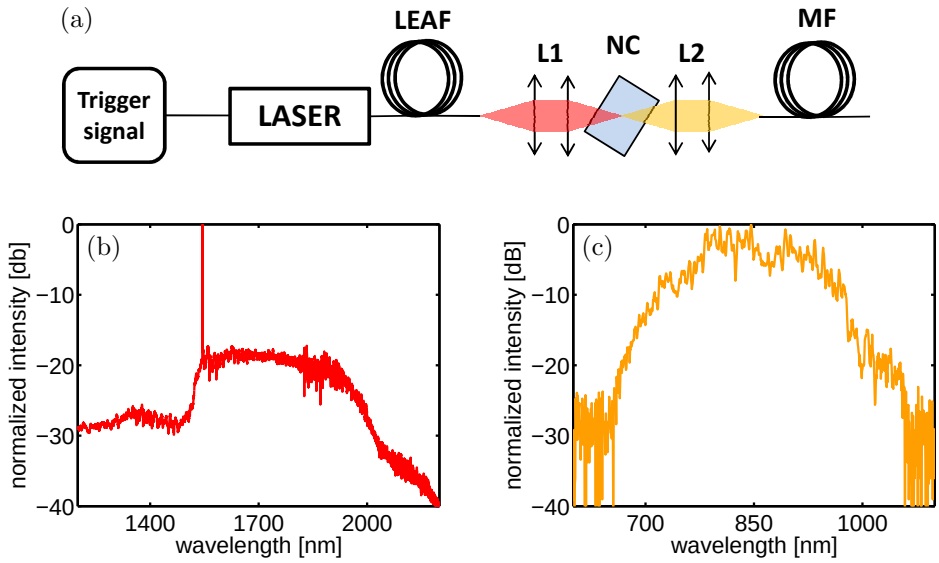

Figure 3.7: (a) Experimental set-up for frequency doubled SC source, LEAF - dispersion shifted fiber, NC - nonlinear crystal, L1, L2 free-space focusing and collimating lens system, MF - multimode fiber, (b) SC spectrum measured after the LEAF fiber, (c) SC spectrum measured after the multi-mode fiber (MF).

The BBO nonlinear crystal used in the experiments is rotated to appropriate angle to enable efficient frequency conversion. In the 1.6-μm spectral region, the dependence of the phase-matching angle on wavelength is nearly flat, which enables efficient interaction for the majority of the SC spectral components. Furthermore, focusing the light into the crystal creates a cone that covers most of the angular acceptance band. Yet, the phase-matching is not met perfectly for all the angles and wavelengths, which causes the light at the crystal output to be spectrally chirped, with different sum frequency components propagating at separate angles. To avoid physical separation of the spectral components, the light was then coupled to a 200-μm core size multi-mode fiber, which collects all the spectral components and mixes them over multiple modes. The large size of the modes at the output of the fiber allows to irradiate a larger area of the sample than it would be possible with a single-mode fiber output.

To extend the measurement possibilities to objects oscillating with frequencies up to few-MHz, a sub-harmonic triggering method was introduced. In this method, a

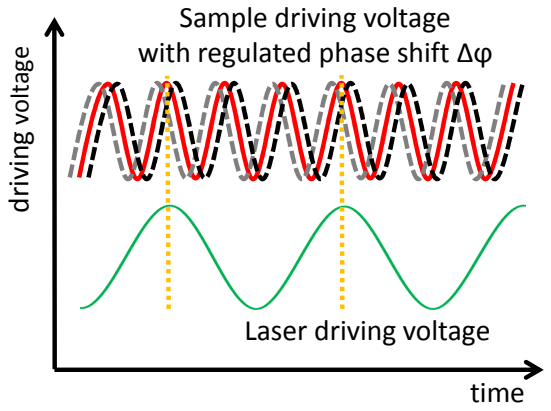

Figure 3.8: Relation between sample and SC driving voltages. In the presented case, the laser is driven with the 4-th sub-harmonic of the sample movement.

light pulse is triggered only every n-th sample oscillation as conceptually shown in Fig. 3.8. This approach is necessary for developed SC source as with increasing repetition rate the pump laser peak power diminishes and becomes insufficient for supercontinuum generation. Still the duty cycle of the source is low enough to provide sufficient illumination time and generate a sharp image of the object.

To evaluate the performance of the light source and proposed modification of the SWLI technique, a measurement of capacitive micro-machined ultrasonic transducer array (CMUT) was performed. The experimental set-up shown in Fig. 3.9 utilises on Airy-type interferometer objective. During the measurement the resonant frequency of the CMUT component was found to be 2.16 MHz, at which the sample oscillation exhibit the largest amplitude. The supercontinuum source was triggered with the 32-nd subharmonic frequency, so that it could operate in the most efficient repetition rate range. Depth scanning was achieved by sample translation using a piezoelectric translation stage. During the scan, for each position a picture of selected sample area was taken by a CCD camera. In data post-processing[61–65], each pixel allows to produce an A-scan line from a series of recorded pictures and to evaluate the position of the sample surface. The reconstructed 3D image of the CMUT is presented in Fig. 3.10. The use of the newly developed SC light source allowed to obtain sub-100 nm resolution and the sub-harmonic pulse triggering enables to perform measurement of

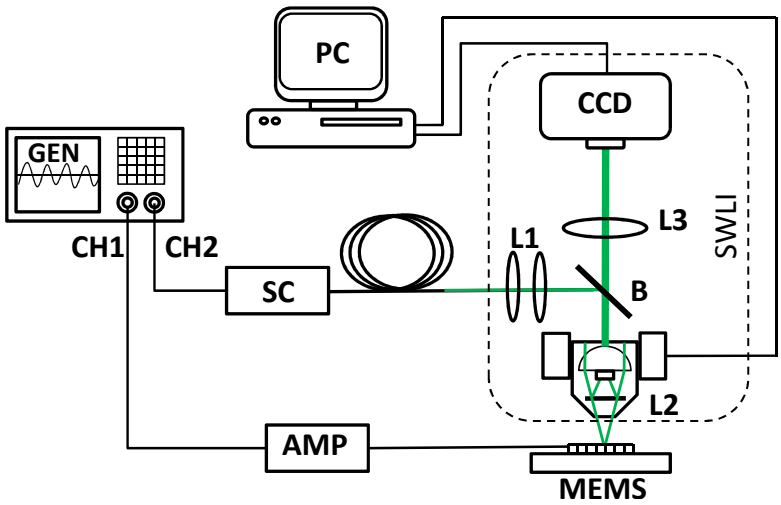

Figure 3.9: Experimental set-up for SWLI, GEN- function generator driving the supercontinuum light source (SC) and the amplifier (AMP) driving the sample (MEMS). The light from the source is collimated by a set of lenses L1 and directed through the beam-splitter (B) to the objective (L2) with built in Airy interferometer. The light form the interferometer is recorded by a CCD camera with objective lens (L3). Data from the camera are recorded by a PC which also controls the position of the interferometer.

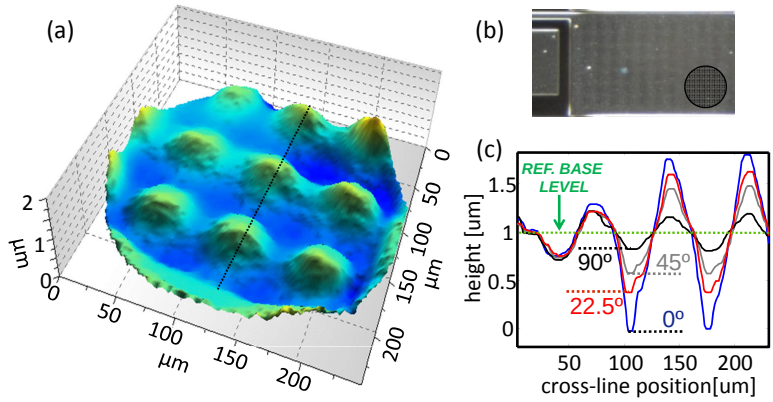

Figure 3.10: SWLI results of CMUT sample. (a) 3D reconstruction, (b) picture of the sample with part under examination highlighted, (c) cross-section of the sample image created for different sample oscillation phases.

samples oscillating in the frequency range from kHz up to several MHz.

Chapter 4

Intensity Optical Coherence Tomography

In this chapter a brief description to Optical Coherence Tomography is given, followed by an introduction of Intensity Optical Coherence Tomography (IOCT), a newly proposed imaging technique with build-in dispersion cancellation and resolution improvement.

4.1 Optical Coherence Tomography in the spectral domain

Optical Coherence Tomography (OCT)[66–68] is a sister technique of White Light Interferometry. It is commonly used to obtain images of biological samples with high in-depth resolution. Due to its non-invasive character and absence of ionizing radiation or toxic contrast agents, the technique has found multiple medical applications[69,70] and been successfully commercialized. It is now widely used in eye retina, skin and blood vessel examination. It is also a method of choice in biological scientific research. Multiple modifications of the technique have been developed, including polarization sensitive detection or Doppler effect based velocity measurement[71–74], enabling to

collect more information about the tissue condition and biological activity. OCT measurements can be performed in two different configurations[75]: in the time-domain, when scanning is made while changing the reference mirror position as in WLI, or in the spectral domain, which we discuss in detail in this paragraph. Spectral-domain optical coherence tomography (SOCT)[76] requires a broadband light source that can be stationary, pulsed or of swept-type (i.e with a time-varying wavelength). Measurement of the phase relation between different wavelength components enables to determine the distance to the sample. The bandwidth of the light source (related to its coherence time) defines, to a great extend, the performance of the whole system. The experimental set-up is similar to that of WLI. The advantage of SOCT over its temporal counterpart is the absence of the need for a reference mirror translation. The information collected from the reference mirror scan is instead obtained by a spectral measurement, which can be done at once with a line camera spectrometer, making a single A-scan and B-scan much faster. However it is worth noticing, that in order to perform a 3D-scan, at least one scan translation is necessary, as it is the case for a 3D temporal OCT scan.

We next present a quantitative description of SOCT in a Michelson interferometer configuration. Because SOCT is performed in the spectral domain, it is most convenient to use the spectral representation of the light amplitude $\boldsymbol{A}(\omega)$ as defined in section 2.4. For simplicity, we omit the vectorial nature of the field and assume that the polarization of light is linear and constant. The initial amplitude $A_0(\omega)$ varies as a function of propagation distance z:

$$A(\omega, z) = A_0(\omega) \cdot e^{ik(\omega)z}. \tag{4.1}$$

For the most simple case of a single reflective interface placed in the sample arm at distance z_S, the spectral amplitude of the electric field reflected from the sample A_S and reference arm A_R can be written as:

$$A_S(\omega) = \frac{r}{2} A_0(\omega) \cdot e^{ik_S(\omega)\ z_S}, \tag{4.2}$$

$$A_R(\omega) = \frac{1}{2} A_0(\omega) \cdot e^{ik_R(\omega)\ z_R}, \tag{4.3}$$

where r is the amplitude reflection coefficient (note that in principle r may depend on ω) and z_R is the distance to the reference arm mirror.

The light spectrum measured at the output of the interferometer is then given by

$$S(\omega) = 2\epsilon_0 cn \left|A_S(\omega) + A_R(\omega)\right|^2, \tag{4.4}$$

or in a more convenient form:

$$S(\omega) = \frac{1}{4} S_0(\omega) \left[1 + |r|^2 + 2|r|\cos(k_S z_S - k_R z_R + \phi_r)\right]. \tag{4.5}$$

$S_0(\omega) = 2\epsilon_0 cn|A_0(\omega)|^2$ is the light source spectrum and ϕ_r is the induced phase change by the sample. From the above equation, one first notices that the measured spectrum $S(\omega)$ does not depend on the complex spectral amplitude of the source, but rather on its spectral intensity. This means that the initial phase relation between the different spectral components is irrelevant such that any light source with an identical spectrum will produce an identical interferometric image. The term in brackets on the other hand consists of two constant terms and a modulation component which carries the information about the measured sample.

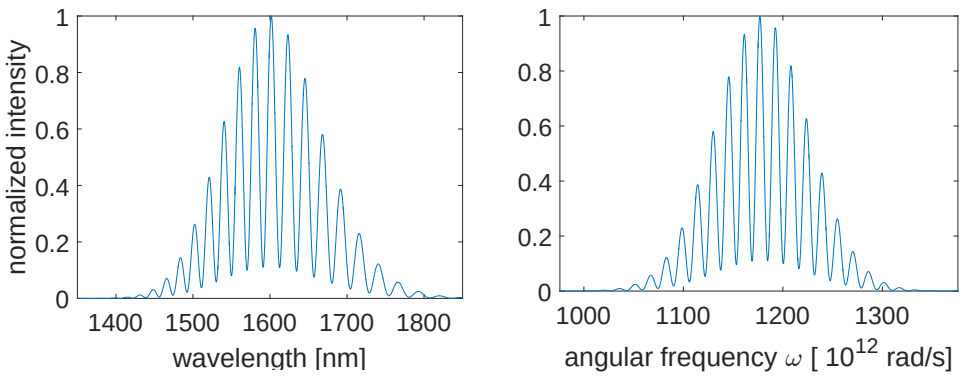

(a) (b)

Figure 4.1: OCT spectral interferogram generated by light reflected from a single interface sample vs. wavelength (a) and angular frequency (b). The period of the modulation in the frequency domain is constant if there is no dispersion in the system.

An example of a recorded interferogram is shown in Fig. 4.1. The envelope of the interferogram simply represents the source spectrum while the period of the modulation underneath depends on the position of the interface in the sample arm. The position of the interface can thus be directly obtained by taking the Fourier transform of the

spectral interferogram:

$$\mathcal{F}\Big(S(\omega)\Big) = \frac{1}{4}\mathcal{F}\Big(S_0(\omega)\Big) \otimes \Big[\left(1+|r|^2\right)\delta(0) + \mathcal{F}\Big(2|r|\cos\left(k_S z_S - k_R z_R + \phi_r\right)\Big)\Big]. \quad (4.6)$$

Assuming that there is no dispersion such that $n_R(\omega) = n_S(\omega) = n$, Eq. (4.6) can be simplified to

$$\mathcal{F}\Big(S(\omega)\Big) = \frac{1}{4}\mathcal{F}\Big(S_0(\omega)\Big) \otimes \Big[\left(1+|r|^2\right)\delta(0) + r\delta(z-\Delta z) + r^*\delta(z+\Delta z)\Big]. \quad (4.7)$$

where δ is the Kronecker delta function. The Fourier spectrum of the interferogram consists of three distinct peaks with different amplitudes and positions. The shape and width of the peaks however is identical and determined by the source spectrum. The central peak at $z = 0$ represents the Fourier transform of the source spectrum whilst the two other peaks are located symmetrically around the central peak at the distance $\Delta z = \pm[n_S(\omega_0)z_S - n_R(\omega_0)z_R]$ where $n_R(\omega_0)$ and $n_s(\omega_0)$ are the refractive indices of the medium in the reference and sample arm, respectively, at the central frequency of the light source ω_0. It is the two peaks located symmetrically around the central peak that contain the information about the sample. Specifically, their height is directly proportional to the sample amplitude reflection coefficient whilst the location corresponds to the position of the sample interface in relation to the reference mirror. It is important to bear in mind that (i) the retrieved distance is then twice as long as the actual physical distance and (ii) the retrieved distance is the optical distance, which can exceed the physical distance if the refractive indices $n > 1$ (i.e. when propagation does not occur in air). This is generally accounting for by rescaling the z-axis into an actual physical distance.

From the above, it then appears that a drawback of SOCT is its inability to distinguish between the positive $+\Delta z$ and negative $-\Delta z$ position of the sample. In the case of multiple interfaces, this requires the sample to be placed on one side of the zero-path difference such that one can then discriminate the positive from negative z half-axes of the image.

OCT in dispersive media

In the non-dispersive case, the width of the peaks in the Fourier spectrum of the interferogram is determined only by the bandwidth of the light spectrum (more specifically

its Fourier transform). In the presence of dispersion, the width of the peaks increases, which can reduce significantly the resolution. We next provide a quantitative description of SOCT in dispersive media, assuming that the source spectral envelope has a Gaussian shape, defined by:

$$S_0(\omega) = Se^{-\frac{(\omega-\omega_0)^2}{2a^2}}, \tag{4.8}$$

where S is the maximum spectral intensity, ω_0 the central frequency, and a is the spectral bandwidth related to the ω_{FWHM} (full width at half the maximum) by:

$$a = \frac{\omega_{\text{FWHM}}}{2\sqrt{2\ln 2}}. \tag{4.9}$$

The effect of dispersion can be best seen by expanding the propagation constants k_R and k_S into a Taylor-series around the central frequency ω_0 (see also section 2.5). Limiting the expansion to the three first terms, one obtains:

$$k_S \approx \beta_S^{(0)} + \beta_S^{(1)}\Delta\omega + \frac{1}{2}\beta_S^{(2)}\Delta\omega^2, \tag{4.10}$$

$$k_R \approx \beta_R^{(0)} + \beta_R^{(1)}\Delta\omega + \frac{1}{2}\beta_R^{(2)}\Delta\omega^2, \tag{4.11}$$

where $\Delta\omega = \omega - \omega_0$. The optical path difference between the sample and reference arm is then given by:

$$\begin{aligned}(k_S z_S - k_R z_R) = \\ &= \left(\beta_S^{(0)} + \beta_S^{(1)}\Delta\omega + \frac{1}{2}\beta_S^{(2)}\Delta\omega^2\right) z_S - \left(\beta_R^{(0)} + \beta_R^{(1)}\Delta\omega + \frac{1}{2}\beta_R^{(2)}\Delta\omega^2\right) z_R \\ &= \left(\beta_S^{(0)} z_S - \beta_R^{(0)} z_R\right) + \left(\beta_S^{(1)} z_S - \beta_R^{(1)} z_R\right)\Delta\omega + \left(\frac{1}{2}\beta_S^{(2)} z_S - \frac{1}{2}\beta_R^{(2)} z_R\right)\Delta\omega^2 \\ &= b_0 + b_1\Delta\omega + b_2\Delta\omega^2. \end{aligned} \tag{4.12}$$

The b_0, b_1 and b_2 parameters are constants related to the zero, first and second-order dispersion coefficients. With this expansion, Eq. (4.5) can be rewritten as:

$$\begin{aligned} S(\omega) &= \frac{1}{4}Se^{-\frac{(\omega-\omega_0)^2}{2a^2}}\left[1 + |r|^2 + re^{i(b_0+b_1\Delta\omega+b_2\Delta\omega^2)} + r^* e^{-i(b_0+b_1\Delta\omega+d_2\Delta\omega^2)}\right] = \\ &= \frac{1}{4}Se^{-\frac{(\omega-\omega_0)^2}{2a^2}}\left[1 + |r|^2 + 2|r|\cos\left(b_0 + b_1\Delta\omega + b_2\Delta\omega^2 + \phi_r\right)\right] = \\ &= \frac{1}{4}Se^{-\frac{(\omega-\omega_0)^2}{2a^2}}\left[1 + |r|^2 + 2|r|\cos\left((b_1 + b_2\Delta\omega)\Delta\omega + b_0 + \phi_r\right)\right]. \end{aligned} \tag{4.13}$$

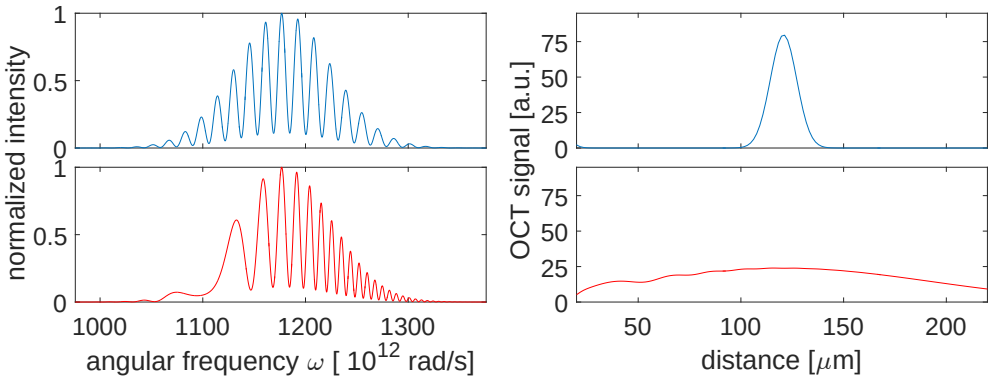

Figure 4.2: (a) Comparison of OCT interferograms recorded without (top) and with (bottom) dispersion present in the system (bottom). (b) Interface position reconstructed from the interferograms shown in (a). The assumed amount of dispersion is intentionally large to better visualize its effect.

It can now be seen that the presence of second-order dispersion (related to the b_2 parameter) changes the spectral modulation period which increases linearly with frequency ω. The effect of dispersion on the width of the peak in the Fourier spectrum of the interferogram that corresponds to the sample position can be examined more precisely by taking the Fourier transform of the r-dependent term in Eq. (4.13):

$$\begin{aligned}
&\mathcal{F}\left(\frac{1}{4}Se^{-\frac{(\omega-\omega_0)^2}{2\Delta a^2}}\cdot re^{i(b_0+b_1\Delta\omega+b_2\Delta\omega^2)}\right) = \\
&\qquad = \frac{1}{2\pi}\int\frac{1}{4}Se^{-\frac{(\omega-\omega_0)^2}{2\Delta a^2}}\cdot re^{i(b_0+b_1\Delta\omega+b_2\Delta\omega^2)}\cdot e^{-i\Delta\omega t}d\Delta\omega \\
&\qquad = \frac{Sre^{ib_0}}{8\pi}\cdot\int e^{-\left(\frac{1}{2a^2}-ib_2\right)\Delta\omega^2}\cdot e^{ib_1\Delta\omega}\cdot e^{-i\Delta\omega t}d\Delta\omega \\
&\qquad = \frac{Sre^{ib_0}}{4\sqrt{2\pi}}\cdot\sqrt{\frac{1+i2a^2b_2}{\left(\frac{1}{a^2}+(2ab_2)^2\right)}}\cdot e^{-\frac{(1+i2a^2b_2)}{2\left(\frac{1}{a^2}+(2ab_2)^2\right)}(t-b_1)^2}.
\end{aligned} \tag{4.14}$$

In the case of a light source with a Gaussian spectral envelope, the peak in the Fourier spectrum of the interferogram that corresponds to the sample position has also a Gaussian shape. One can see that b_0 only affects the phase and has no effect on the amplitude or width of the peak. The parameter b_1, related to the group-delay, changes the peak position and therefore the actual measured distance. The group-velocity dispersion, related to b_2, increases the width, alters the phase, and decreases

the amplitude of the Gaussian peak profile. The difference in first-order dispersion between the arms of the interferometer determines the sample position. The second-order dispersion increases the width of the peak and decreases its amplitude. This can be understood from the fact that the source spectral envelope becomes chirped when propagating through the dispersive medium. Dispersion-induced broadening of the peak that contains the sample information is detrimental as it decreases the resolution of the OCT system. In the presence of dispersion, the width of the image peak τ_{β_2} is given by:

$$\tau_{\beta_2} = \sqrt{\tau_0^2 + \left(\frac{\Delta(\beta_2 z)}{\tau_0}\right)^2} = \sqrt{\frac{1}{a^2} + (a\Delta(\beta_2 L))^2}, \tag{4.15}$$

where τ_0 is the width of the image peak in the absence dispersion, and $\Delta(\beta_2 L) = b_2$ is the total accumulated dispersion in the system. Time can be converted to distance units, multiplying the time axis by the speed of light $c\tau_0/2$, where the factor of $1/2$ is added to compensate for the distance doubling due to reflection in the interferometer. Introducing the FWHM of the source envelope λ_{FWHM} into Eq. (4.15), the width of the image peak is given by the expression:

$$z_{\text{FWHM}} = \sqrt{\left(\frac{2\ln 2}{\pi}\frac{\lambda_0^2}{\lambda_{\text{FWHM}}}\right)^2 + \left(\frac{\pi c^2 \lambda_{\text{FWHM}}}{\lambda_0^2}\Delta(\beta_2 L)\right)^2}. \tag{4.16}$$

The first term under the square root gives the width of the image peak in the absence of dispersion, as determined by the source spectral width λ_{FWHM} and central wavelength λ_0:

$$z_{\text{FWHM}} = \frac{2\ln 2}{\pi}\frac{\lambda_0^2}{\lambda_{\text{FWHM}}} \approx 0.44\frac{\lambda_0^2}{\lambda_{\text{FWHM}}}. \tag{4.17}$$

This is the minimum with of the image peak that can be achieved. It is then clear that the larger the spectral bandwidth of the source and/or the shorter the central wavelength, the better the resolution. The second term in Eq. (4.16) reflects the broadening resulting from the presence of dispersion in the system and reduces the resolution in comparison to the non-dispersive case. There exists and optimum source bandwidth ω_{min} that minimizes the increase in the image peak width:

$$\omega_{min} = \sqrt{\frac{8\ln(2)}{\Delta(\beta_2 L)}}, \tag{4.18}$$

corresponding to the minimum width that can be achieved for a given amount of dispersion

$$z_{\mathrm{FWHM}}(\omega_{min}) = 2c\sqrt{\Delta(\beta_2 L)\ln 2}. \tag{4.19}$$

The effect of dispersion on the performance of a SOCT system is illustrated in Fig. 4.3 as a function of the source spectral bandwidth. We assume a 700 nm light source and dispersion equivalent to 1 cm of glass. Whilst in general increasing the source bandwidth results in a reduced image peak width, it is clearly not the case when dispersion is present in the system where the minimum achievable image peak width is 13 μm for a 20 nm spectral bandwidth. Dispersion is thus a major obstacle in high

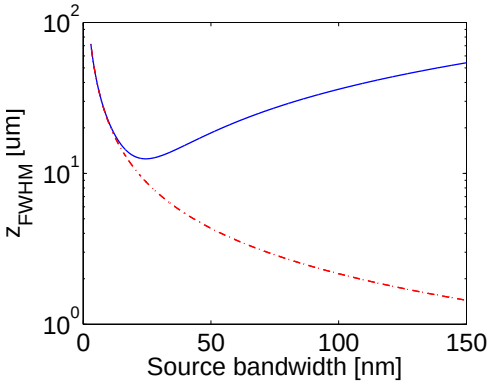

Figure 4.3: OCT image peak width as a function of bandwidth calculated for 700nm center wavelength in case of no dispersion (red) and dispersion introduced by 1 cm thick glass layer (blue)

resolution imaging, both because of an increase in the point spread function and a decrease in the amplitude of the image peak. Several techniques have been developed to overcome the effect of dispersion, including physical dispersion compensation directly in the interferometer arms or by numerical post-processing[77].

4.2 Principles of Intensity Optical Coherence Tomography

Intensity Optical Coherence Tomography (IOCT) is a recently proposed interferometric imaging technique[78,79] that allows to reduce the width of the point spread

function compared to conventional SOCT and is inherently insensitive to dispersion (more specifically to all even orders dispersion coefficients). IOCT was initially inspired by Quantum Optical Coherence Tomography (Q-OCT)[80] where correlations between the arrival time of entangled photons[81–83] are used to determine the distance to the sample. Although Q-OCT is inherently insensitive to dispersion[84–86], it requires the use of sophisticated light sources generating entangled photon pairs and single-photon detectors. This makes the measurement system costly and difficult to implement for practical applications. A classical analogue of Q-OCT in the form of chirped-pulse interferometry has also been proposed[87–90]. Yet, chirped-pulse interferometry also requires complex light sources producing short pulses of light with particular chirp distributions and large enough intensity to enable efficient non-linear interactions. IOCT on the other hand can utilize standard, stationary or pulsed light sources and normal spectrometers just as those used in conventional SOCT. This makes IOCT an interesting potential alternative to SOCT.

The measurement set-up for IOCT inspired from the Hong-Ou-Mandel interferometer is shown in Fig. 4.4. Light from the source is divided into a reference path, where it is reflected from a non-moving mirror, and a sample path where it is reflected from the sample under test. The two beams are then recombined at beam splitter whose outputs are spectrally measured independently. The key aspect in IOCT compared to

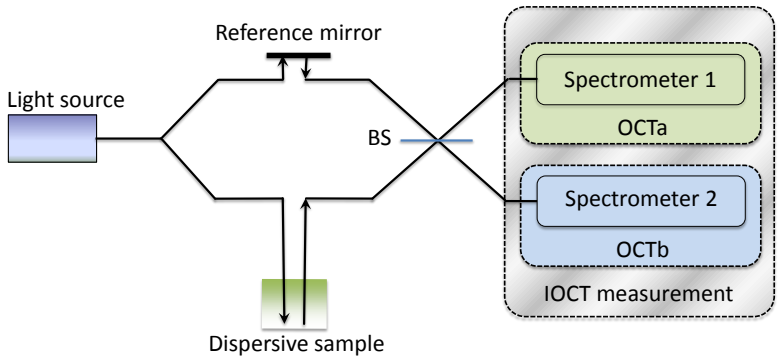

Figure 4.4: Concept sketch of a typical IOCT experiment.

SOCT is the use of spectral correlations between components measured at the output of the interferometer to retrieve the distance to the sample:

$$C(\omega_0', \omega') = S_a(\omega' + \omega_0') \cdot S_b(-\omega' + \omega_0'), \tag{4.20}$$

where S_a and S_b are the spectra measured at the beam splitter outputs, related to the light field spectral amplitude in the reference and sample arm as:

$$S_a(\omega) = 2\epsilon_0 cn \left| A_S(\omega) + iA_R(\omega) \right|^2, \tag{4.21}$$

$$S_b(\omega) = 2\epsilon_0 cn \left| iA_S(\omega) + A_R(\omega) \right|^2. \tag{4.22}$$

Here, $\omega' = \omega - \omega_0$ is the frequency shift with respect to the central frequency ω_0' of the light source spectrum. The output beam splitter induces a $\pi/2$ phase-shift between the sample and reference beam amplitudes such that the two output spectra are symmetric with respect to the frequency axis around ω_0'. Note that, in principle, ω_0' may not be necessarily the central frequency of the light source spectrum and it can be chosen arbitrarily, which in some cases can be beneficial. We next treat the case of a sample consisting of two reflective interfaces p and q, and describe how the correlation function $C(\omega_0', \omega')$ provides information about the sample. The spectral amplitude $A_S(\omega)$ of the field at the sample arm output can be described as:

$$A_S(\omega) = \frac{1}{2} A_0 \left(r_p e^{ik_p(\omega) z_p} + r_q e^{ik_q(\omega) z_q} \right), \tag{4.23}$$

where r_p and r_q are the amplitude reflection coefficients characterizing the two interfaces placed at distances z_p and z_q, respectively. The spectral amplitude of the electric field at the output of the reference arm on the other hand is defined by Eq. (4.3). The two spectra $S_a(\omega)$ and $S_b(\omega)$ recorded by a spectrometer can then be expressed as:

$$S_a(\omega) = \frac{1}{4} S_0(\omega) \Big[1 + |r_p|^2 + |r_q|^2 + \Big(r_p r_q^* e^{i(k_p(\omega) z_p - k_q(\omega) z_q)} - \\ - i r_p e^{i(k_p(\omega) z_p - k_R(\omega) z_R)} - i r_q e^{i(k_q(\omega) z_q - k_R(\omega) z_R)} + c.c. \Big) \Big], \tag{4.24}$$

$$S_b(\omega) = \frac{1}{4} S_0(\omega) \Big[1 + |r_p|^2 + |r_q|^2 + \Big(r_p r_q^* e^{i(k_p(\omega) z_p - k_q(\omega) z_q)} + \\ + i r_p e^{i(k_p(\omega) z_p - k_R(\omega) z_R)} . + i r_q e^{i(k_q(\omega) z_q - k_R(\omega) z_R)} + c.c. \Big) \Big], \tag{4.25}$$

which can be rewritten in the more convenient forms:

$$S_a(\omega) = \frac{1}{4} S_0(\omega) \Big[1 + |r_p|^2 + |r_q|^2 + 2|r_p r_q| \cos\Big(k_p(\omega) z_p - k_q(\omega) z_q + \phi_{(p-q)} \Big) + \\ + 2|r_p| \sin\Big(k_p(\omega) z_p - k_R(\omega) z_R + \phi_p \Big) + 2|r_q| \sin\Big(k_q(\omega) z_q - k_R(\omega) z_R \phi_q \Big) \Big], \tag{4.26}$$

$$S_b(\omega) = \frac{1}{4}S_0(\omega)\left[1 + |r_p|^2 + |r_q|^2 + 2|r_p r_q|\cos\Big(k_p(\omega)z_p - k_q(\omega)z_q + \phi_{(p-q)}\Big) - \right.$$
$$\left. -2|r_p|\sin\Big(k_p(\omega)z_p - k_R(\omega)z_R + \phi_p\Big) - 2|r_q|\sin\Big(k_q(\omega)z_q - k_R(\omega)z_R\phi_q\Big)\right]. \quad (4.27)$$

From the above equations, one can see that each spectrum consists of the original light source spectrum modulated by three distinct terms. The cosine term corresponds to the interference between the two sample interfaces (self-interference) while the sine terms are associated with the interference between the p and q sample interfaces and the field from the reference arm. Note that the difference between S_a and S_b lies in the sine terms with a π phase-shift. This can be directly seen from Fig. 4.5(a) which shows S_a and S_b in the absence of dispersion. In order to account for dispersion, one

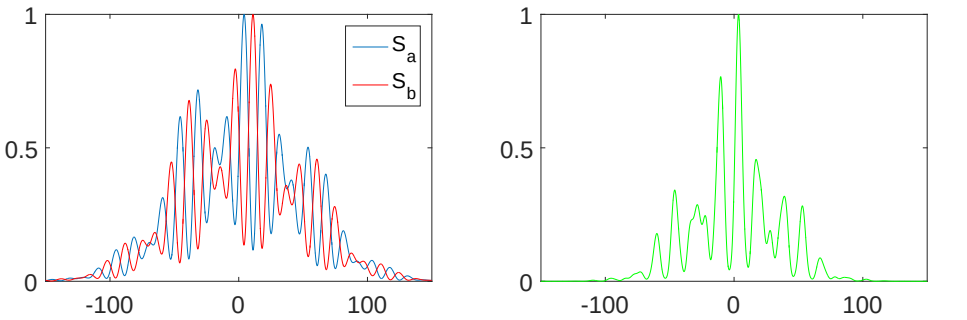

Figure 4.5: Normalized value of (a) simulated S_a and S_b spectra and (b) $C(\omega')$ function calculated from S_a and S_b for non-dispersive case.

can expand the propagation constants into Taylor-series. Keeping only the first three terms in the expansion, one obtains:

$$k_l(\omega' + \omega'_0) = \beta_l^{(0)} + \beta_l^{(1)}\omega' + \frac{1}{2}\beta_l^{(2)}\omega'^2, \quad (4.28)$$

where $l = p, q, R$ and $\beta_l^{(n)}$ is nth derivative of k_l calculated at ω'_0. One can then derive the expression for $C(\omega'_0, \omega)$ that consists of all the linear combinations of modulation frequencies present in S_a and S_b. The 0 index relates to the constant term, the pq index refers to the modulation caused by the interference between the interfaces, p

and q indexes the single interface modulation terms.

$$C(\omega_0',\omega) = \frac{1}{16} S_0(\omega-\omega_0') S_0(-\omega+\omega_0') \cdot \left(c_0 + c_{pq} + c_p + c_q + c_{p+pq} + c_{q-pq} + c_{p+q} + c_{2pq} + c_{2p} + c_{2q}\right), \tag{4.29}$$

with

$$\begin{aligned} c_0 = {} & \left(1+|r_p|^2+|r_q|^2\right)^2 \\ & + \left(r_p^2 r_q^2 e^{i\left(2\beta_p^{(0)} z_p - 2\beta_q^{(0)} z_q + 2\beta_p^{(2)}\omega'^2 z_p - 2\beta_q^{(2)}\omega'^2 z_q\right)}\right) \\ & + \left(r_p^2 e^{i\left(2\beta_p^{(0)} z_p - 2\beta_R^{(0)} z_R + 2\beta_p^{(2)}\omega'^2 z_p - 2\beta_R^{(2)}\omega'^2 z_R\right)}\right) \\ & + \left(r_q^2 e^{i\left(2\beta_q^{(0)} z_q - 2\beta_R^{(0)} z_R + 2\beta_q^{(2)}\omega'^2 z_q - 2\beta_R^{(2)}\omega'^2 z_R\right)}\right), \end{aligned} \tag{4.30}$$

$$\begin{aligned} c_{pq} = {} & \left(e^{i\left(\beta_p^{(1)}\omega' z_p - \beta_q^{(1)}\omega' z_q\right)} + c.c.\right) \\ & \cdot \left[\left(1+|r_p|^2+|r_q|^2\right) \cdot \left(r_p r_q^* e^{i\left(\beta_p^{(0)} z_p - \beta_q^{(0)} z_q + \frac{1}{2}\beta_p^{(2)}\omega'^2 z_p - \frac{1}{2}\beta_q^{(2)}\omega'^2 z_q\right)} + c.c.\right)\right. \\ & \left. + \left(r_p r_q e^{i\left(\beta_p^{(0)} z_p + \beta_q^{(0)} z_q - 2\beta_R^{(0)} z_R + \frac{1}{2}\beta_p^{(2)}\omega'^2 z_p + \frac{1}{2}\beta_q^{(2)}\omega'^2 z_q - \beta_R^{(0)}\omega'^2 z_R\right)} + c.c.\right)\right], \end{aligned} \tag{4.31}$$

$$\begin{aligned} c_p = {} & \left(-ie^{i\left(\beta_p^{(1)}\omega' z_p - \beta_R^{(1)}\omega' z_R\right)} + c.c.\right) \\ & \cdot \left[\left(1+|r_p|^2+|r_q|^2\right) \cdot \left(r_p e^{i\left(\beta_p^{(0)} z_p - \beta_R^{(0)} z_R + \frac{1}{2}\beta_p^{(2)}\omega'^2 z_p - \frac{1}{2}\beta_R^{(2)}\omega'^2 z_R\right)} + c.c.\right)\right. \\ & \left. + \left(r_p r_q^{*2} e^{i\left(\beta_p^{(0)} z_p - 2\beta_q^{(0)} z_q + \beta_R^{(0)} z_R + \frac{1}{2}\beta_p^{(2)}\omega'^2 z_p - \beta_q^{(2)}\omega'^2 z_q + \frac{1}{2}\beta_R^{(0)}\omega'^2 z_R\right)} + c.c.\right)\right], \end{aligned} \tag{4.32}$$

$$c_q = \left(-ie^{i\left(\beta_q^{(1)}\omega' z_q - \beta_R^{(1)}\omega' z_R\right)} + c.c.\right) \cdot \left[\left(1 + |r_p|^2 + |r_q|^2\right) \cdot \left(r_p e^{i\left(\beta_q^{(0)} z_q - \beta_R^{(0)} z_R + \frac{1}{2}\beta_q^{(2)}\omega'^2 z_q - \frac{1}{2}\beta_R^{(2)}\omega'^2 z_R\right)} + c.c.\right) + \left(r_p^{*2} r_q e^{i\left(-2\beta_p^{(0)} z_p + \beta_q^{(0)} z_q + \beta_R^{(0)} z_R - \beta_p^{(2)}\omega'^2 z_p + \frac{1}{2}\beta_q^{(2)}\omega'^2 z_q + \frac{1}{2}\beta_R^{(0)}\omega'^2 z_R\right)} + c.c.\right)\right], \tag{4.33}$$

$$c_{p+pq} = \left(-ie^{i\left(2\beta_p^{(1)}\omega' z_p - \beta_q^{(1)}\omega' z_q - \beta_R^{(1)}\omega' z_R\right)} + c.c.\right) \cdot \left(|r_p|^2 r_q^* e^{i\left(-\beta_q^{(0)} z_q + \beta_R^{(0)} z_R - \frac{1}{2}\beta_q^{(2)}\omega'^2 z_q + \frac{1}{2}\beta_R^{(0)}\omega'^2 z_R\right)} + c.c.\right), \tag{4.34}$$

$$c_{q-pq} = \left(-ie^{i\left(-\beta_p^{(1)}\omega' z_p + 2\beta_q^{(1)}\omega' z_q - \beta_R^{(1)}\omega' z_R\right)} + c.c.\right) \cdot \left(|r_q|^2 r_p^* e^{i\left(-\beta_p^{(0)} z_p + \beta_R^{(0)} z_R - \frac{1}{2}\beta_p^{(2)}\omega'^2 z_p + \frac{1}{2}\beta_R^{(0)}\omega'^2 z_R\right)} + c.c.\right), \tag{4.35}$$

$$c_{p+q} = -\left(e^{i\left(\beta_p^{(1)}\omega' z_p + \beta_q^{(1)}\omega' z_q\right)} + c.c.\right) \cdot \left(r_p r_q^* e^{i\left(\beta_p^{(0)} z_p - \beta_q^{(0)} z_q + \frac{1}{2}\beta_p^{(2)}\omega'^2 z_p - \frac{1}{2}\beta_q^{(2)}\omega'^2 z_q\right)} + c.c.\right), \tag{4.36}$$

$$c_{2pq} = |r_p|^2 |r_q|^2 \left(e^{i\left(2\beta_p^{(1)}\omega' z_p - 2\beta_q^{(1)}\omega' z_q\right)} + c.c.\right), \tag{4.37}$$

$$c_{2p} = -|r_p|^2 \left(e^{i\left(2\beta_p^{(1)}\omega' z_p - 2\beta_R^{(1)}\omega' z_R\right)} + c.c.\right), \tag{4.38}$$

$$c_{2q} = -|r_q|^2 \left(e^{i\left(2\beta_q^{(1)}\omega' z_q - 2\beta_R^{(1)}\omega' z_R\right)} + c.c.\right). \tag{4.39}$$

Information about the sample is contained in the interfering terms and thus obtained from the Fourier transform of the correlation function. Taking the Fourier transform of Eq. (4.29) leads to the convolution of $\mathcal{F}\left[S_0(\omega - \omega_0')S_0(-\omega + \omega_0')\right]$ with the sum of the Fourier transforms of all c_l terms. The different terms of the Fourier spectrum

corresponds to the different peaks located at different frequencies or positions. These peaks possess specific characteristics due to the properties of the c_l terms. In particular, the factor $S_0(\omega - \omega_0')S_0(-\omega + \omega_0')$ is real and even with respect to ω'. All c_l terms are real functions. One can notice that c_l terms are grouped by the common ω' term, which defines the position of the image peak. For an even c_l term, the convolution peak is real and symmetrical, whilst it is imaginary and antisymmetric when c_l is an odd function. Only the last three terms, with two frequency arguments, are independent of dispersion, which causes peaks to broaden as discussed for SOCT. All the peaks can be seen on the simulated IOCT image presented in Fig. 4.6.

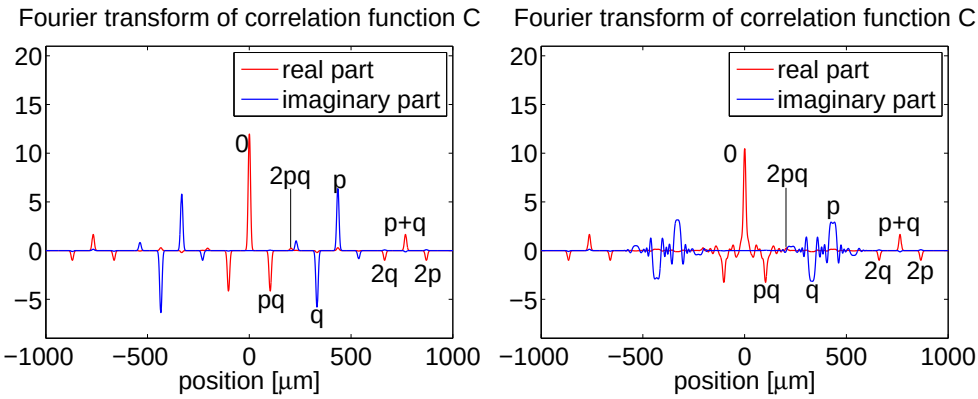

Figure 4.6: Simulated IOCT image of a sample containing two reflective interfaces with amplitude reflection coefficient 0.5, and separated by 60 μm, without uncompensated dispersion (left) and with dispersion in the system (right).

IOCT advantages

The actual interfaces of the sample correspond to the interference terms c_{2p} and c_{2q} of Eqs. (4.38) and (4.39). The Fourier transform of these terms is real and negative with a shape defined by $\mathcal{F}[S_0(\omega - \omega_0')S_0(-\omega + \omega_0')]$. This means that, for an identical light source, the width of the peaks marking the position of the interfaces is broader than in SOCT. In the case of a Gaussian spectral envelope and absence of dispersion, the peak width ratio of IOCT to SOCT is equal to $\sqrt{2}$. However, the distance separation of the interfaces terms with respect to the zero-position is twice larger than in SOCT, such that when the actual physical distance is properly rescaled the image peak width is in fact narrower by a factor of $\sqrt{2}/2$ as compared to SOCT. If dispersion is present,

this factor decreases as dispersion is inherently cancelled in ICOT unlike in SOCT. Indeed, one can see that c_{2p} and c_{2q} in Eqs. (4.38) and (4.39) do not depend on the dispersion coefficient $\beta^{(2)}$, showing how IOCT is inherently insensitive to dispersion.

An additional benefit of IOCT is the fact that the density of data points in the retrieved image is twice as high as in conventional SOCT, which allows to obtain an image with better sampling. Simulated comparison between the image peaks corresponding to one of the interfaces of the sample obtained with IOCT and OCT is plotted in Fig. 4.7 both for a dispersion-free system and a system with dispersion. The reduced width of the point spread function and better sampling are clearly observed in the case of IOCT. Nevertheless, the better sampling comes at the price of the achievable scanning depth.

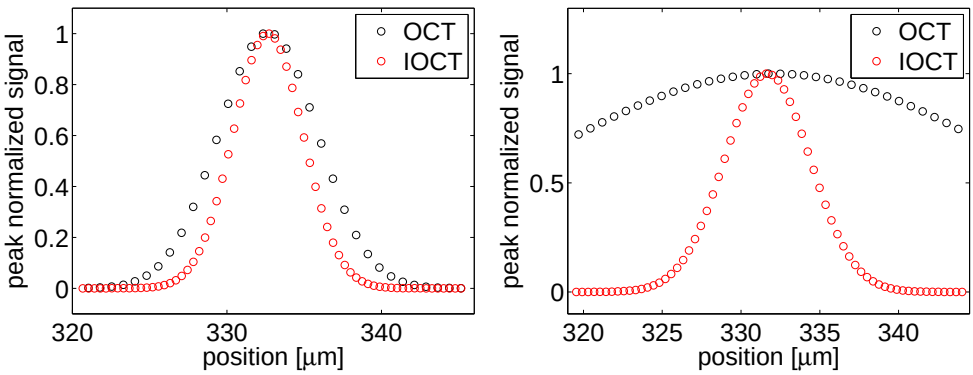

Figure 4.7: Comparison between image data points obtained from OCT and IOCT techniques in no dispersion (left) and significant amount of dispersion in the sample (right).

Specifically, the larger the optical path difference between the reference and sample arms, the shorter the oscillation period in the interference terms corresponding to the position of the interfaces. In IOCT, the oscillation period in the correlation function terms c_{2p} and c_{2q} is doubled compared to that in the interference spectrum of SOCT, thus requiring twice as dense frequency grid to be resolved. The scanning depth limit which is defined by the inverse of the spectrometer resolution is then halved compared to SOCT. The scanning depth may then be increased by using a spectrometer with a higher resolution and/or using numerical extrapolation of the frequency grid to resolve higher frequencies.

4.3 Image artefacts

Apart from the c_{2p} and c_{2q} terms which indicate the positions of the interfaces, the correlation function contains several additional terms which correspond to artefacts resulting from the cross-product of the measured interferograms. A common property to all these artefacts is their dependence on the propagation constant value at the central frequency of the source through the $e^{i(\beta_l^{(0)} z_l - \beta_m^{(0)} z_m)}$ factor. Because $\beta^{(0)}$ is the zero-order Taylor series expansion coefficient of $\beta(\omega)$, it naturally depends on the frequency ω_0' around which the expansion is performed. In principle $\beta^{(0)} = \beta^{(0)}(\omega_0')$ changes approximately linearly as a function of ω_0' and therefore the amplitude of the image peaks corresponding to artefacts in the Fourier spectrum of the correlation function will oscillate as the central frequency of the light source is changed. Varying the central frequency in IOCT technique is straightforward and can be done numerically through data processing without any additional measurement, providing a convenient means to discriminate artefacts as shown in [91].

An illustration of the change in amplitude of the image peaks corresponding to artefacts as the central wavelength of the source is varied is shown in Fig. 4.8. We can see how the oscillation period depends on the relative distance between the interfaces producing a particular artefact. For example, the c_p and c_q terms generate an artefact at p+q position which oscillates slowly due to the small distance between p and q interfaces. The artefact at p-q position on the other hand oscillates with a shorter period due to the larger distance between p and -q positions. Note also that some artefacts are produced by more than one combination of interfaces, and in that case multiple modulation frequencies are present in the artefact. A straightforward solution to discriminate the artefacts is to solely consider the real part of the Fourier spectrum of the correlation function $\mathbf{F}(C)$ and averaging as the central frequency of the source is varied. In this case, similar to ref. [92], the oscillating amplitude of the artefact peaks averages out whilst the constant amplitude of the real image peaks remains unchanged as discussed in ref. [79]. An example of this procedure is presented in Fig. 4.9 in the absence of dispersion and we can clearly see how the averaging completely removes the presence of artefacts. Note also that the change of the image peak position arising from the change in the group-delay provides information about the dispersion in the system. Unfortunately, this approach only performs well when there is no dispersion in the system. This is because the c_{2p} and c_{2q} terms which determines the position of the two interfaces depends on the group-delay $\beta^{(1)}$ through

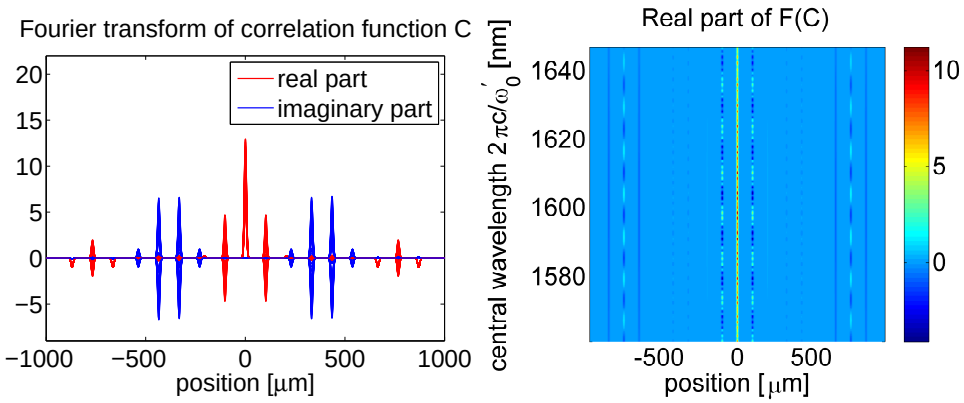

(a) (b)

Figure 4.8: Simulated oscillation of the artefact peaks in an IOCT image as the central frequency ω_0' is varied. (a) real and imaginary part of $\mathbf{F}(C)$ for several central wavelengths, (b) color plot of the real part of $\mathbf{F}(C)$.

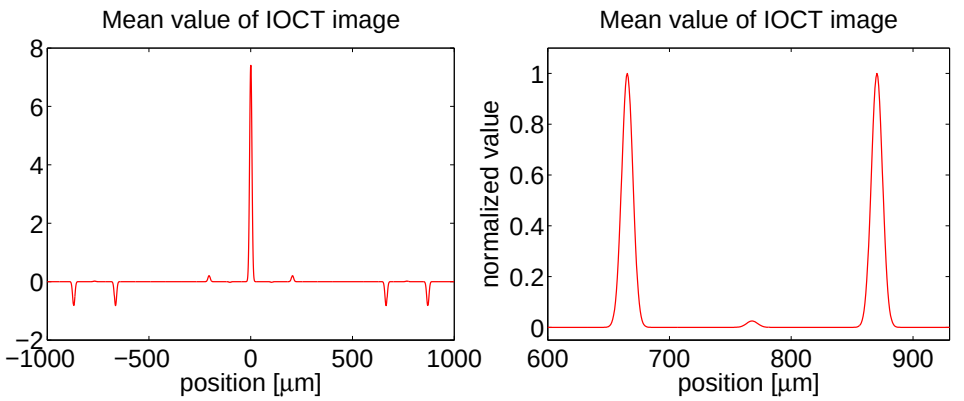

(a) (b)

Figure 4.9: IOCT image with artefacts averaging in the nondispersive case, (a) mean value of data presented in Fig. 4.8(b), (b) normalized view of the image peaks.

the $e^{i\left(2\beta_q^{(1)}\omega' z_q - 2\beta_R^{(1)}\omega' z_R\right)}$ term which includes the first-order dispersion parameter. The group-delay value depends on the central frequency $\beta^{(1)}(\omega_0')$, which then varies when the central frequency is changed and, in turn, modifies the position of the associated image peak. Specifically, the position of the peak varies linearly with the central frequency with a slope proportional to the amount of dispersion in the system before the sample interface as illustrated in Fig. 4.10. Note, however, that the width of the

point spread function at a single central frequency (i.e. in a given cross-section in Fig. 4.10) remains unaffected by dispersion. Therefore, whilst averaging the measurement over multiple central frequencies will generally lead to the broadening of the width of the point spread function, averaging along the dispersion slope will eliminate the artefacts without degrading the resolution. An alternative is simply to identify the artefact by varying the central wavelength and subsequently consider only a single scan corresponding to one specific central frequency.

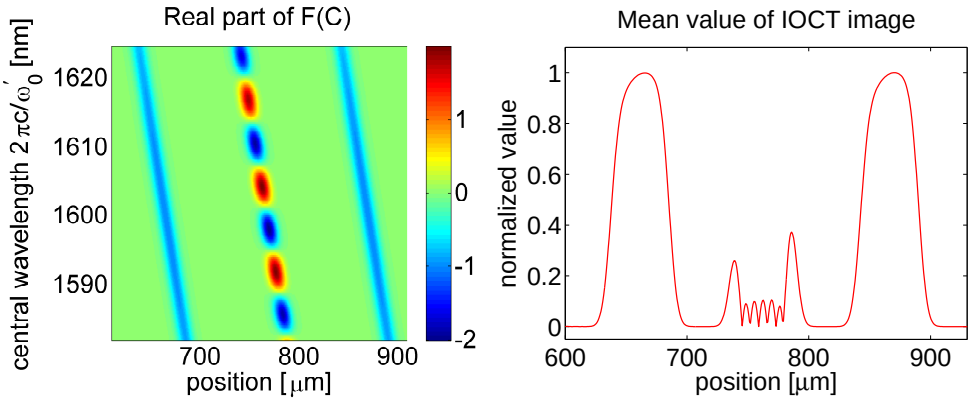

(a) (b)

Figure 4.10: IOCT image with artefacts averaging in the dispersive case. (a) color plot of the real part of $F(C)$ as a function of position and central wavelength, (b) mean value of the data projection from plot (a), normalized to the peak value.

Higher-order dispersion

The correlation function used in IOCT produces an image where the real interfaces' position is not affected by even-order dispersion coefficients (in contrary to the artefacts as discussed above). Yet, odd-order dispersion is not inherently cancelled and, when broadband light is used, or in highly dispersive materials, third-order dispersion results in the asymmetrical broadening of the image peaks with the presence of oscillation on its trailing edge. The image peaks lines on $F(C)(\omega_0')$ then have a quadratic dependence on the central frequency ω_0' as seen in Fig. 4.11.

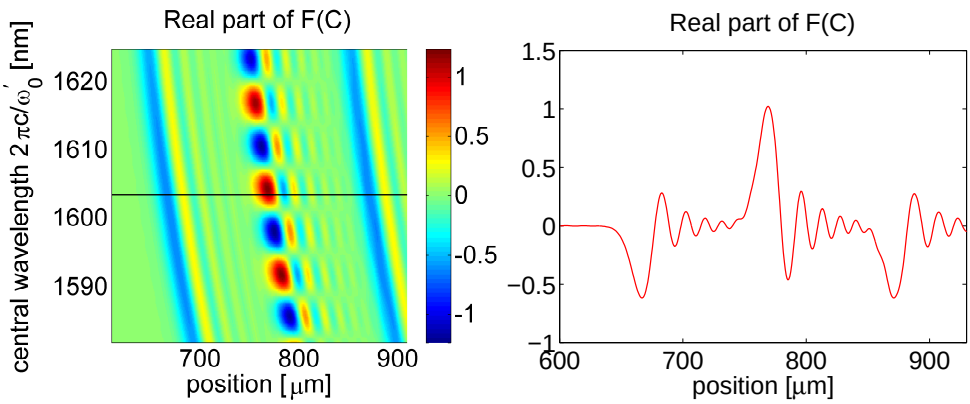

Figure 4.11: IOCT image affected by third order dispersion. (a) color plot of the real part of $F(C)$ as a function of position and central wavelength. (b) cross-section from (a) indicated by the solid black line.

4.4 Precision vs resolution of the measurement

IOCT possesses a narrower point spread function with a larger amount of data points compared to that of SOCT. This characteristics allows to determine the physical position of reflective interfaces with a better precision. The precision with which the position of the interfaces is determined cannot in fact be better than what would be expected from the width of the point spread function. This is because the precision can be treated as a systematic error of the fit defined by multiple measurement data points or as the distance between the two measurement points with the largest amplitude. If two interfaces are sufficiently far apart such that their corresponding peaks in the Fourier spectrum of the correlation function do not overlap, the precision of the position is identical for each interface. If the interfaces separation reduces, the peaks merge, eventually becoming indistinguishable. The minimum distance for which one can still determine the position of the two interfaces defines the resolution of the system. In general, the resolution exceeds the precision of a single interface measurement. One can explain that paradox from the fact that the a priori knowledge that there is a single interface provides additional information. Without this a priori knowledge, one can only state that there is no other interface outside the image peak but there could well be in fact two closely separated interfaces producing a single image peak. This justifies why the resolution of SOCT measurement is generally defined by the FWHM

of the point spread function. If two interfaces are separated by a distance exceeding the FWHM of the point spread function, they can then be resolved.

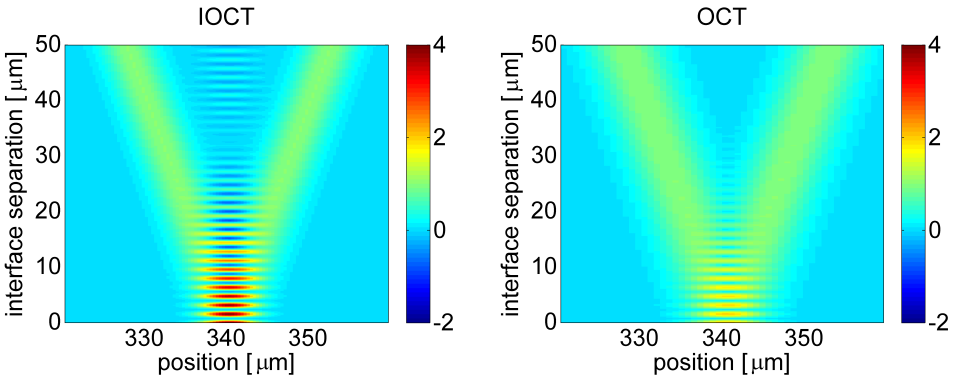

(a) (b)

Figure 4.12: Simulated image of two interfaces with decreasing separation. (a) IOCT image, with artefact averaging, normalized to the peak value produced by a single interface, (b) OCT image normalized to the peak value produced by a single interface. For easier comparison the same colour scale is used in both plots.

Figure 4.12 shows the simulated image of two interfaces with decreasing separation and without dispersion, as would be measured by IOCT (a) and SOCT (b). In the case of IOCT, we apply the method previously described to remove the artefact. Whilst the artefact vanishes if the interfaces separation is relatively large, it is still present for separations exceeding 20 microns such that the two interfaces become undistinguishable at a larger separation than it does with SOCT. This suggest that IOCT does not provide any benefit for resolving multiple interfaces. However the situation is different when a significant amount of dispersion is present in the sample or measurement system as seen in Fig. 4.13. Here, no artefact cancellation method is applied. In the dispersive case, IOCT allows to distinguish the two interfaces down to a similar separation of about 20 microns as in the non-dispersive case whereas the large increase in the point spread function of SOCT renders the interfaces difficult to distinguish for separations shorter than 40 microns. This is because dispersion is inherently compensated for in the IOCT technique.

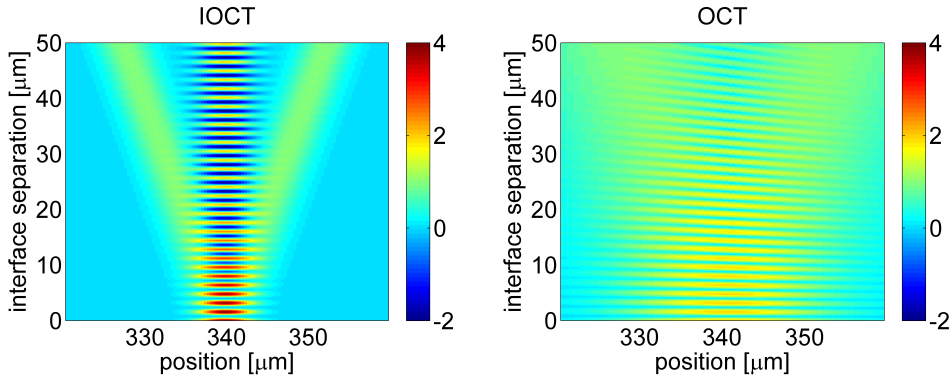

(a) (b)

Figure 4.13: Simulated image of two interfaces with decreasing separation and dispersion present in the system. (a) IOCT image, without artefact averaging, normalized to the peak produced by a single interface, (b) OCT image normalized to the peak produced by a single interface. The same colour scale is used in both plots.

4.5 Experimental realization of Intensity Optical Coherence Tomography

Experimental demonstration of IOCT was demonstrated in publication P2 using the set-up presented in Fig. 4.14. The light source is a superluminescent, fiber-coupled, light emitting diode with a Gaussian spectrum centred at 1604-nm and 55-nm FWHM bandwidth. The beam is divided between the sample and reference arms with a 50/50% beam-splitter (BS1). In the reference arm, an additional beam splitter BS2 is inserted to equalize the optical path in both arms before reaching beam splitter BS3 where the two beams are recombined. Light at the output of BS3 is then collimated into two single-mode fibers and guided directly to the entrance slit of an imaging spectrograph which measures simultaneously the spectral intensities of both beams.

The reduced width of the point spread function and cancellation of second-order dispersion was demonstrated by preforming measurements of a single interface in the form of a reflecting mirror. A 32-cm long glass cube was intentionally inserted in the sample arm to introduce significant amount of dispersion in the measurement system. Note that light passes through the glass twice, resulting in a total amount of 64 cm of dispersive material. Measurements results are presented in Fig. 4.15 both for SOCT and IOCT, confirming the two benefits of IOCT, in excellent agreement with

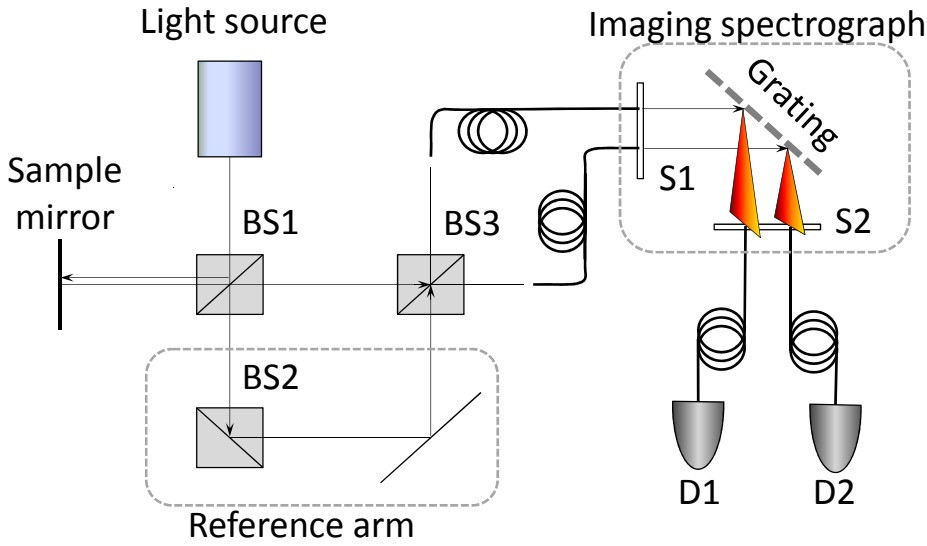

Figure 4.14: IOCT experimental set-up, BS- 50/50 cube beam-splitter, S1,S2 input and output slits of imaging spectrograph, D1, D2 - sensor diodes recording two IOCT channel spectra.

the theory. We also investigated the case of two interfaces using a microscopic glass cover as the sample to be characterized. The results presented in Figure 4.16 agrees very well with the theoretical prediction, and in particular we can see how the artefact amplitude oscillate as the central wavelength of the light source spectrum varies allowing to unambiguously discriminate the artefacts from the two actual interfaces whose amplitude remains constant.

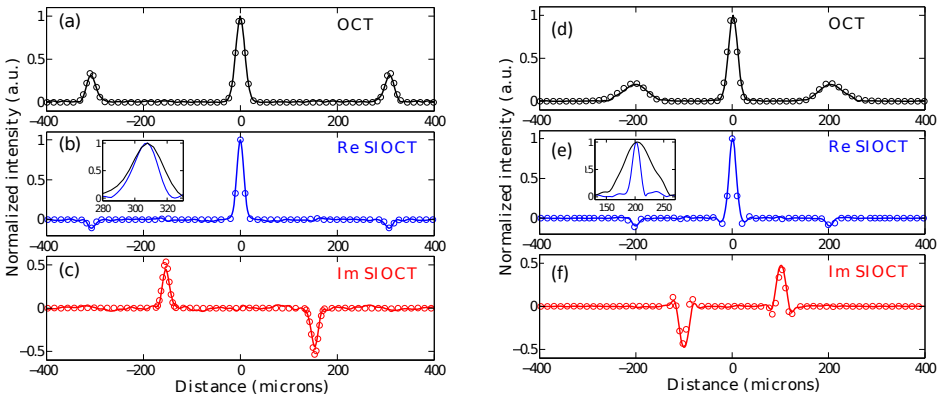

Figure 4.15: Comparison between the measurement performed without dispersion present in the set-up (a-c) and measurement performed with significant amount of second-order dispersion present in the set-up (d-f). Normalized image peak of OCT can be compared with the normalized IOCT image peak in the inset of plot (b) and (d). For each plot, the circles represent the experimental data and the solid lines show the theoretically calculated signal.

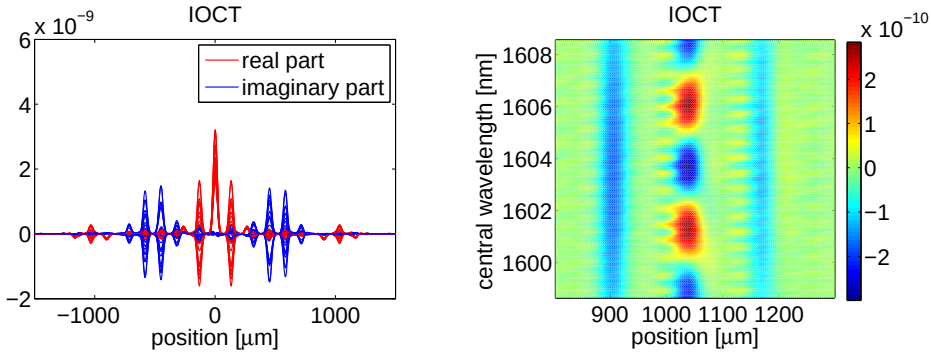

(a) (b)

Figure 4.16: IOCT image of a two-interface sample. (a) overlay of real and imaginary parts of $F(C)$ calculated for different central frequencyω_0', (b) color plot of the real part of IOCT data corresponding to the sample.

Chapter 5

Temporal Ghost Imaging

In this chapter, we first introduce the concept of Ghost Imaging in the spatial domain where it was originally developed. We then proceed to extend it to the temporal domain, showing how ultrafast signals can be retrieved blindly with this new technique as demonstrated in publication P3. We also demonstrate an approach to magnify the retrieved temporal ghost signal, allowing to overcome the resolution limitations of the standard time-domain ghost imaging (demonstrated in publication P4).

5.1 Ghost Imaging in the spatial domain

Ghost Imaging uses the correlation between a known structured pattern that illuminates an object and the total (integrated) intensity transmitted (or reflected) by the object to create an image[93–99]. The specificity of ghost imaging is that neither of the beams alone actually carries enough information to construct an image of the object. The main advantage of ghost imaging lies in the fact that it is insensitive to distortions of the wavefront occurring after the object, as only the total light intensity is measured.

Ghost imaging was first proposed in the spatial domain[100–105] with a set-up similar to the one presented in Fig. 5.1. Light from a spatially coherent source is transmitted

through a diffusive rotating plate that randomly modifies the phase and creates a varying speckle pattern. The beam is then split by a beam splitter into a reference beam whose intensity is imaged with a high resolution camera and a sample beam which passes through (or is reflected from) the object and is captured by a "bucket detector" (BD)- a single pixel detector with no spatial resolution. The image of the speckle illumination and the total light intensity from the bucket detector are then correlated numerically with a computer over multiple speckle patterns corresponding to different position of the rotating diffusive plate. Note that for a successful image reconstruction, the illuminating speckle pattern must be recorded exactly as it arrives on the object. This implies that the distances from the beam splitter to the object and to the ghost plane (corresponding to the plane where the speckle pattern is recorded) should be equal. The correlation procedure is performed for each pixel of the high

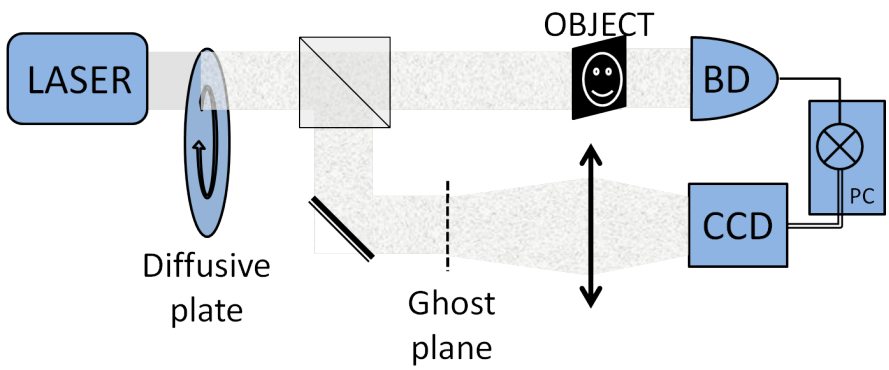

Figure 5.1: Spatial domain ghost imaging scheme. BD - single pixel "Bucket Detecor", CCD - charged coupled device camera.

resolution camera separately, i.e. the intensity values recorded by the individual pixels are correlated with the bucket detector signal measured for each speckle pattern. One can also see this procedure as the weighted sum of all the pictures recorded by the camera with the mean level of each pixel subtracted. The weight of each picture is defined by the bucket detector deviation from its mean detected signal (over all the realizations). Adding a large number of pictures produces the image of the object just as it would be standing like a ghost in the focus plane of the camera, although the camera actually never recorded light that interacted with the real physical object.

Space-time duality

Due do the similarities between the mathematical description of diffractive light propagation in space (Eq. (2.33)) and dispersive light propagation (Eq. (2.50)) in time, one can formally establish several space-time symmetries [106,107] as schematically illustrated in Fig. 5.2. More specifically, for a field propagating in the z-direction, the transverse position in space is equivalent to the duration in time such that there is a direct correspondence between spatial light distribution and temporal variations. In the spectral domain, angular frequencies k_x in space are the equivalent of the light angular frequency $\omega - \omega_0$ in the spectrum. The propagation distance z in the spatial case corresponds in the time domain to the total amount of dispersion accumulated $\beta^{(2)}\omega_0 z$. Because of such space-time duality, one can transfer many concepts from light propagation in space into the time domain.

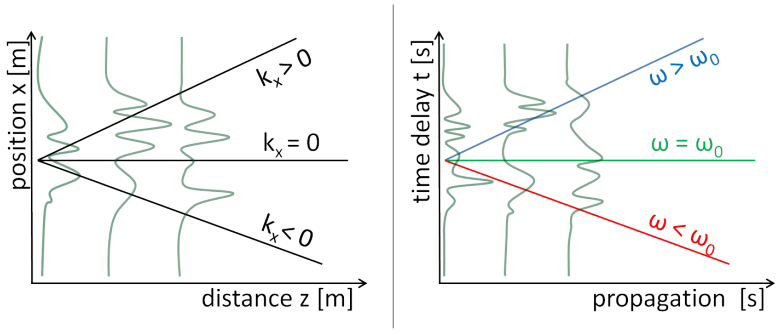

Figure 5.2: Symmetry between temporal and spatial propagation. The beam with angular frequency k_x changes position while propagating through space similar to the frequency component ω changing its delay in time while propagating in a dispersive medium.

5.2 Temporal Ghost Imaging with a Chaotic Laser

Temporal Ghost Imaging (TGI) [108,109] is the analogue of spatial ghost imaging transposed to the time domain. It is used to image temporal objects - a time-varying transmission, absorption, reflection or phase. The concept of temporal ghost imaging was originally proposed theoretically in Ref. [110]. A schematic illustration of TGI is presented in Fig. 5.3. A temporally incoherent light source is used to produce random

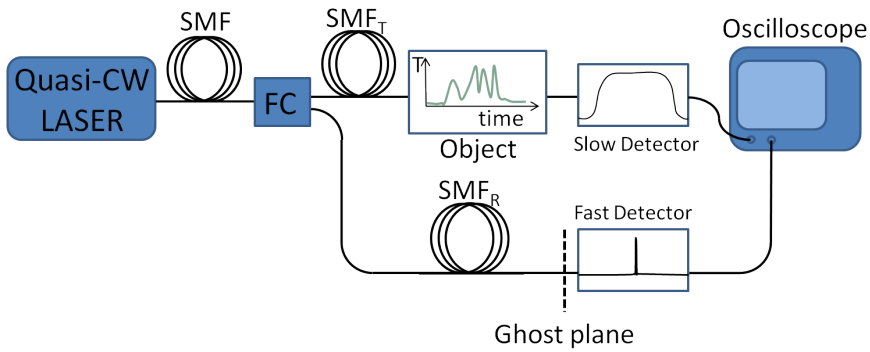

Figure 5.3: Basic temporal ghost imaging scheme. FC- fiber coupler, SMF - single-mode fiber, The imaging condition requires that lengths of fibers in the reference arm $\mathrm{SMF_R}$ and the object arm $\mathrm{SMF_T}$ are equal.

intensity fluctuations - the time domain equivalent of the speckle pattern. The light is then divided between two identical fibers of the same length, which ensures that both beams accumulate the same amount of dispersion. Light from the first fiber interacts with a temporal object in the form of a time-varying transmission $T_{obj}(t)$ generated by a modulator which changes the light intensity. The transmitted light is then measured with a slow photo-detector that only records the total (integrated) intensity I_{test}:

$$I_{\mathrm{test}} = \int_{\Delta t} I_{\mathrm{inc}}(t) \cdot T_{obj}(t) dt, \tag{5.1}$$

where Δt is the window duration of a single measurement. This slow detector is the analogue of the bucket detector in the spatial ghost imaging scheme.

The light intensity $I_{\mathrm{ref}}(t)$ from the second fiber is recorded with a fast photo-detector that provides a high temporal resolution measurement of the random intensity fluctuations:

$$I_{\mathrm{ref}}(t) = \int_{-\infty}^{+\infty} I_{\mathrm{src}}(t+\tau) \cdot T_D(\tau) d\tau, \tag{5.2}$$

where $I_{\mathrm{src}}(t)$ is the source temporal intensity at the object and $T_D(t)$ is the fast diode response function. The signal recorded by the fast detector is then the convolution of the source fast varying intensity with the detector response function.

The measurement is repeated multiple times for different (random) light intensity patterns transmitted through the object which is then simply reconstructed from the

correlation function $C(t)$ given by:

$$C(t) = \frac{\langle \Delta I_{\text{ref}}(t) \cdot \Delta I_{\text{test}} \rangle_N}{\sqrt{\langle [\Delta I_{\text{ref}}(t)]^2 \rangle_N \langle [\Delta I_{\text{test}}]^2 \rangle_N}}, \tag{5.3}$$

where $\langle \dots \rangle_N$ represents the average over all realizations and $\Delta I = I - \langle I \rangle_N$. Note that the correlation function $C(t)$ only retrieves the shape of the object and normalization is required in order to find the value of $T_{obj}(t)$ amplitude.

The fact that the correlation function $C(t)$ is calculated from a finite number of realizations leads to uncertainty in the object reconstruction. The uncertainty can be estimated from the error function $SE[C(t)]$ that can be approximated by[111]:

$$SE[C(t)] = \frac{1 - C^2(t)}{\sqrt{N}}. \tag{5.4}$$

One can see that the error function is inversely proportional to the square root of the number of realizations, but that it also depends on the correlation value itself. This means that, in principle, if the correlation is close to 1 the error can be kept very small even for a low number of realizations. However, this situation can only occur in a specific case as described in the next section.

Estimation of the correlation function for an incoherent light source

The shape of the correlation function $C(T)$ can be estimated from the experimental measurement parameters, assuming an infinite number of realizations. For simplicity, we assume a discrete time grid divided into elementary time steps rather than continuous functions.

We define a vector I which represents the light intensity as a function of time. This means that the vector components I_i represent the light intensity at a specific time t_i. The I_i values are taken to be random and independent of each other. In order to account for the spectral properties of the light source, I is convolved with the function T_S defined by the Fourier transform of the light spectrum and representing the average source intensity fluctuation. The width of $T_S(t)$ is equal to the grid temporal spacing and does not affect the I_i values substantially, but it enables to account for the finite spectral width of the light source. The convolution limits the

fluctuations period according to the spectral bandwidth while maintaining the random nature of the source. Light irradiating the object I_{inc} is then defined as:

$$(I_{\text{inc}})_i = \sum_j I_{i+j} \cdot (T_S)_j. \tag{5.5}$$

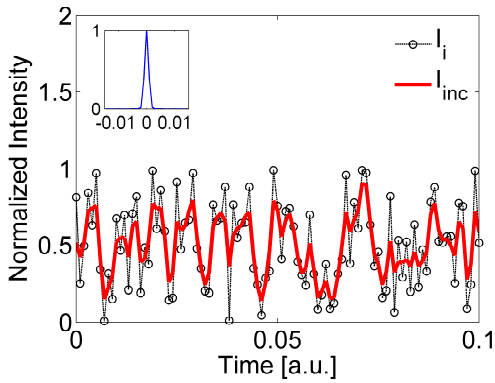

Figure 5.4: Relation between I (black) and I_{inc} (red) in single TGI measurement realization. The inset shows the source characteristic fluctuation shape T_S (blue) defined by the light spectrum. The inset axes are in the same scale as the main plot axes.

The light intensity recorded by the bucket detector is the total light intensity transmitted through the object, which can be calculated as:

$$\begin{aligned} I_{\text{test}} = \sum_i (I_{\text{inc}})_i \cdot (T_{obj})_i &= \left(\sum_i I_i \cdot (T_{obj})_i \right) \cdot \left(\sum_j (T_s)_j \right) \\ &= \sum_i I_i \cdot (T_{obj})_i \cdot (T_S)_{sum}. \end{aligned} \tag{5.6}$$

An example of light intensity pattern that is transmitted through the object is shown in Fig. 5.5(a).

The light recorded by the fast photodetector is given by the convolution of I_{inc} with

the detector response function T_D:

$$(I_{\text{ref}})_i = \sum_k \left((I_{\text{inc}})_{i+k}\right)(T_D)_k = \sum_k \left(\sum_j I_{i+j+k} \cdot (T_S)_j\right) \cdot (T_D)_k$$
$$= \sum_j I_{i+j} \cdot \left(\sum_k (T_S)_{j+k} \cdot (T_D)_k\right). \tag{5.7}$$

Thus, I_{ref} corresponds to the random field emitted by the light source convolved with the convolution T_{SD} of the source fluctuation function and the detector response function:

$$(I_{\text{ref}})_i = \sum_j I_{i+j} \cdot (T_{SD})_j. \tag{5.8}$$

An example of I_{ref} is illustrated in Fig. 5.5(b).

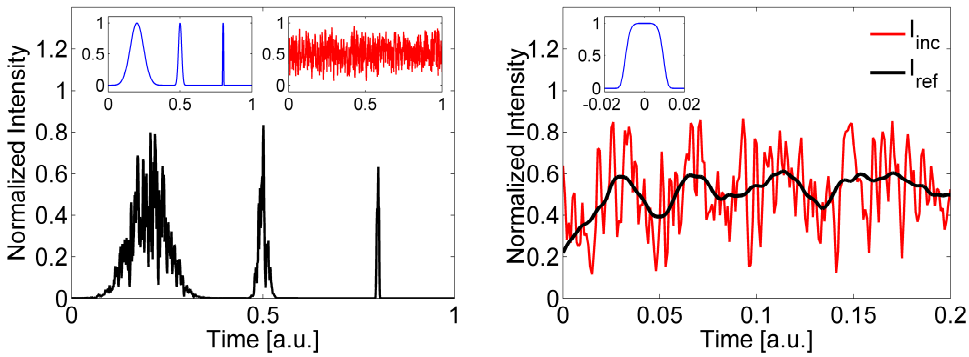

(a) (b)

Figure 5.5: (a) (black) Light transmitted through the object T (inset, blue), light I_i incident on the object is shown in red in the inset plot. The integrated signal of the black curve corresponds to the bucket detector measurement. The inset axes present the same time interval as the main plot axes. (b) Example of I_{ref} (black) calculated as the convolution of I_{inc} (red) with the detector response function T_D (inset, blue). The inset axes are in the same scale as the main plot axes.

The correlation function $C(t) \equiv C_i$ can be rewritten as:

$$C_i = Cor\left[(I_{\text{ref}})_i, I_{\text{test}}\right] = \frac{Cov\left[(I_{\text{ref}})_i, I_{\text{test}}\right]}{\sqrt{Var\left[(I_{\text{ref}})_i\right) \cdot Var(I_{\text{test}})]}}, \tag{5.9}$$

where Cor, Cov and Var stands for correlation, covariance and variance functions, respectively. After substituting expressions from Eq. (5.6) and Eq. (5.8), one can use

the linear properties of the covariance function applied to each of the elements of Eq. (5.9):

$$\begin{aligned} Cov\left((I_{\text{ref}})_i, I_{\text{test}})\right] &= Cov\left[\sum_j I_{i+j}\cdot(T_{SD})_j\ ,\ \sum_k I_k\cdot(T_{obj})_k\cdot(T_S)_{sum}\right] = \\ &= \sum_j\sum_k Cov\left[I_{i+j}\cdot(T_{SD})_j\ ,\ I_k\cdot(T_{obj})_k\cdot(T_S)_{sum}\right] = \\ &= \sum_j\sum_k (T_{SD})_j\cdot(T_{obj})_k\cdot(T_S)_{sum}\cdot Cov\left(I_{i+j}\ ,\ I_k\right). \end{aligned} \tag{5.10}$$

Due to the fact that I_i and I_k are independent random variables, their covariance is equal to zero unless $i = k$. Other factors in the correlation equation can be calculated as:

$$\begin{aligned} Cov\left[(I_{\text{ref}})_i, I_{\text{test}})\right] &= \sum_j\sum_k (T_{SD})_j\cdot(T_{obj})_k\cdot(T_S)_{sum}\cdot Cov\left(I_{i+j}\ ,\ I_k\right)\cdot\delta_{i+j,k} = \\ &= \sum_j (T_{SD})_j\cdot(T_{obj})_{i+j}\cdot(T_S)_{sum}\cdot Cov\left(I_{i+j}\ ,\ I_{i+j}\right) = \\ &= (T_S)_{sum}\cdot\sum_j (T_{SD})_j\cdot(T_{obj})_{i+j}\cdot Var\left(I_{i+j}\right), \end{aligned} \tag{5.11}$$

$$\begin{aligned} Var\left[((I_{\text{ref}})_i)\right] &= Cov\left[\sum_j I_{i+j}\cdot(T_{SD})_j\ ,\ \sum_k I_{i+k}\cdot(T_{SD})_k\right] = \\ &= \sum_j\sum_k Cov\left[I_{i+j}\cdot(T_{SD})_j\ ,\ I_{i+k}\cdot(T_{SD})_k\right] = \\ &= \sum_j\sum_k (T_{SD})_j\cdot(T_{SD})_k\cdot Cov\left(I_{i+j}\ ,\ I_{i+k}\right) = \\ &= \sum_j\sum_k (T_{SD})_j\cdot(T_{SD})_k\cdot Cov\left(I_{i+j}\ ,\ I_{i+k}\right)\cdot\delta_{i+j,i+k} = \\ &= \sum_j (T_{SD})_j^2\cdot Var(I_{i+j}), \end{aligned} \tag{5.12}$$

$$
\begin{aligned}
Var\left[(I_{\text{test}})\right] &= Cov\left[\sum_i I_i \cdot (T_{obj})_i \cdot (T_S)_{sum}\ ,\ \sum_k I_k \cdot (T_{obj})_k \cdot (T_S)_{sum}\right] = \\
&= \sum_i \sum_k (T_{obj})_i \cdot (T_{obj})_k \cdot (T_S)^2_{sum} Cov\left(I_i\ ,\ I_k\right) = \\
&= (T_S)^2_{sum} \cdot \sum_i (T_{obj})^2_i \cdot Var\left(I_i\right). \qquad (5.13)
\end{aligned}
$$

Finally after substituting Eqs. (5.11-5.13) into Eq. (5.9) one obtains:

$$
C_i = \frac{\sum_j (T_{obj})_{i+j} \cdot (T_{SD})_j \cdot Var(I_{i+j})}{\sqrt{\left(\sum_j (T_{SD})^2_j \cdot Var(I_{i+j})\right) \cdot \left(\sum_i (T_{obj})^2_i \cdot Var(I_i)\right)}}. \qquad (5.14)
$$

Assuming that the intensity statistics are stationary (i.e. independent of time), one can reduce $Var(I_i)$ to:

$$
C_i = \frac{\sum_j (T_{obj})_{i+j} \cdot (T_{SD})_j}{\sqrt{\left(\sum_j (T_{SD})^2_j\right) \cdot \left(\sum_j (T_{obj})^2_j\right)}}. \qquad (5.15)
$$

Taking the limit to a continuous function, one finally obtains:

$$
C(t) = \frac{\int_{\Delta t} T_{obj}(t+\tau) \cdot T_{SD}(\tau) d\tau}{\sqrt{\int_{\Delta t} T^2_{SD}(\tau) d\tau} \cdot \sqrt{\int_{\Delta t} T^2_{obj}(\tau) d\tau}}. \qquad (5.16)
$$

The correlation function of Eq. (5.16) follows the shape of the object transmission $T_{obj}(t)$ convolved with the fast detector response and the light intensity fluctuations $T_{SD}(t)$. This implies that the detector speed and the light spectrum affects the correlation value. The influence of the object duration and detector response on the correlation function value are illustrated in Figs. 5.6 and 5.7, respectively. According to the Cauchy-Schwarz inequality, it is possible to obtain $C(t) = 1$ only if the object transmission function is exactly equal to the convolution of the source temporal oscillation and detector response $T(t+\tau) = T_{SD}(t)$, as shown in Fig. 5.6(a). In cases where $T_{SD}(t)$ differs from the object transmission function (in terms of profile or duration), the correlation value is reduced. This means that $T_{SD}(t)$ also defines the temporal resolution of the measurement, with a trade-off between high correlation signal value and high temporal resolution.

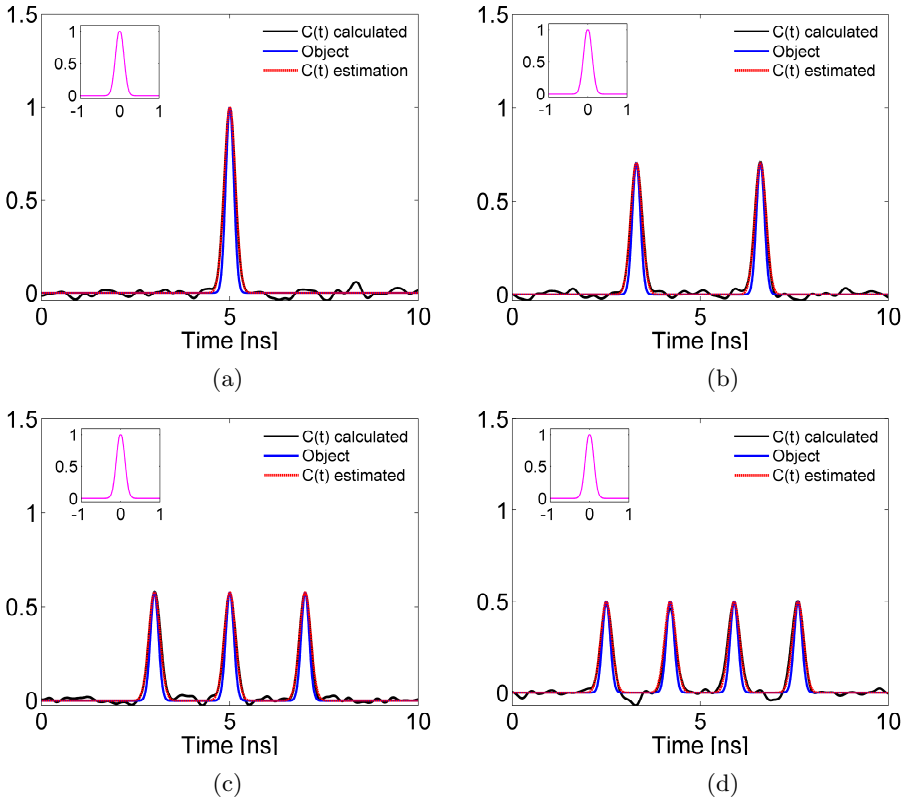

Figure 5.6: Simulated TGI images. The temporal object (blue) is normalized to the height of the estimated correlation function (red) which can be compared with the actual correlation function (black) calculated for N=3200 realizations. The total object transmission time is increased by adding extra pulse fo each plot. All the simulations are performed with the same $T_{SD}(t)$ function (shown in the inset). The time scale of the inset is identical to that of the main plot. $T_{SD}(t)$ has been chosen to correspond precisely to the object time-dependent transmission for a single pulse.

To estimate the maximum $C(t)$ value, one can assume that the temporal width of T_{SD} is shorter than the object duration. In this case, the integrals in Eq. (5.16) are easily calculated, and the maximum of the correlation function C_{max} is found to be:

$$C_{max} \approx \frac{\Delta T_{SD}}{\sqrt{\Delta T_{obj} \cdot \Delta T_{SD}}} = \sqrt{\frac{\Delta T_{SD}}{\Delta T_{obj}}}, \tag{5.17}$$

where ΔT_{obj} is the total duration of the object transmission and ΔT_{SD} is the temporal width of T_{SD} function. Within this approximation, the maximum of the correlation function is defined by the square root of the ratio of the resolution to the object duration. Keeping in mind the result of Eq. (5.4), one can estimate the signal-to-noise ratio (SNR) of the measurement as:

$$\mathrm{SNR} = \frac{C_{max}}{SE(C)} \approx \sqrt{\frac{\Delta T_{SD}}{\Delta T_{obj}}} \cdot \sqrt{N}. \tag{5.18}$$

Therefore, in order to increase the temporal resolution by a factor of 2 while keeping the SNR constant, the number N of realizations over which the correlation between the two signals is calculated must be doubled. From the above, one can estimate that imaging an object with a duration 100-times longer than the measurement resolution will result in a correlation function with amplitude 0.1. In this case, in order to achieve a SNR equal to 100, one needs to perform $N = 1\ 000\ 000$ distinct measurements with randomly varying temporal fluctuations.

The result above is only exact for the binary-type function (i.e. taking discrete values 0 or 1), but it underestimates the correlation value for other types of T_{obj} and T_{SD} functions. Yet, when changing the duration of a function with a given shape, the correlation variation is proportional to that obtained from the indicator-type function. For example, if an object of any shape produces a correlation value X, an object with duration twice as long (and identical shape) will result in a correlation value $\mathrm{X}/\sqrt{2}$. A similar relation holds for the T_{SD} function temporal width which defines the resolution of the measurement: increasing the resolution twice decreases the correlation function by a factor of $\sqrt{2}$. This behaviour is illustrated in Fig. 5.7. Note that if the light source fluctuations time ΔT_S (defined as the temporal width of $T_S(t)$) is much shorter than the fast detector response time, T_S should not affect the retrieved object quality. This is because in that case the detector response time becomes equal to the convolution function $T_{SD}(t)$. From a theoretical point of view, as was assumed in this section, it

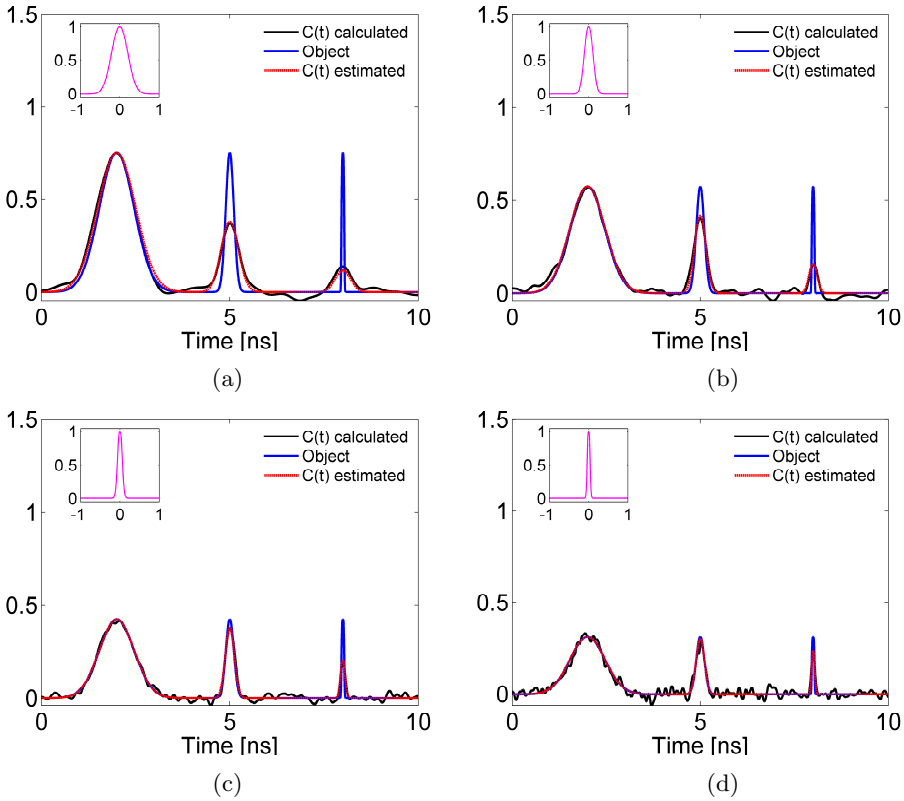

Figure 5.7: Simulated TGI images. Temporal object (green) is normalized to the height of estimated correlation function (red) which can be compared with actual correlation function (black) calculated for N=3200. The resolution is increased by a factor of two between each plot. Each inset shows the $T_{SD}(t)$ function being the effective resolution. The time scale of the inset is identical to that of the main plot.

does not mater how short ΔT_S is. However in practice, if the source random intensity fluctuations are much shorter than the fast detector response time, the fast intensity fluctuations are partially averaged by the detector, the constant component of the signal increases and the modulation amplitude decreases. From a purely computational consideration this is not a problem in principle as the correlation function subtracts the average value of the signal and normalizes the fluctuation amplitude. But in practice, this might become an issue possibly causing the recorded fluctuations to be lost in the detector noise. In order to avoid this, as a rule of thumb, one should then use light sources with a characteristic fluctuations time on the order of (but still shorter than) the fast detector response time.

5.3 Experimental realization of Temporal Ghost Imaging

The theory of ghost imaging in the time-domain was confirmed in publication P3 using the experimental set-up shown in Fig. 5.3 [112]. The light source is a fiber coupled multi-mode laser with a Gaussian spectrum centred at 1546-nm and 0.6-nm bandwidth (FWHM). The corresponding source coherence time (estimated from the spectral bandwidth) is $\Delta T_S = 13\ ps$. The reference signal was recorded with a 25 GHz bandwidth photodiode and a 20 GHz, 50 Gsamples/s real-time oscilloscope. The light intensity produced by the source, convolved with the photodiode and oscilloscope response time produced effective source fluctuations with a characteristic time $\Delta T_{SD} \approx 50\ ps$. Examples of recorded intensity fluctuations are shown in Fig. 5.8. A temporal object was created with an electro-optic intensity modulator driven by a bit pattern generator resulting in the transmission function plotted in Fig. 5.9 with features as short as 100 ps. The programmed pattern was repeated every 50 ns and the first bit in the sequence was used to trigger (with a proper delay) the recording time window of the oscilloscope. Note that synchronization of the object and measurement time window is crucial for successful imaging, as otherwise the "ghost object" would change position in time and the retrieved image would be significantly distorted. The light transmitted through the object was recorded by 1.2 GHz diode and integrated over 5 ns long measurement window duration, effectively resulting in 0.2 GHz bandwidth for the test arm detector. For comparison purposes a direct measurement of the object was performed with the fast detector placed in the object arm. The results of the ghost measurement for $N = 100,000$ distinct realizations are shown in Fig. 5.9 and we can see how the ghost imaging results are in excellent agreement with a direct measurement of the temporal object. The influence of the number of measurements and detector speed on the image quality is illustrated in Fig. 5.10, confirming the theoretical predictions from the previous section.

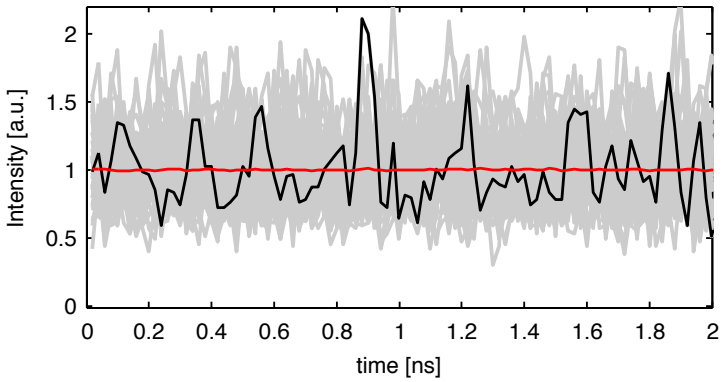

Figure 5.8: Recorded temporal fluctuations of a quasi-CW laser. Single trace (black) is shown together with 50 other traces (gray). The average intensity of 1 000 traces is shown in red.

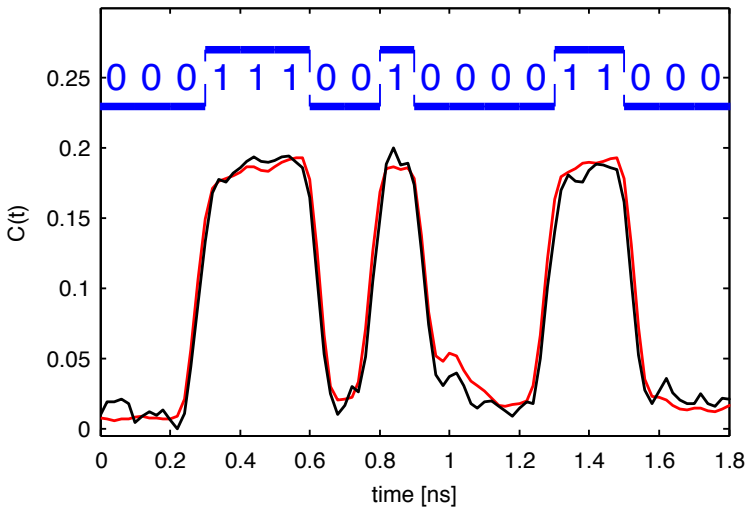

Figure 5.9: Experimental demonstration of TGI made with N=100 000 realizations. The ghost image (black) is compared with the direct measurement of the object (red). The bit pattern driving the optical modulator is schematically shown above the ghost image (blue).

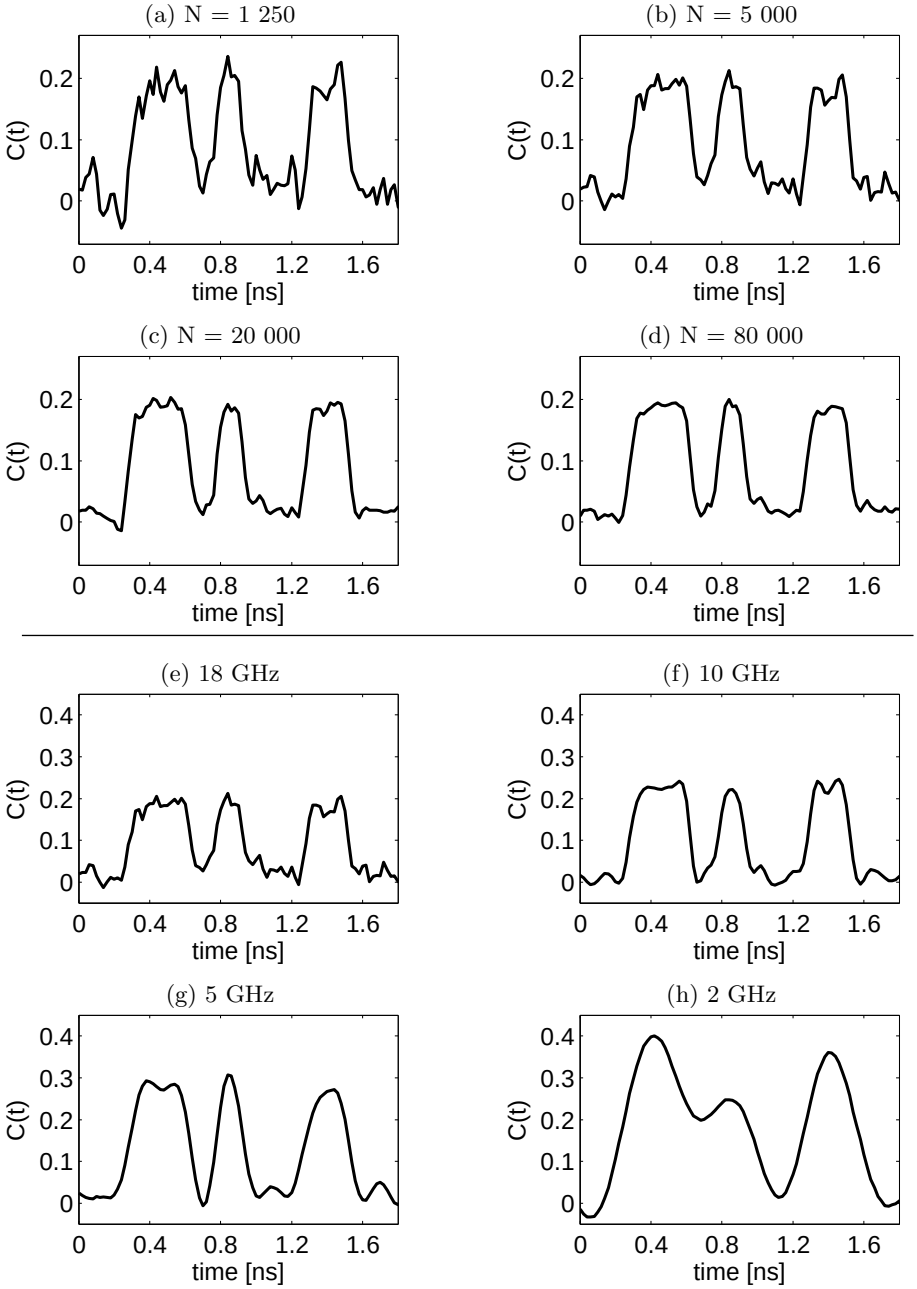

Figure 5.10: Influence of experimental parameters on TGI image quality. (a-d) influence of the number of realizations on the image noise measured with the same detector bandwidth of 18 GHz, (e-h) influence of detector speed on the temporal image resolution and correlation amplitude, measured for $N = 5000$ realizations.

5.4 Magnified Temporal Hhost Imaging

In order to increase the resolution of time-domain ghost imaging, temporal magnification can be used to stretch the temporal intensity fluctuations of the light source. The magnification is only performed in the reference arm, as shown in Fig. 5.11(a), and acts on the light source fluctuations in the ghost plane. Temporal stretching is realized optically, before the signal is convolved with the fast detector response function $T_D(t)$, such that the fast detector effectively measures slower fluctuations. This is equivalent of using a detector with a faster response time $T_{D_M}(t) = T_D(t/M)$ where M is the magnification factor. The resolution is then given by a $T_{SD_M}(t)$:

$$T_{SD_M}(t) = \int_{-\infty}^{+\infty} T_S(t-\tau)T_{D_M}(\tau)d\tau = \int_{-\infty}^{+\infty} T_S(t-\tau)T_D(\tau/M)d\tau. \tag{5.19}$$

It is then clear that to increase the resolution, the fluctuations of the light source should be sufficiently short so that they would not dominate the convolution term $\Delta T_S < \Delta T_D/M$. This can be ensured in practice by using a light source with a sufficiently broad spectral bandwidth. Magnification can be achieved in different ways, using e.g. a time lens[113–115] or a time pinhole[116]. In the case of a time lens, the light is first propagated in a dispersive fiber where it accumulates a total dispersion $\beta^{(2)}z_a$, then experiences a quadratic phase, followed by a second dispersive propagation step $\beta^{(2)}z_b$. This arrangement is the analogue in the time domain of a spatial lens. In a temporal pinhole set-up, light is propagated in a dispersive medium (for a total dispersion $\beta^{(2)}z_a$) after which a narrow temporal transmission gate is applied. A magnified image is obtained after a second dispersive propagation step $\beta^{(2)}z_b$. In both cases the magnification M is defined by the ratio of dispersive propagation lengths before and after the lens/pinhole:

$$M = \frac{\beta^{(2)}z_b}{\beta^{(2)}z_a}. \tag{5.20}$$

The temporal pinhole, although relatively straightforward to implement experimentally, has a drawback imposed by the inherent low overall light transmission. The light intensity captured by the detector is proportional to the pinhole duration and inversely proportional to the desired magnification factor, which results in very low intensities level when large magnification is desired. A time lens on the other hand does not suffer from this drawback, but it is much more difficult to implement experi-

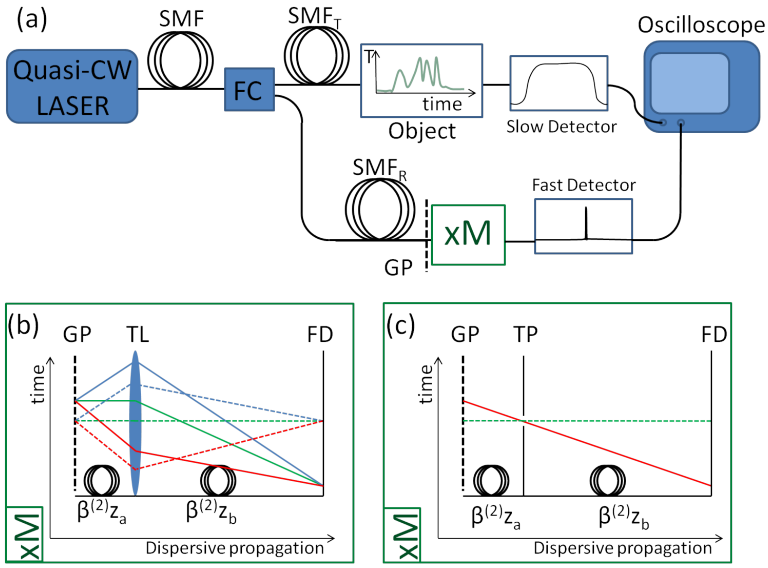

Figure 5.11: (a) Magnification setup (xM) is included into the TGI scheme just after the ghost plane (GP) and before the fast detector (FD). Two magnification schemes: (b) temporal lens (TL) and (c) time pinhole (TP) are presented. Blue, green and red colors denote different frequency components of light originating from two selected time-points of the light irradiating the ghost plane.

mentally. There is another alternative much less complex than a time lens to magnify the intensity fluctuations in the form of a "temporal shadow" imaging set-up shown in Fig. 5.12. This approach which is the analogue of shadow imaging in the spatial domain is discussed and demonstrated in publication P4. It uses a broadband pulsed light source with random fluctuations both within a single pulse and from pulse to pulse. The fluctuations from a given pulse are stretched in time significantly through dispersive propagation in a fiber with total dispersion $\beta^{(2)} z_a$. As a result, the different frequency components are spread in time and irradiate different parts of the temporal object (or ghost plane). In the reference arm, the fluctuations are stretched further in another dispersive fiber with total dispersion $\beta^{(2)} z_b$ and detected with a fast photodetector. The light transmitted through the object in the object arm is recorded by a slow detector as in the conventional time-domain ghost imaging configuration. With this scheme, the intensity fluctuations at the ghost plane are magnified by a factor

$$M = \frac{\beta^{(2)} z_a + \beta^{(2)} z_b}{\beta^{(2)} z_a}. \tag{5.21}$$

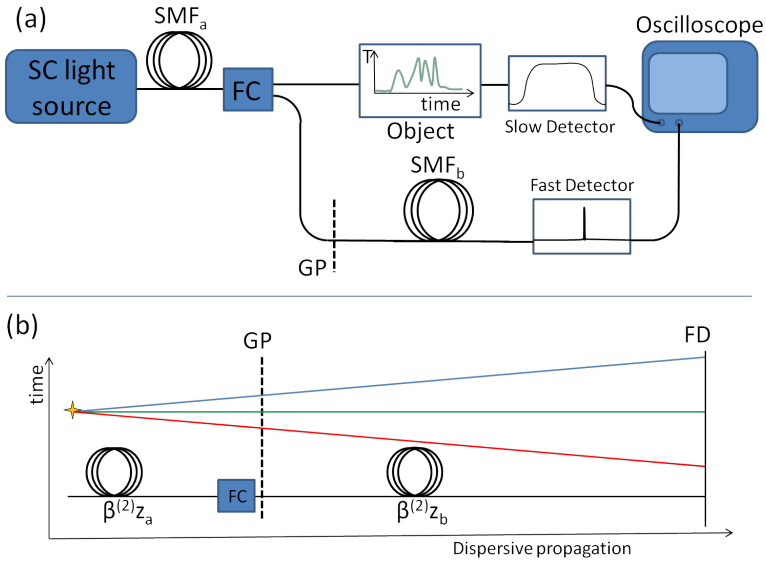

Figure 5.12: (a) TGI set-up with temporal shadow magnification scheme. GP - ghost plane, FC - fiber coupler, SMF- single mode fibers. (b) Schematic view of light propagation in the reference arm of temporal shadow imaging measurements. The light source (marked by the yellow star) is a supercontinuum emitting a broad spectrum, The light passes through the ghost plane and is recorded by the fast detector (FD) . Three particular frequencies of the supercontinuum spectrum are highlighted in blue, green and red.

Because of the finite initial duration of the pulses, the spectral components at the ghost plane are never perfectly separated in time. This causes a particular instant in the ghost plane to be stretched at the detector plane and thus blurs the image. This undesirable effect is similar in the spatial domain to the blur observed in the shadow of an object illuminated by a light source of finite size. Assuming that all the frequency components are distributed uniformly in the initial pulses, the size of the blur τ_b only depends on the initial source pulse duration T_0 and the magnification factor:

$$\tau_b = \frac{z_b}{z_a} T_0 = (M-1)T_0. \tag{5.22}$$

From Eq. (5.22) it can therefore be seen that sources emitting pulses of short durations are preferable in order to limit the blur effect on the reconstructed temporal object.

A pre-requisite for ghost imaging in the time domain is the existence of fast temporal

fluctuations in the light intensity that is transmitted (or reflected) by the object. In the magnified configuration, these fluctuations actually arise from large shot-to-shot spectral fluctuations present in the spectrum of the light source and which are then converted into the time-domain through dispersive propagation. In general, for an incoherent source, the spectral fluctuations period can be approximated by the inverse of the initial pulse duration $1/T_0$ such that the temporal fluctuations τ_s at the ghost plane can be evaluated as:

$$\tau_s \approx \frac{\beta^{(2)} z_a}{T_0}. \tag{5.23}$$

Taking into account the limitations imposed by the detector speed, image blur and intensity fluctuation time, and assuming that these limitations are independent of each other, it is possible to estimate the resolution τ_{res} of the magnified time-domain ghost imaging scheme as:

$$\begin{aligned} \tau_{res} &\approx \sqrt{\left(\frac{\Delta T_D}{M}\right)^2 + \left(\frac{\tau_b}{M}\right)^2 + (\tau_s)^2} \\ &\approx \sqrt{\left(\frac{\Delta T_D}{M}\right)^2 + \left(\frac{M-1}{M}\ T_0\right)^2 + \left(\frac{\beta^{(2)} z_a}{T_0}\right)^2}. \end{aligned} \tag{5.24}$$

If the magnification is equal to 1 (i.e. no magnification) the resolution is mainly limited by the detector response time as discussed in the previous section. But as the magnification increases, the resolution is limited by the initial source pulse duration time T_0. Note that the first dispersive step $\beta^{(2)} z_a$ and the source spectral bandwidth determines the total duration of the intensity fluctuations contained within a single pulse at the ghost plane and one should ensure that it exceeds the duration of the temporal object to be retrieved. The influence of the initial source duration on the resolution is illustrated in Fig. 5.13 for a light source with an 80 nm bandwidth centered at 1550 nm and assuming a 4-ns long temporal object.

Experimental realization of magnified ghost imaging in the time-domain

The experimental realization of magnified TGI is presented in the publication P4. The light source is an incoherent supercontinuum source, similar to the one used in Chapter

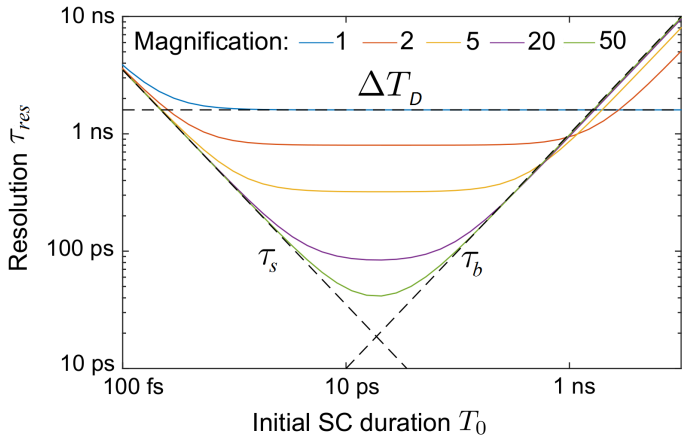

Figure 5.13: Influence of the source pulse duration on magnified TGI resolution presented for different magnification factors. The dashed lines present the resolution limits imposed by the detector resolution without magnification ΔT_D, the shadow blur τ_b for $M \to \infty$, and the source fluctuation time at the ghost plane τ_s. The calculations were performed for an 80-nm bandwidth light source operating at 1550 nm, the initial dispersive propagation step was set in a way that a 4-ns long object would be irradiated.

3. The source has a broad spectrum generated by noise-seeded modulation instability [117]. Due to the incoherent nature of the noise, the spectrum is characterized by random intensity fluctuations which, after dispersive stretching, provide large intensity fluctuations in the time-domain. The spectrum of the source is filtered to match the optical coupler and electro-optic modulator bandwidths, and the intensity is also attenuated to suppress any nonlinear effects that might occur in the dispersive fibers. The first dispersive step $\beta^{(2)} z_a$ is realized in a 2.5 km long SFM-28 fiber after which it is split by a fiber coupler between the object and reference arms. In the reference arm the intensity fluctuations are stretched further along a 10-km long SMF-28 fiber, corresponding to a magnification scheme with magnification factor $M = 5$. The light intensity in the reference arm is measured with a 12.5-GHz bandwidth InGaAs photodiode allowing to image in real time the fast intensity fluctuations of the light source. Examples of recorded intensity fluctuations are shown in Fig. 5.14(a). Light transmitted through the object on the other hand was measured with a 1.2 GHz diode and integrated over a 5 ns time window duration, corresponding to an effective 200 MHz bandwidth bucket detector. The temporal object in this case was composed of several 0.6-ns long pulses generated by an electro-optic modulator driven by the electrical

signal of a programmable ns-pulse generator. A direct measurement of the temporal object was also conducted for comparison purposes. The ghost image retrieved for $N = 100000$ realizations is plotted in 5.14(b). The temporal object is indeed magnified by a factor of 5 as expected, and in excellent agreement with the direct measurement of the object (stretched 5 times numerically to facilitate the comparison).

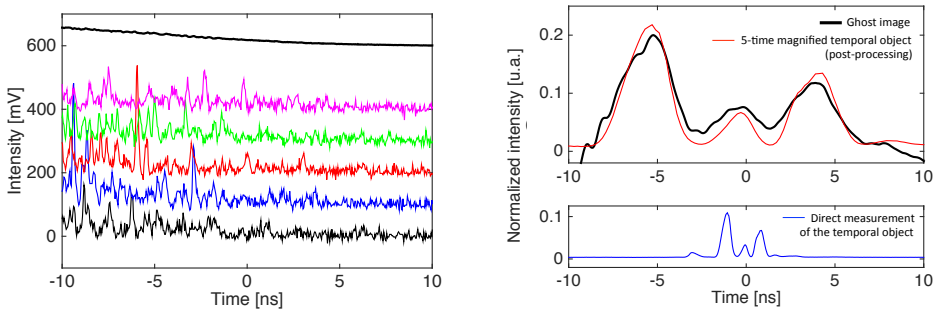

(a) (b)

Figure 5.14: (a) Selected examples of magnified intensity fluctuations measured in the reference arm (note the vertical shift in the intensity axis). The average intensity over 1000 measurements is also shown. (b) Magnified ghost image (black) compared with the 5-times numerically stretched direct measurement of the object (red). For completeness, the direct measurement of the temporal object, without magnification, is shown in blue.

Chapter 6

Summary

Optical imaging techniques are paramount to precisely characterize spatial objects and temporal waveforms. Well-established in laboratories for some of the techniques, commercialized and already used in practical medical procedures for some other, spatial imaging techniques continue to be the subject of intense research and a field of great development. Novel light sources, measurement regimes, and detection schemes continue to improve performance and open new application areas. This work brings novel contributions to the field of imaging both in the time and spatial domains. All the concepts described in this work were validated experimentally, providing potential alternatives to existing techniques.

In the spatial domain, we have proposed a scheme that allows to extend the capabilities for capturing the movement of rapidly oscillating objects. The approach relies on pulsed supercontinuum based stroboscopic white-light interferometry. The tunable repetition rate, broad bandwidth and short pulse duration combined with subharmonic triggering allowed to measure objects oscillating at few-megahertz frequencies - the limit of current mechanical structures. The source was based on off-the-shelf components providing a robust and affordable solution for practical use.

We subsequently demonstrated the concept of Intensity Optical Tomography technique, which, unlike conventional optical coherence tomography approach, is based on intensity correlations. With this technique, we have shown that the influence of even-

order dispersion is inherently cancelled and the point spread function of the system has a reduced width allowing for better image sampling. What's more, the scheme uses classical light sources and off-the-shelf detectors. These results open up new, relatively simple ways for dispersion-free imaging.

We also demonstrated a completely new imaging concept in the time domain in the form of temporal ghost imaging that uses the correlation of the total amount of light transmitted through a time-varying object and the fast intensity fluctuations of light irradiating the object. Experimental measurements were performed with stationary random light in a series of experiments that analysed the performance of the technique. We further demonstrated how to effectively increase the temporal resolution with which temporal variations can be measured through temporal magnification of the signal. These results open novel perspectives for dynamic imaging of ultra-fast waveforms with potential applications in communications and spectroscopy.

In closing, this thesis has been a great journey where novel ideas have been implemented in imaging techniques and experimentally tested. Feedback from the experiments was of invaluable help in understanding the constraints and limits of the proposed scheme often leading to modifications and improved performances. There is no doubt that imaging will keep on playing a central role in the future development of photonics science and everyday life, and we hope that this thesis will have brought its own contribution to the field and stimulate further research based on the results produced here.

References

[1] J. Rogowska, C. M. Bryant, and M. E. Brezinski. Cartilage thickness measurements from optical coherence tomography. J. Opt. Soc. Am. A, **20**, 357 (2003).

[2] I. Kassamakov, K. Hanhijärvi, I. Abbadi, J. Aaltonen, H. Ludvigsen, and E. Hæggström. Scanning white-light interferometry with a supercontinuum source. Opt. Lett., **34**, 1582 (2009).

[3] M. Bellini and T. W. Hänsch. Phase-locked white-light continuum pulses: toward a universal optical frequency-comb synthesizer. Opt. Lett., **25**, 1049 (2000).

[4] Y. Okawachi, K. Saha, J. S. Levy, Y. H. Wen, M. Lipson, and A. L. Gaeta. Octave-spanning frequency comb generation in a silicon nitride chip. Opt. Lett., **36**, 3398 (2011).

[5] H. Park, M. Chodorow, and R. Kompfner. High resolution optical ranging system. Appl. Opt., **20**, 2389 (1981).

[6] C. O'Mahony, M. Hill, M. Brunet, R. Duane, and A. Mathewson. Characterization of micromechanical structures using white-light interferometry. Measurement Science and Technology, **14**, 1807 (2003).

[7] L. Yuan. White-light interferometric fiber-optic strain sensor from three-peak-wavelength broadband LED source. Appl. Opt., **36**, 6246 (1997).

[8] W. B. Ribbens. Interferometric Surface Roughness Measurement. Appl. Opt., **8**, 2173 (1969).

[9] R. C. Youngquist, S. Carr, and D. E. N. Davies. Optical coherence-domain reflectometry: a new optical evaluation technique. Opt. Lett., **12**, 158 (1987).

[10] A. Bosseboeuf and S. Petitgrand. Characterization of the static and dynamic behaviour of M(O)EMS by optical techniques: status and trends. Journal of Micromechanics and Microengineering, **13**, S23 (2003).

[11] D. Huang, E. Swanson, C. Lin, J. Schuman, W. Stinson, W. Chang, M. Hee, T. Flotte, K. Gregory, C. Puliafito, and a. et. Optical coherence tomography. Science, **254**, 1178 (1991).

[12] J. M. Schmitt, A. Knüttel, and R. F. Bonner. Measurement of optical properties of biological tissues by low-coherence reflectometry. Appl. Opt., **32**, 6032 (1993).

[13] J. M. Schmitt and A. Knüttel. Model of optical coherence tomography of heterogeneous tissue. J. Opt. Soc. Am. A, **14**, 1231 (1997).

[14] A. M. Sergeev, V. M. Gelikonov, G. V. Gelikonov, F. I. Feldchtein, R. V. Kuranov, N. D. Gladkova, N. M. Shakhova, L. B. Snopova, A. V. Shakhov, I. A. Kuznetzova, A. N. Denisenko, V. V. Pochinko, Y. P. Chumakov, and O. S. Streltzova. In vivo endoscopic OCT imaging of precancer and cancer states of human mucosa. Opt. Express, **1**, 432 (1997).

[15] N. A. Nassif, B. Cense, B. H. Park, M. C. Pierce, S. H. Yun, B. E. Bouma, G. J. Tearney, T. C. Chen, and J. F. de Boer. In vivo high-resolution video-rate spectral-domain optical coherence tomography of the human retina and optic nerve. Opt. Express, **12**, 367 (2004).

[16] E. Hecht. *Optics* (Addison-Wesley, 2001).

[17] M. Born and E. Wolf, eds. *Principles of Optics (sixth edition)* (Pergamon Press, 1986).

[18] R. W. Boyd. *Nonlinear Optics (third edition)* (Academic Press, 2008).

[19] P. Kaiser and H. W. Astle. Low-Loss Single-Material Fibers Made From Pure Fused Silica. Bell System Technical Journal, **53**, 1021 (1974).

[20] Y. Kodama and A. Hasegawa. Nonlinear pulse propagation in a monomode dielectric guide. IEEE Journal of Quantum Electronics, **23**, 510 (1987).

[21] *Nonlinear Fiber Optics (Fourth Edition)* (Springer, 2007).

[22] R. H. Stolen, J. P. Gordon, W. J. Tomlinson, and H. A. Haus. Raman response function of silica-core fibers. J. Opt. Soc. Am. B, **6**, 1159 (1989).

[23] C.-S. Wang. Theory of Stimulated Raman Scattering. Phys. Rev., **182**, 482 (1969).

[24] A. A. Voronin and A. M. Zheltikov. Soliton self-frequency shift decelerated by self-steepening. Opt. Lett., **33**, 1723 (2008).

[25] N. Akhmediev, W. Królikowski, and A. Lowery. Influence of the Raman-effect on solitons in optical fibers. Optics Communications, **131**, 260 (1996).

[26] F. Luan, D. Skryabin, A. Yulin, and J. Knight. Energy exchange between colliding solitons in photonic crystal fibers. Opt. Express, **14**, 9844 (2006).

[27] L. F. Mollenauer, R. H. Stolen, and J. P. Gordon. Experimental Observation of Picosecond Pulse Narrowing and Solitons in Optical Fibers. Phys. Rev. Lett., **45**, 1095 (1980).

[28] L. F. Mollenauer, W. J. Tomlinson, R. H. Stolen, and J. P. Gordon. Extreme picosecond pulse narrowing by means of soliton effect in single-mode optical fibers. Opt. Lett., **8**, 289 (1983).

[29] F. M. Mitschke and L. F. Mollenauer. Discovery of the soliton self-frequency shift. Opt. Lett., **11**, 659 (1986).

[30] J. P. Gordon. Theory of the soliton self-frequency shift. Opt. Lett., **11**, 662 (1986).

[31] A. Hasegawa. Generation of a train of soliton pulses by induced modulational instability in optical fibers. Opt. Lett., **9**, 288 (1984).

[32] N. N. Akhmediev and V. I. Korneev. Modulation instability and periodic solutions of the nonlinear Schrödinger equation. Theoretical and Mathematical Physics, **69**, 1089 (1986).

[33] A. S. Gouveia-Neto, M. E. Faldon, A. S. B. Sombra, P. G. J. Wigley, and J. R. Taylor. Subpicosecond-pulse generation through cross-phase-modulation-induced modulational instability in optical fibers. Opt. Lett., **13**, 901 (1988).

[34] J. M. Dudley, G. Genty, F. Dias, B. Kibler, and N. Akhmediev. Modulation instability, Akhmediev Breathers and continuous wave supercontinuum generation. Opt. Express, **17**, 21497 (2009).

[35] K. Hammani, B. Wetzel, B. Kibler, J. Fatome, C. Finot, G. Millot, N. Akhmediev, and J. M. Dudley. Spectral dynamics of modulation instability described using Akhmediev breather theory. Opt. Lett., **36**, 2140 (2011).

[36] L. Mandel and E. Wolf, eds. *Optical Coherence and Quantum Optics* (Cambridge University Press, 1995).

[37] D. N. Wang, Y. N. Ning, K. T. V. Grattan, A. W. Palmer, and K. Weir. Three-wavelength combination source for white-light interferometry. IEEE Photonics Technology Letters, **5**, 1350 (1993).

[38] M. Fleischer, R. Windecker, and H. J. Tiziani. Theoretical limits of scanning white-light interferometry signal evaluation algorithms. Appl. Opt., **40**, 2815 (2001).

[39] V. Heikkinen, I. Kassamakov, T. Paulin, A. Nolvi, and E. Hæggström. Stroboscopic scanning white light interferometry at 2.7 MHz with 1.6 μm coherence length using a non-phosphor LED source. Opt. Express, **21**, 5247 (2013).

[40] I. Shavrin, L. Lipiäinen, K. Kokkonen, S. Novotny, M. Kaivola, and H. Ludvigsen. Stroboscopic white-light interferometry of vibrating microstructures. Opt. Express, **21**, 16901 (2013).

[41] P. Ryczkowski, A. Nolvi, I. Kassamakov, G. Genty, and E. Hæggström. High-speed stroboscopic imaging with frequency-doubled supercontinuum. Optics Letters, **38**, 658 (2013).

[42] J. M. Dudley, G. Genty, and S. Coen. Supercontinuum generation in photonic crystal fiber. Rev. Mod. Phys., **78**, 1135 (2006).

[43] G. Genty, S. Coen, and J. M. Dudley. Fiber supercontinuum sources (Invited). J. Opt. Soc. Am. B, **24**, 1771 (2007).

[44] J. M. Dudley and S. Coen. Coherence properties of supercontinuum spectra generated in photonic crystal and tapered optical fibers. Opt. Lett., **27**, 1180 (2002).

[45] E. M. Dianov, P. V. Mamyshev, A. M. Prokhorov, and S. V. Chernikov. Generation of a train of fundamental solitons at a high repetition rate in optical fibers. Opt. Lett., **14**, 1008 (1989).

[46] P. V. Mamyshev, S. V. Chernikov, E. M. Dianov, and A. M. Prokhorov. Generation of a high-repetition-rate train of practically noninteracting solitons by using the induced modulational instability and Raman self-scattering effects. Opt. Lett., **15**, 1365 (1990).

[47] K. Washio, K. Inoue, and S. Kishida. Efficient large-frequency-shifted three-wave mixing in low dispersion wavelength region in single-mode optical fibre. Electronics Letters, **16**, 658 (1980).

[48] S. Trillo and S. Wabnitz. Dynamics of the nonlinear modulational instability in optical fibers. Opt. Lett., **16**, 986 (1991).

[49] P. K. A. Wai, C. R. Menyuk, Y. C. Lee, and H. H. Chen. Nonlinear pulse propagation in the neighborhood of the zero-dispersion wavelength of monomode optical fibers. Opt. Lett., **11**, 464 (1986).

[50] K. Mori, H. Takara, and S. Kawanishi. Analysis and design of supercontinuum pulse generation in a single-mode optical fiber. J. Opt. Soc. Am. B, **18**, 1780 (2001).

[51] J. M. Dudley and J. R. Taylor, eds. *Supercontinuum Generation in Optical Fibers* (Cambridge University Press, 2010).

[52] A. Demircan and U. Bandelow. Supercontinuum generation by the modulation instability. Optics Communications, **244**, 181 (2005).

[53] N. Korneev, E. A. Kuzin, B. Ibarra-Escamilla, M. Bello-Jiménez, and A. Flores-Rosas. Initial development of supercontinuum in fibers with anomalous dispersion pumped by nanosecond - long pulses. Opt. Express, **16**, 2636 (2008).

[54] A. Demircan and U. Bandelow. Analysis of the interplay between soliton fission and modulation instability in supercontinuum generation. Applied Physics B, **86**, 31 (2007).

[55] K. Tai, N. Bekki, and A. Hasegawa. Fission of optical solitons induced by stimulated Raman effect. Opt. Lett., **13**, 392 (1988).

[56] M. N. Islam, G. Sucha, I. Bar-Joseph, M. Wegener, J. P. Gordon, and D. S. Chemla. Broad bandwidths from frequency-shifting solitons in fibers. Opt. Lett., **14**, 370 (1989).

[57] S. Coen, A. H. L. Chau, R. Leonhardt, J. D. Harvey, J. C. Knight, W. J. Wadsworth, and P. S. J. Russell. Supercontinuum generation by stimulated Raman scattering and parametric four-wave mixing in photonic crystal fibers. J. Opt. Soc. Am. B, **19**, 753 (2002).

[58] A. Mussot, E. Lantz, H. Maillotte, T. Sylvestre, C. Finot, and S. Pitois. Spectral broadening of a partially coherent CW laser beam in single-mode optical fibers. Opt. Express, **12**, 2838 (2004).

[59] P. A. Franken, A. E. Hill, C. W. Peters, and G. Weinreich. Generation of Optical Harmonics. Phys. Rev. Lett., **7**, 118 (1961).

[60] K. Regelskis, J. Želudevičius, N. Gavrilin, and G. Račiukaitis. Efficient second-harmonic generation of a broadband radiation by control of the temperature distribution along a nonlinear crystal. Opt. Express, **20**, 28544 (2012).

[61] S. K. Debnath and M. P. Kothiyal. Improved optical profiling using the spectral phase

in spectrally resolved white-light interferometry. Appl. Opt., **45**, 6965 (2006).

[62] Q. Wang, Y. Ning, A. Palmer, and K. Grattan. Central fringe identification in a white light interferometer using a multi-stage-squaring signal processing scheme. Optics Communications, **117**, 241 (1995).

[63] P. de Groot, X. C. de Lega, J. Kramer, and M. Turzhitsky. Determination of fringe order in white-light interference microscopy. Appl. Opt., **41**, 4571 (2002).

[64] K. G. Larkin, D. J. Bone, and M. A. Oldfield. Natural demodulation of two-dimensional fringe patterns. I. General background of the spiral phase quadrature transform. J. Opt. Soc. Am. A, **18**, 1862 (2001).

[65] J. H. Kim. High Precision Signal Processing Algorithm for White Light Interferometry. Sensors, **8**, 7609 (2008).

[66] A. F. Fercher, W. Drexler, C. K. Hitzenberger, and T. Lasser. Optical coherence tomography - principles and applications. Reports on Progress in Physics, **66**, 239 (2003).

[67] B. Bouma. *Handbook of Optical Coherence Tomography* (Taylor & Francis, 2001).

[68] W. Drexler and J. G. Fujimoto, eds. *Optical Coherence Tomography Technology and Applications* (Springer, 2008).

[69] W. Drexler, U. Morgner, F. X. Kärtner, C. Pitris, S. A. Boppart, X. D. Li, E. P. Ippen, and J. G. Fujimoto. In vivo ultrahigh-resolution optical coherence tomography. Opt. Lett., **24**, 1221 (1999).

[70] A. G. Podoleanu, G. M. Dobre, and D. A. Jackson. En-face coherence imaging using galvanometer scanner modulation. Opt. Lett., **23**, 147 (1998).

[71] G. Liu, A. J. Lin, B. J. Tromberg, and Z. Chen. A comparison of Doppler optical coherence tomography methods. Biomed. Opt. Express, **3**, 2669 (2012).

[72] J. A. Izatt, M. D. Kulkarni, S. Yazdanfar, J. K. Barton, and A. J. Welch. In vivo bidirectional color Doppler flow imaging of picoliter blood volumes using optical coherence tomography. Opt. Lett., **22**, 1439 (1997).

[73] Z. Chen, T. E. Milner, D. Dave, and J. S. Nelson. Optical Doppler tomographic imaging of fluid flow velocity in highly scattering media. Opt. Lett., **22**, 64 (1997).

[74] M. D. Kulkarni, T. G. van Leeuwen, S. Yazdanfar, and J. A. Izatt. Velocity-estimation accuracy and frame-rate limitations in color Doppler optical coherence tomography. Opt. Lett., **23**, 1057 (1998).

[75] R. Leitgeb, C. K. Hitzenberger, and A. F. Fercher. Performance of fourier domain vs. time domain optical coherence tomography. Opt. Express, **11**, 889 (2003).

[76] J. F. de Boer, B. Cense, B. H. Park, M. C. Pierce, G. J. Tearney, and B. E. Bouma. Improved signal-to-noise ratio in spectral-domain compared with time-domain optical coherence tomography. Optics Letters, **28**, 2067 (2003).

[77] A. F. Fercher, C. K. Hitzenberger, M. Sticker, R. Zawadzki, B. Karamata, and

T. Lasser. Numerical dispersion compensation for Partial Coherence Interferometry and Optical Coherence Tomography. Opt. Express, **9**, 610 (2001).

[78] T. Shirai and A. T. Friberg. Resolution improvement in spectral-domain optical coherence tomography based on classical intensity correlations. Optics Letters, **38**, 115 (2013).

[79] T. Shirai and A. T. Friberg. Intensity-interferometric spectral-domain optical coherence tomography with dispersion cancellation. J. Opt. Soc. Am. A, **31**, 258 (2014).

[80] V. Torres-Company, H. Lajunen, and A. T. Friberg. 'Nonlocal' dispersion cancelation with classical light. New Journal of Physics, **11**, 063041 (2009).

[81] A. F. Abouraddy, B. E. A. Saleh, A. V. Sergienko, and M. C. Teich. Role of Entanglement in Two-Photon Imaging. Phys. Rev. Lett., **87**, 123602 (2001).

[82] A. F. Abouraddy, B. E. A. Saleh, A. V. Sergienko, and M. C. Teich. Entangled-photon Fourier optics. J. Opt. Soc. Am. B, **19**, 1174 (2002).

[83] G. Scarcelli, V. Berardi, and Y. Shih. Can Two-Photon Correlation of Chaotic Light Be Considered as Correlation of Intensity Fluctuations? Phys. Rev. Lett., **96**, 063602 (2006).

[84] J. D. Franson. Lack of dispersion cancellation with classical phase-sensitive light. Phys. Rev. A, **81**, 023825 (2010).

[85] A. F. Abouraddy, M. B. Nasr, B. E. A. Saleh, A. V. Sergienko, and M. C. Teich. Quantum-optical coherence tomography with dispersion cancellation. Phys. Rev. A, **65**, 053817 (2010).

[86] M. B. Nasr, B. E. A. Saleh, A. V. Sergienko, and M. C. Teich. Demonstration of Dispersion-Canceled Quantum-Optical Coherence Tomography. Phys. Rev. Letters, **91**, 083601 (2003).

[87] R. Kaltenbaek, J. Lavoie, and K. J. Resch. Classical Analogues of Two-Photon Quantum Interference. Phys. Rev. Lett., **102**, 243601 (2009).

[88] J. Lavoie, R. Kaltenbaek, and K. J. Resch. Quantum-optical coherence tomography with classical light. Opt. Express, **17**, 3818 (2009).

[89] M. B. Nasr, B. E. A. Saleh, A. V. Sergienko, and M. C. Teich. Dispersion-cancelled and dispersion-sensitive quantum optical coherence tomography. Opt. Express, **12**, 1351 (2004).

[90] B. E. A. Saleh, A. F. Abouraddy, A. V. Sergienko, and M. C. Teich. Duality between partial coherence and partial entanglement. Phys. Rev. A, **62**, 043816 (2000).

[91] P. Ryczkowski, J. Turunen, A. T. Friberg, and G. Genty. Experimental Demonstration of Spectral Intensity Optical Coherence Tomography. Scientific Reports, **6**, 22126 (2016).

[92] F. Robles, R. N. Graf, and A. Wax. Dual window method for processing spectroscopic optical coherence tomography signals with simultaneously high spectral and temporal resolution. Opt. Express, **17**, 6799 (2009).

[93] R. S. Bennink, S. J. Bentley, and R. W. Boyd. "Two-Photon" Coincidence Imaging with a Classical Source. Phys. Rev. Lett., **89**, 113601 (2002).

[94] R. S. Bennink, S. J. Bentley, R. W. Boyd, and J. C. Howell. Quantum and Classical Coincidence Imaging. Phys. Rev. Lett., **92**, 033601 (2004).

[95] B. Sun, M. P. Edgar, R. Bowman, L. E. Vittert, S. Welsh, A. Bowman, and M. J. Padgett. 3D Computational Imaging with Single-Pixel Detectors. Science, **340**, 844 (2013).

[96] T. B. Pittman, Y. H. Shih, D. V. Strekalov, and A. V. Sergienko. Optical imaging by means of two-photon quantum entanglement. Phys. Rev. A, **52**, R3429 (1995).

[97] C. Zhang, S. Guo, J. Cao, J. Guan, and F. Gao. Object reconstitution using pseudo-inverse for ghost imaging. Opt. Express, **22**, 30063 (2014).

[98] J. H. Shapiro. Computational ghost imaging. Phys. Rev. A, **78**, 061802 (2008).

[99] Y. Zhu, J. Shi, H. Li, and G. Zeng. Three-dimensional ghost imaging based on periodic diffraction correlation imaging. Chin. Opt. Lett., **12**, 071101 (2014).

[100] B. I. Erkmen. Computational ghost imaging for remote sensing applications. Interplanetary Network Progress Reports, **42**, 1 (2011).

[101] B. I. Erkmen. Computational ghost imaging for remote sensing. J. Opt. Soc. Am. A, **29**, 782 (2012).

[102] B. I. Erkmen and J. H. Shapiro. Ghost imaging: from quantum to classical to computational. Advances in Optics and Photonics, **2**, 405 (2010).

[103] R. Meyers, K. S. Deacon, and Y. Shih. Ghost-imaging experiment by measuring reflected photons. Phys. Rev. A, **77**, 041801 (2008).

[104] R. E. Meyers, K. S. Deacon, and Y. Shih. Turbulence-free ghost imaging. Applied Physics Letters, **98**, 111115 (2011).

[105] Y. Cai and S.-Y. Zhu. Ghost imaging with incoherent and partially coherent light radiation. Phys. Rev. E, **71**, 056607 (2005).

[106] R. Salem, M. A. Foster, and A. L. Gaeta. Application of space-time duality to ultrahigh-speed optical signal processing. Adv. Opt. Photon., **5**, 274 (2013).

[107] B. H. Kolner. Space-time duality and the theory of temporal imaging. IEEE Journal of Quantum Electronics, **30**, 1951 (1994).

[108] T. Shirai, T. Setälä, and A. T. Friberg. Ghost imaging of phase objects with classical incoherent light. Phys. Rev. A, **84**, 041801 (2011).

[109] Z. Chen, H. Li, Y. Li, J. Shi, and G. Zeng. Temporal ghost imaging with a chaotic laser. Optical Engineering, **52**, 076103 (2013).

[110] T. Shirai, T. Setälä, and A. T. Friberg. Temporal ghost imaging with classical non-stationary pulsed light. J. Opt. Soc. Am. B, **27**, 2549 (2010).

[111] B. K. Ghosh. Asymptotic Expansions for the Moments of the Distribution of Correlation

Coefficient. Biometrika, **53**, 258 (1966).

[112] P. Ryczkowski, M. Barbier, A. T. Friberg, J. M. Dudley, and G. Genty. Ghost imaging in the time domain. Nat. Photon., **10**, 167 (2016).

[113] B. H. Kolner and M. Nazarathy. Temporal imaging with a time lens. Opt. Lett., **14**, 630 (1989).

[114] R. Salem, M. A. Foster, A. C. Turner, D. F. Geraghty, M. Lipson, and A. L. Gaeta. Optical time lens based on four-wave mixing on a silicon chip. Opt. Lett., **33**, 1047 (2008).

[115] M. Fridman, A. Farsi, Y. Okawachi, and A. L. Gaeta. Demonstration of temporal cloaking. Nature, **481**, 62 (2012).

[116] Z. Wu, J. Dong, J. Hou, S. Yan, Y. Yu, and X. Zhang. Temporal imaging using a time pinhole. Opt. Express, **22**, 8076 (2014).

[117] S. D. R., H. G., J. B., and R. C. Fluctuations and correlations in modulation instability. Nat Photon, **6**, 463 (2012).

Appendices

Paper I

Piotr Ryczkowski, Anton Nolvi, Ivan Kassamakov,
Goëry Genty, and Edward Hæggström.

High-speed stroboscopic imaging with frequency-doubled supercontinuum

OPTICS LETTERS / Vol. 38, No. 5 / March 1, 2013.

doi: 10.1364/OL.38.000658.

©2013 Optical Society of America

High-speed stroboscopic imaging with frequency-doubled supercontinuum

Piotr Ryczkowski,[1,*] Anton Nolvi,[2] Ivan Kassamakov,[2] Goëry Genty,[1] and Edward Hæggström[2]

[1]*Department of Physics, Tampere University of Technology, Tampere FIN-33101, Finland*

[2]*Department of Physics, University of Helsinki, Helsinki FIN-00014, Finland*

**Corresponding author: piotr.ryczkowski@tut.fi*

Received December 19, 2012; accepted January 1, 2013;
posted January 16, 2013 (Doc. ID 182056); published February 22, 2013

We present a supercontinuum (SC) light source designed for stroboscopic white light interferometry. The compact, cost-effective SC source is built from off-the-shelf optical components and operates both in the visible and near-IR at arbitrary repetition rates in the 10 kHz–1 MHz frequency range. We estimate that our source allows performing dynamic white-light interferometric characterization of rapidly oscillating objects up to several tens of megahertz. Its current potential is demonstrated by capturing the movement of a microelectromechanical system oscillating at 2.16 MHz with sub-100 nm accuracy. © 2013 Optical Society of America

OCIS codes: 120.3180, 320.6629.

Scanning white light interferometry (SWLI) is a high-resolution, noncontact imaging technique that can be used to characterize objects ranging from biological tissues to novel materials and components [1–3]. Compared to standard two-dimensional microscopy methods, SWLI allows reconstructing three-dimensional (3D) images from the interference pattern recorded between a reference arm and another arm in which the object being tested is placed. SWLI is not restricted to measuring static samples; rapidly oscillating objects also can be characterized with modulated light sources that illuminate the sample motion. In this case a camera captures interferograms—the combination of light from the reference and object arms—at select phases of the motion, which permits stroboscopic imaging of the "frozen sample".

To obtain high-resolution SWLI images, the bandwidth of the source should be broad. Light bulbs, halogen lamps, white LEDs, and supercontinuum (SC) [4,5] sources are typically used in white light interferometry. All these sources possess a broad bandwidth and short coherence length. Yet, halogen lamps and LEDs typically suffer from low output power that is further decreased by the small duty cycle necessary in the measurement, and they can only be modulated with restrictions. In practice, it is hard to produce pulses shorter than 10 ns duration, which limits the maximum oscillation frequency that can be imaged. Since SC sources are bright and broadband, they are ideal candidates for a SWLI source. The downside with SC sources is that they usually require coupling expensive pump lasers into highly nonlinear photonic crystal fibers (PCFs), which can make their long-term operation unstable in the case of free-space coupling or make them sensitive to power damage when tapered fiber adaptors are spliced between the pump laser and the PCF. Most importantly, for mode-locked or *Q*-switched pump lasers, SC pulses are produced at a fixed repetition rate (or harmonic of it). On the other hand, amplified pump diodes offer cost-effective solutions with more flexibility in the repetition rate but at the expense of the pulse duration [6].

Microelectromechanical systems (MEMS) are cost-effective sensors and actuators that are increasingly used in cars, display technology, inkjet printing, and biomedicine. Consequently, it is important to develop accurate characterization techniques for these devices. Common methods for MEMS characterization are atomic force microscopy (AFM) and scanning electron microscopy. Although AFM may reach nanometer precision, it requires physical contact with the MEMS device and is slow. In contrast, SWLI can acquire full 3D images in a few seconds.

SWLI using SC sources can record 3D images of static objects with 30 nm accuracy [5] or of MEMS structures oscillating at a few hertz [7]. Here, we extend the potential of SC sources for rapid dynamic SWLI 3D imaging by demonstrating a cost-effective, broadband SC source with a small footprint, operating both in the visible and near-IR spectral regions. This source provides a continuously tunable repetition rate up to 1 MHz for stroboscopic white light interferometry. The SC source is based on off-the-shelf optical components and we prove that it allows capturing the 3D profile of a MEMS oscillating at 2.16 MHz with sub-100 nm precision. Importantly, the oscillating frequency of the movement that can be imaged is not restricted by the source but rather by the MEMS performance. Our test result is close to the 2.4 MHz maximum imaging frequency provided by the Bruker device [8], which solidifies the position of SWLI as a powerful technology for dynamic 3D imaging.

A schematic of the SC source is shown in Fig. 1(a). The source consists of a gain-switched fiber laser operating at 1547 nm (Keopsys KPS-KULT2-1550) producing 1 ns pulses with a peak power of 10 kW. The repetition rate of the pump laser can be tuned arbitrarily from 10 kHz to 1 MHz. The laser output is connected to a 6 m dispersion-shifted fiber (Corning LEAF, G.655) with 1510 nm zero-dispersion wavelength. The fiber length was optimized using numerical simulations [9] to generate an SC from 1200 to 2000 nm. The experimental SC spectrum measured at the output of the fiber is shown in Fig. 1(c), where it can be seen that the bandwidth covers the wavelength range predicted by the simulations. To extend the operating wavelength range of the SC source into the visible region, we exploited the relative insensitivity to the incident angle of the phase-matching curve of beta

0146-9592/13/050658-03$15.00/0 © 2013 Optical Society of America

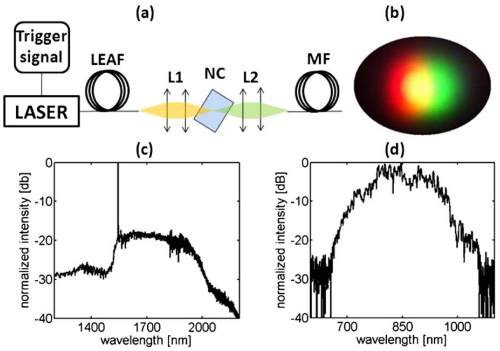

Fig. 1. (Color online) (a) SC source setup. L1, L2: achromatic lens sets, NC: nonlinear crystal, MF: multimode fiber. (b) Photograph showing the spatial dependence of the visible SC spectrum across the beam (the crystal was oriented to highlight this dependence). Normalized SC spectrum before (c) and after (d) the crystal.

barium borate (BBO) crystals to frequency-double the near-IR SC. Besides increasing the operating wavelength range, the advantage of frequency-doubling is twofold: (i) it allows operating within the silicon absorption band, the core material of MEMS, and (ii) it allows altering the SC spectral shape by fine tuning the angle of the BBO crystal to favor or reduce the conversion efficiency at specific wavelengths.

Frequency-doubling was realized by focusing with a 3 cm focal achromatic lens the SC onto an 8 mm thick periodically poled BBO crystal. We strongly focused the beam to fulfill the phase-matching condition for nearly all the SC wavelengths. In this way, most of the SC spectrum can be frequency-doubled simultaneously. In addition, by carefully adjusting the BBO crystal angle with respect to the output of the fiber, it is possible to compensate for the asymmetric spectral shape of the near-IR SC spectrum that results from the detuning between the fiber zero-dispersion and the pump wavelength.

We also take advantage of the crystal orientation to induce a phase-mismatch in the spectral component at 1547 nm, which removes the strong pump peak residue apparent in the near-IR SC. The final result is a SC spectrum spanning from 680 nm to beyond 1000 nm with a quasi-Gaussian spectral envelope. The repetition rate of the SC can be simply tuned by changing the frequency of the pump laser driving signal. The overall efficiency of the frequency-doubling process was estimated to be less than 1%, corresponding to a total power of 0.5 mW.

Even though the conversion efficiency is low because of the short interaction length in the crystal and the fact that the phase-matching condition for each spectral component is not fulfilled across the whole beam area due to the strong focusing configuration, the average power of the SC source in the 680–1000 nm wavelength range is sufficient for our dynamic imaging experiment. Because the SC dynamics are initially seeded by noise, the near-IR SC is quasi-incoherent with large shot-to-shot fluctuations. Similar fluctuations also are observed after the BBO crystal. One drawback of the experimental arrangement is that the SC spectrum after the BBO crystal is nonuniform across the beam since different wavelengths are phase-matched for different angles in the crystal [Fig. 1(b)]. This spatial dependence is detrimental because it can cause artifacts in the white light interferograms. It was suppressed by coupling the beam into a multimode fiber that directs the light to the interferometer.

The SC source was used to perform stroboscopic 3D imaging of a rapidly oscillating MEMS device. The SWLI set up (see Fig. 2) consists of a microscope objective (Nikon CF Plan DI Mirau 10×) and a monochrome progressive scan CCD-camera (Pulnix TM-6740GE). The interferometric objective is placed on a piezoelectric translator (PI P-725.1CD) that allows scanning in the direction perpendicular to the sample with a shortest step size of 100 nm (mean wavelength of the interferogram is 830 nm divided by eight). At each step, the light intensity corresponding to the different object areas is detected by each camera pixel. The information is stored and analyzed by a computer. These data are corrected for camera frame rate and piezo position, and then processed to extract the image profile of the object. The extraction is done by a five-point Larkin algorithm [5,7].

The MEMS device consists of several capacitive micromachined ultrasonic transducer array (CMUT) elements [10]. Each element comprises several active cells and each cell features a several hundred nm thick, partly metallized silicon membrane supported by silicon-oxide posts. The membranes are some tens of microns in diameter. A DC bias deflects the membrane. Driven by AC excitation, the membrane oscillates into a vacuum-filled cavity that is few hundreds of nanometre deep. The oscillation of the membrane is driven by a sine-wave function generator (Tektronix AFG-3252) whilst the second channel of the generator triggers the pulses of the SC pump laser. The resonance frequency of the CMUT is 2.16 MHz and this particular drive frequency was used. To perform dynamic measurement of the oscillating MEMS, we used the 32nd harmonic of the waveform generator to set the pump laser repetition rate. Both frequencies were set manually with a ratio of 32 between them, which means that the SC pulses illuminated the MEMS with 67.5 kHz repetition rate. The pump laser peak power depends on the repletion rate and triggering the pump laser from the 32nd harmonic of the MEMS driving frequency allows to operate in a regime of sufficient power to generate a broad SC as seen in Fig. 1. The relative

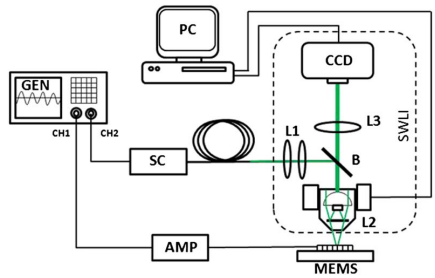

Fig. 2. (Color online) SWLI setup. B, beam splitter; L1, collimating lenses; L2, Mirau interferometer objective; L3, camera objective; GEN, signal generator; AMP, driving signal amplifier.

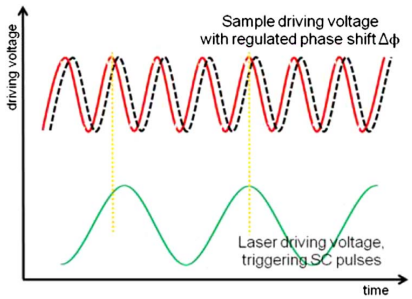

Fig. 3. (Color online) Illustration of the relation between the CMUT and pump laser driving signals.

phase $\Delta\phi$ between the harmonic signal and the fundamental waveform could be fine-tuned and the image at different phases of the MEMS oscillation cycle could then be acquired by varying the phase difference (see Fig. 3).

To image a full oscillation cycle of the CMUT, sequences of measurements were taken with a phase difference of $\pi/8$. Figure 4 shows the reconstructed 3D moving profile of the CMUT along with a profile of the cross section measured at selected oscillation phases. In principle, the z-axis resolution in the image is determined by the accuracy with which the peak of the interferogram envelope can be detected (i.e., the resolution of the piezo-stage) [10]. However, in practice, the precision is limited by environmental conditions (e.g., mechanical vibrations, precision in phase shifting, light source stability), and duty cycle length in stroboscopy [11]. With our experimental setup, we estimate the resolution to be less than 100 nm, as seen from the profile cross section shown in Fig. 4(c).

Note that it is crucial to be able to operate the SC source at an arbitrary repetition rate. The limitation in terms of oscillation frequency arises from the SC pulse duration (here 1 ns), which must be much shorter than the period of the oscillating MEMS. The pump laser jitter is approximately 1 ns, which does not affect the stroboscopic measurements averaged over multiple oscillation cycles. Yet, for high oscillation frequency in excess of several tens of megahertz, the jitter would be a clear limitation in addition to the pulse duration. We estimate that the SC source developed in this work should permit performing stroboscopic imaging of structures oscillating at frequencies as high as several tens of megahertz.

In conclusion, we demonstrated stroboscopic white light interferometry using a specially designed SC source that can operate at an arbitrary selected repetition rate

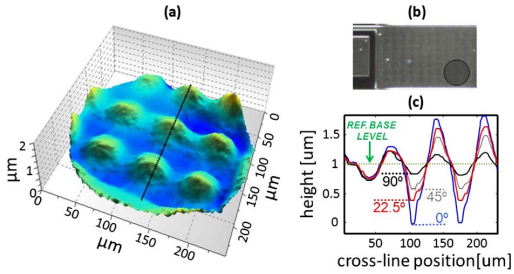

Fig. 4. (Color online) (a) Reconstructed 3D image for a specific phase of the MEMS oscillation, (b) microscope image of the MEMS, and (c) profile cross section obtained at selected oscillation phases and measured along the direction of the dotted line indicated in (a).

from 10 kHz to 1 MHz. As a proof of concept, we captured the 3D image of a MEMS oscillating at 2.16 MHz with sub-100 nm resolution. We anticipate that our experimental setup may be able to image objects performing identical oscillating cycles at high frequencies, potentially up to several tens of megahertz, far beyond the capability of current light sources employed for SWLI. Finally, we point out that the system presented here also can operate in near-IR if the nonlinear crystal is removed, which could allow penetrating into silicon samples transparent in this wavelength range.

References

1. C. O'Mahony, M. Hill, M. Brunet, R. Duane, and A. Mathewson, Meas. Sci. Technol. **14**, 1807 (2003).
2. J. Lademann, A. Knüttel, H. Richter, N. Otberg, R. V. Pelchrzim, H. Audring, H. Meffert, W. Sterry, and K. Hoffmann, Laser Phys. **15**, 288 (2005).
3. J. Rogowska, C. M. Bryant, and M. E. Brezinski, J. Opt. Soc. Am. A **20**, 357 (2003).
4. D. N. Wang, Y. N. Ning, K. T. V. Grattan, A. W. Palmer, and K. Weir, IEEE Photon. Technol. Lett. **5**, 1350 (1993).
5. I. Kassamakov, Hanhijärvi, I. Abbadi, J. Aaltonen, H. Ludvigsen, and E. Hæggström, Opt. Lett. **34**, 1582 (2009).
6. S. Moon and D. Kim, Opt. Express **14**, 270 (2006).
7. K. Hanhijärvi, I. Kassamakov, V. Heikkinen, J. Aaltonen, L. Sainiemi, K. Grigoras, S. Franssila, and E. Hæggström, Opt. Lett. **37**, 1703 (2012).
8. A. L. Hartzell, M. G. da Silva, and H. R. Shea, *MEMS Reliability* (Springer, 2010).
9. G. Genty, P. Kinsler, B. Kibler, and J. M. Dudley, Opt. Express **15**, 5382 (2007).
10. B. Bhushan, J. C. Wyant, and J. Meiling, Wear **122**, 301 (1988).
11. M. Fleischer, R. Windecker, and H. Tiziani, Appl. Opt. **40**, 2815 (2001).

Paper II

Piotr Ryczkowski, JariTurunen, Ari T. Friberg, and Goëry Genty.

Experimental Demonstration of Spectral Intensity Optical Coherence Tomography

Scientific Reports / Vol. 6, 22126 / February 26, 2016.

doi: 10.1038/srep22126.

©2016 Macmillan Publishers Limited

SCIENTIFIC REPORTS

OPEN

Experimental Demonstration of Spectral Intensity Optical Coherence Tomography

Received: 13 October 2015
Accepted: 03 February 2016
Published: 26 February 2016

Piotr Ryczkowski[1], Jari Turunen[2], Ari T. Friberg[2] & Goëry Genty[1]

We demonstrate experimentally spectral-domain intensity optical coherence tomography using a Mach-Zehnder interferometer with balanced detection. We show that the technique allows for a point spread function with reduced full-width at half maximum compared to conventional optical coherence tomography. The method further provides benefits similar to those of chirped-pulse interferometry in terms of dispersion cancellation but only requires a broadband incoherent source and standard detectors. The measurements are in excellent agreement with the theoretical predictions. Finally, we propose an approach that enables the elimination of potential artefacts arising from multiple interfaces.

Optical coherence tomography (OCT) is a powerful, three-dimensional (3D) imaging technique which may be operated in both the spectral and the temporal domain[1,2], and it is widely employed for biological *in vitro* and *in vivo* imaging[3]. The axial resolution of conventional OCT is limited by the spectral bandwidth of the light source and by the dispersion of the optical components and/or the sample under the test. Because of dispersion, especially in fiber-based setups, increasing the spectral bandwidth of the light source may not necessarily lead to resolution improvement[4]. To circumvent this problem several approaches have been proposed, including both numerical[5,6] and experimental techniques[7–13]. In particular, methods such as quantum-optical coherence tomography (QOCT) or chirped pulse interferometry have been shown to possess built-in dispersion cancelation and resolution enhancement; however, these techniques generally require sophisticated light sources such as single-photon sources or chirped ultrashort pulses and advanced detection techniques[9–13]. They also operate in the time domain requiring in-depth scanning, which results in slow measurement times.

Intensity-based optical coherence tomography, based on higher-order correlations compared to standard OCT, using a classical broadband light source and a Mach-Zehnder interferometer with balanced detection was recently put forward in the time domain[14,15]. The method produces improved resolution but is hampered by the lack of ultrafast detectors capable of recording rapid intensity variations characteristic of incoherent sources. Spectral intensity optical coherence tomography (SIOCT) on the other hand provides a much simpler and cost-effective alternative that operates, without moving parts, in the spectral domain and can use a classical broadband light source of any state of temporal coherence and standard detectors[16,17]. Furthermore, SIOCT requires only a minor modification of conventional spectral-domain OCT imaging setup, exhibits a point spread function (PSF) with reduced full-width at half maximum compared to standard OCT, and, significantly, possesses built-in even-order dispersion cancellation. Yet, no experimental demonstration of SIOCT has been reported. Numerical techniques based on higher-order correlations that yields the frequency-depth distribution[18] have been suggested and demonstrated[19] to provide useful information when the spectrum of backscattered light are depth-varying along the imaging axis. These techniques require the use of multiple windows to maintain high resolution in frequency and depth simultaneously. Here, we demonstrate experimentally SIOCT with a classical incoherent source, confirming both the reduced PSF and the dispersion cancellation in the case of a single interface. We also measure a sample with two interfaces and show how simple numerical post-processing similar to that used to obtain the Wigner distribution of time-varying frequency fields[18] allows to discriminate artefacts arising from cross talk in the higher-order correlation signal. The measurements are in excellent agreement with the theoretical predictions. Our results open up new perspectives for high-resolution imaging using classical light sources.

[1]Optics Laboratory, Department of Physics, Tampere University of Technology, 33720 Tampere, Finland. [2]Institute of Photonics, University of Eastern Finland, P. O. Box 111, FI-80101 Joensuu, Finland. Correspondence and requests for materials should be addressed to G.G. (email: goery.genty@tut.fi)

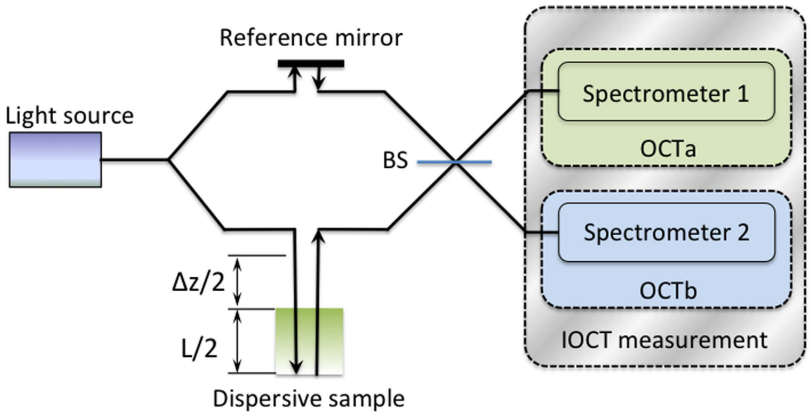

Figure 1. OCT and SIOCT concepts. BS – 50:50 non-polarizing beam splitter. OCT corresponds to a single spectral interference measurement at Spectrometer 1 (or 2). SIOCT corresponds to a simultaneous measurement of spectral interferences at Spectrometers 1 and 2.

Theory

The difference between the principles of the operation of conventional spectral-domain OCT and SIOCT is illustrated in Fig. 1. Light from an incoherent broadband source is divided between the two arms of an interferometer. One arm serves as the reference while the other contains the sample to be characterized. In traditional OCT, the spectral intensity recorded at the output of the beam splitter and resulting from the interference of the light in the two arms is of the form

$$I_{\mathrm{OCTa}}(\omega) \sim \left|E_{\mathrm{S}}(\omega) + \mathrm{i}E_{\mathrm{R}}(\omega)\right|^2, \tag{1}$$

$$I_{\mathrm{OCTb}}(\omega) \sim \left|\mathrm{i}E_{\mathrm{S}}(\omega) + E_{\mathrm{R}}(\omega)\right|^2, \tag{2}$$

where ω is the angular frequency, E_{S} and E_{R} are the complex spectral amplitudes of the electric fields emerging from the sample and reference arms, respectively, and the subscripts a and b denote at which output of the beam splitter the spectral OCT measurement is recorded. The phase difference between the reference and sample arm fields is caused by the difference Δz in distance that the light propagates in air and the propagation through the dispersive sample of path length L. Both distances mark the total path, including wave transits before and after reflection. The intensity of the recorded interferogram can then be written as

$$I_{\mathrm{OCTa}}(\omega) = S(\omega)\left|re^{-\mathrm{i}[\omega\Delta z/c+\beta(\omega)L]} + \mathrm{i}\right|^2, \tag{3}$$

where $S(\omega)$ represents the spectrum of the light source, $r = |r|\exp(\mathrm{i}\phi_s)$ is the (complex) amplitude reflection coefficient of the sample, and c is the speed of light in vacuum. The coefficient $\beta(\omega)$ denotes the frequency-dependent propagation constant within the sample. Using a Taylor-series expansion around the central frequency ω_0 of the source spectrum up to second order, one obtains

$$I_{\mathrm{OCTa}}(\omega) = S(\omega_0+\omega') \times \left|re^{-\mathrm{i}[(\Delta z/c)\omega_0+\beta_0 L+\tau\omega'+(\beta_2 L/2)\omega'^2]} + \mathrm{i}\right|^2, \tag{4}$$

where $\omega' = \omega - \omega_0$ and $\tau = \Delta z/c + \beta_1 L$, with β_0, β_1, and β_2 being the propagation constant, the group delay, and the group-velocity dispersion at frequency ω_0, respectively. The envelope of the spectral interference pattern represents the source spectrum whilst the frequency, phase, and amplitude of the modulation underneath depend on the sample position and reflectance, which can then be obtained through a Fourier transform of the recorded interferogram. The full width at half maximum (FWHM) of the PSF is given by the Fourier transform of the term corresponding to the optical path difference between the reference and sample arms. In the absence of dispersion, the PSF is inversely proportional to the source bandwidth. With dispersion present in the system, the resolution decreases by a factor $[1 + (\beta_2 L)^2(\Delta\omega/2\sqrt{2\ln 2})^4]^{1/2}$, where $\Delta\omega$ is the FWHM spectral bandwidth of the light source.

In SIOCT, the spectral interference patterns of the fields in the two arms are recorded simultaneously by two separate detectors at the two output ports of the beam splitter. The location and reflectance of the sample are obtained from the Fourier transform of the cross product of the individual spectral intensities $C(\omega') = I_{\mathrm{OCTa}}(\omega_0+\omega')I_{\mathrm{OCTb}}(\omega_0-\omega')$. It is straightforward to show that the interference pattern of the SIOCT signal is then given by

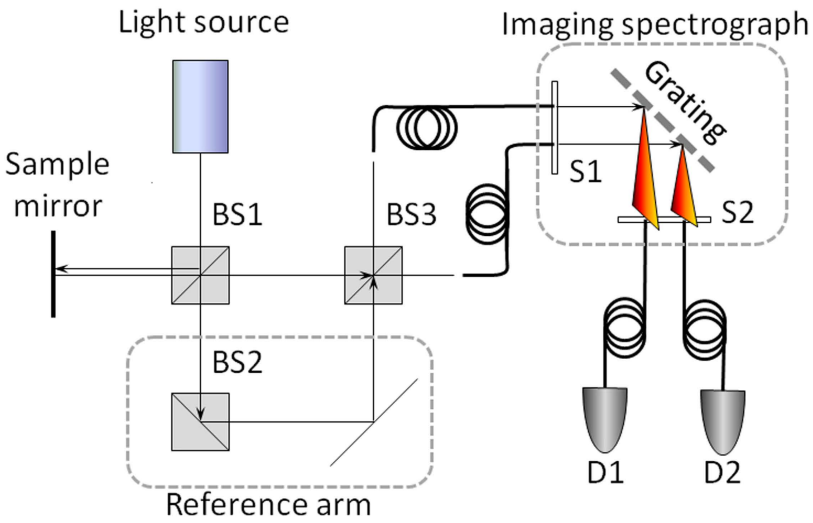

Figure 2. Modified Mach-Zehnder interferometer, experimental setup: BS – 50:50 non-polarizing beam splitter. S1, S2 – spectrograph input and output slits. D1, D2 – photodiodes.

$$C(\omega') = S(\omega_0 + \omega')S(\omega_0 - \omega')[c_0(\omega') + c_1(\omega') + c_2(\omega')], \tag{5}$$

where

$$c_0(\omega') = (|r|^2 + 1)^2 + 2r^2\Re\{e^{-i[2\omega_0(\Delta z/c)+2L(\beta_0-(\beta_2/2)\omega'^2)]}\}, \tag{6}$$

$$c_1(\omega') = -4(|r|^2 + 1)\Im\{e^{-i\tau\omega'}\} \times \Re\{e^{-i[\omega_0(\Delta z/c)+L(\beta_0+(\beta_2/2)\omega'^2)]}\}, \tag{7}$$

$$c_2(\omega') = -2|r|^2\Re\{e^{-i2\tau\omega'}\}, \tag{8}$$

with $\Re$ and $\Im$ denoting the real and the imaginary parts, respectively. One can see that the Fourier transform of the SIOCT signal produces a PSF with a width reduced by a factor of $\sqrt{2}$ compared to that of conventional OCT. The Fourier spectrum of the function $C(\omega')$ gives access to the sample information and consists of three separated peaks corresponding to the Fourier transforms of $c_0(\omega')$, $c_1(\omega')$, and $c_2(\omega')$ convolved by the Fourier transform of $S(\omega_0 + \omega')S(\omega_0 - \omega')$.

Several observations can be made. We first remark that the product $S(\omega_0 + \omega')S(\omega_0 - \omega')$ is always an even function, even if the spectrum of the light source is not symmetrical with respect to ω_0. The term $c_0(\omega')$ is an even function whose Fourier transform produces a real-valued peak centered at the zero delay (equal path lengths). The term $c_1(\omega')$, on the other hand, is an odd function that depends on the optical path length and its Fourier transform corresponds to an imaginary-valued peak centered at the optical path difference between the two arms. Finally, the Fourier transform of $c_2(\omega')$ gives rise to a real, negative-valued peak at twice the optical path difference. It is precisely this peak in the Fourier spectrum that gives information about the sample position and, after correcting for the distance, one obtains an overall PSF reduced by a factor of $\sqrt{2}$ compared to standard OCT. However, it should be noted that this decrease in the PSF width comes with a price: the imaging depth is only half of that obtained by the standard OCT. We further note that the number of data points is identical in both OCT and SIOCT but their density is doubled in SIOCT, allowing for better accuracy in locating interfaces. Note further that in practice the terms arising from $c_1(\omega')$ and $c_2(\omega')$ can be distinguished as one is real and the other imaginary. Besides the point density increase in the measurement, another benefit of SIOCT is the inherent dispersion cancellation of all even-order terms in the Taylor-series expansion. This is because in SIOCT intensities of opposite frequencies relative to central frequency ω_0 are multiplied, cancelling the even-order phase terms that arise from dispersion.

In the case of multiple interfaces, artefacts which have generally complex values appear in the Fourier signal due to cross-talk between the terms corresponding to the multiple interferences. This means that they can not be discriminated from the real interfaces by solely considering the real part of the Fourier transform of the SIOCT interferogram. Yet, in this case, one can take advantage of the fact that the amplitude of the artefacts corresponding to the $c_1(\omega')$ term in Eq. (7) depends on the center frequency ω_0 of the source spectrum. Indeed, for a stationary light source the spectrum does not need to be symmetrical with respect to ω_0, so that one can choose

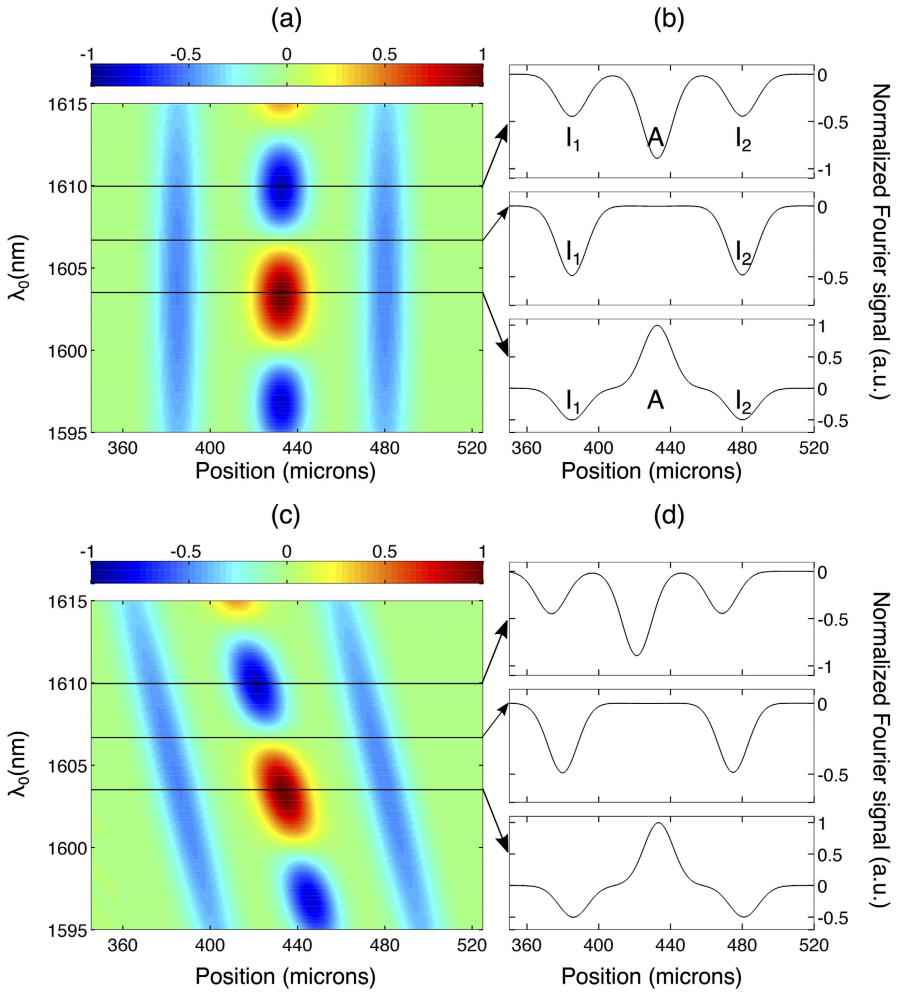

Figure 3. False color representation of the numerically simulated real part of the Fourier signal recorded by the IOCT system vs. center wavelength λ_0 of the light source for two interfaces: (**a**) without dispersion and (**c**) with dispersion. Fourier signal for selected center wavelengths indicated by the arrows: (**b**) without dispersion and (**d**) with dispersion. For clarity, the position of the two interfaces (I_1 and I_2) and artefact A are marked.

arbitrarily the center frequency as long as the detected signal significantly exceeds the measurement noise. Because the phase of the $c_1(\omega')$ term oscillates with ω_0, the amplitude of the peak in the Fourier domain corresponding to artefacts oscillates when spectra of different center frequencies are measured. This is illustrated in Fig. 3 where we show numerical simulations of the Fourier signal recorded for two interfaces separated by 95 μm (optical thickness) as a function of the light source center wavelength $\lambda_0 = 2\pi c/\omega_0$. We show results both without [Fig. 3(a,b)] and with dispersion [Fig. 3(c,d)] present in the system. We can see how in both cases the peaks corresponding to the interface positions always remain negative with a change in amplitude that follows the spectral amplitude of the source vs wavelength. On the contrary, the amplitude of the peak corresponding to the artefact arising from cross-talk oscillates dramatically between negative and positive values. We also note that when dispersion is present, it is cancelled independently of the center wavelength with a constant width for the PSF. Interestingly, multiple measurements with a different center frequency can be numerically performed by post-selection of a smaller number of points from the measured interferogram, which in turn shifts the spectral window together with the central frequency. In this way, one can produce an ensemble of data sets corresponding to spectra with different central frequencies. Therefore, in principle, only a simple post-processing operation of the recorded interferograms is required to discriminate possible artefacts when multiple interfaces are probed.

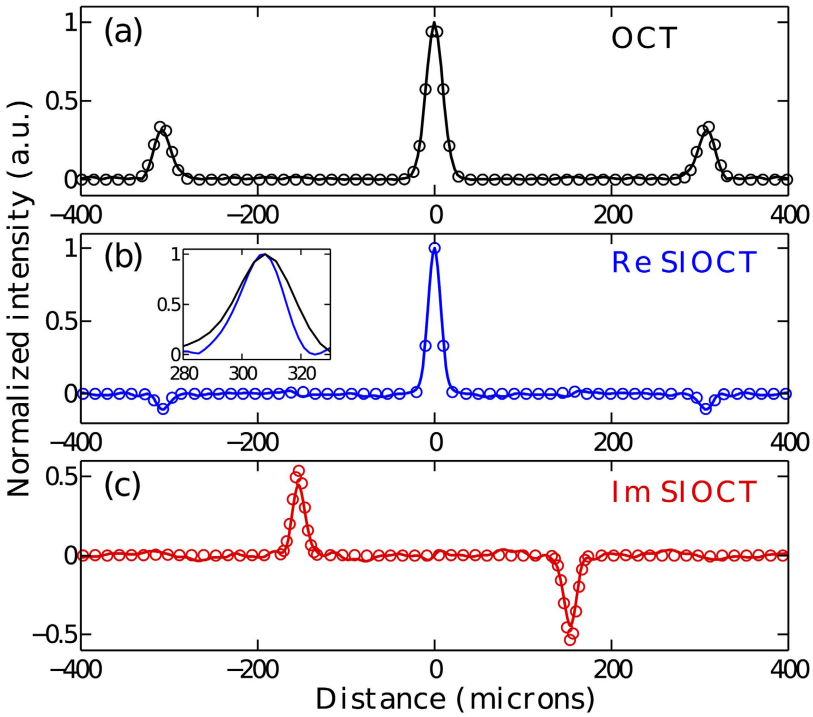

Figure 4. Comparison of OCT and intensity-based SIOCT in the absence of dispersion in the system. The solid lines show the experimental results and the circles correspond to theoretical predictions. (**a**) OCT result. (**b**,**c**) Real and imaginary part of the Fourier transform of the SIOCT interferogram, respectively. The inset in (**b**) displays a direct comparison of the PSF of both techniques: black OCT, blue SIOCT.

Experimental Results

We confirmed experimentally the narrowing of the PSF and dispersion cancellation in SIOCT as compared to standard OCT using a modified Mach-Zehnder interferometer with balanced detection. The experimental setup is shown in Fig. 2 (see also Methods). The signal recorded at either detector independently is identical to a conventional OCT system, while measuring simultaneously the signal at both detectors allows to construct the SIOCT interferogram.

In order to characterize the PSF, we first performed measurements in the absence of dispersion in the sample arm. The results are shown in Fig. 4 where both the real and the imaginary part of the Fourier transform of the cross-product function $S(\omega')$ are presented. For comparison, the theoretical results obtained on the basis of Eqs. (4) and (5) are superimposed as circles. The optical path delay was converted into physical distance as light would travel in vacuum and thereby the 0 point represents equal path lengths. For ease of comparison with the conventional OCT result, the distance was divided by 2 for the SIOCT measurement so that the image peak would correspond to the actual sample position. In general, we observe excellent agreement between the experimental and theoretically predicted results. Specifically, we see that the measured imaginary part of the Fourier spectrum is an odd function and corresponds precisely to the Fourier transform of the term $c_1(\omega')$, while the measured real part is even and matches closely the Fourier transforms of the terms $c_0(\omega')$ and $c_2(\omega')$ of the SIOCT interferogram. Significantly, we also observe how the width of PSF is reduced in comparison to that of standard OCT (see inset in Fig. 4). The FWHMs of the OCT and SIOCT PSFs corresponding to the sample position are respectively equal to 23.5 μm and 17.3 μm, giving a ratio of 0.736 close to the $\sqrt{2}$ theoretical PSF width reduction predicted for a light source with a Gaussian spectrum.

We next proceeded to confirm experimentally the built-in dispersion cancellation of the SIOCT scheme. For this purpose, an 8 cm thick bulk piece of SF10 glass was inserted into the sample arm. In order to increase the effect of dispersion the beam was propagated eight times through the glass cube, effectively corresponding to a 64 cm glass piece. The group-velocity dispersion coefficient of SF10 at 1610 nm is $\beta_2 = 1.63410^{-26}\,s^2/m$, which should lead to a PSF width increase by a factor of about 2.4 in the case of conventional OCT. The measurement results for conventional OCT and SIOCT are illustrated in Fig. 5. As for the dispersionless case, the theoretical results computed from Eqs. (4) and (5) are also superimposed as circles. It can readily be seen that the experimental results in both cases follow the theoretical predictions with great accuracy. More specifically, we observe how in the case of conventional OCT the FWHM of the PSF corresponding to the sample location has broadened

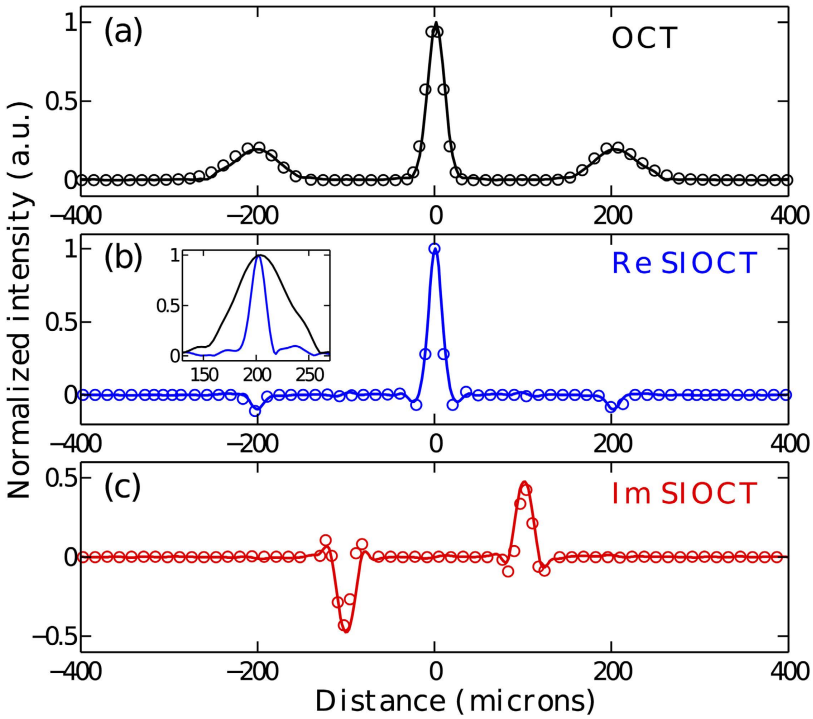

Figure 5. Comparison of OCT and intensity-based SIOCT when dispersion is present in the system. The solid lines show the experimental results and the circles give the theoretical predictions that are based on Eqs. (4) and (5). (**a**) OCT result. (**b**,**c**) Real and imaginary part of the Fourier transform of the SIOCT interferogram, respectively. The inset in (**b**) illustrates the direct comparison of the PSF in the two techniques: black OCT, blue SIOCT.

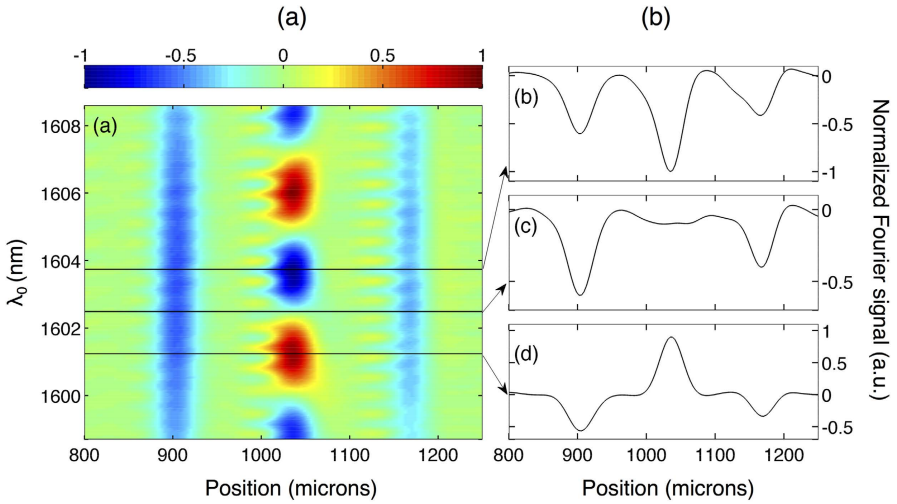

Figure 6. Experimental results for two interfaces. (**a**) False color representation of the numerically post-processed real part of the Fourier signal recorded by the IOCT system vs. center wavelength λ_0 of the spectral window. (**b**) Fourier signal for selected center wavelengths as indicated by the arrows.

nearly 2.5 times to 58.0 μm due to the dispersion of the SF10 glass, a value very close to that expected from the theoretical calculations. Most remarkably, the width of the SIOCT PSF at the sample position is unaffected by the presence of the bulk piece of glass, clearly demonstrating that dispersion is inherently canceled in SIOCT. In fact, the width of the PSF was found to be 16.2 μm, which is even slightly reduced compared to the case when dispersion. This slight change in the resolution is caused by third-order dispersion, which is not canceled in SIOCT (only even order are). Finally, we also see how the artefact peak corresponding to the term $c_1(\omega')$ is generally affected by dispersion, which provides an additional means of discrimination.

We also performed experiments with a dual-interface sample. for this purpose, we inserted a thin microscope cover slip consisting of two air-glass interfaces in the sample arm. Note that no dispersion was added in this case. The results are illustrated in Fig. 6. In order to discriminate the actual interfaces from the artefacts we processed the experimental data by post-selecting a smaller number of points from the measured interferograms which allows to shift numerically the spectral window and center frequency (or wavelength). A false color representation of the real part of the Fourier signal is shown in Fig. 6 as a function of the center wavelength. The amplitude of the artefacts oscillates between positive and negative values as the central wavelength is changed in perfect agreement with the numerical simulations of Fig. 3. In marked contrast, the amplitude of the peaks corresponding to the actual interfaces remains negative independently of the center wavelength of the source and their amplitude follow the spectral intensity of the source vs wavelength. The optical distance between the two interfaces can then be readily inferred to be c.a. 270 μm, resulting in a measured physical thickness of 185 μm for the cover slip in very good agreement with the manufacturer specified value of <200 μm. This experimental result demonstrates a convenient approach to effectively eliminate artefacts in the case of samples with multiple interfaces.

Conclusions

In summary, we have experimentally demonstrated spectral intensity optical coherence tomography and proved the associated reduced point spread function and dispersion cancellation. The imaging depth for SIOCT is only half of the one obtained by the standard OCT but the density of measurement points is doubled in SIOCT allowing for better accuracy in locating interfaces. We further suggested a possible approach to eliminate artefacts that might be present in the case of samples with multiple distinct interfaces. No fast detectors are needed in our technique as only mean spectral intensities are measured. The method works with classical light sources and standard photodiodes, illustrating the simplicity of the technique and showing its potential application to high resolution imaging.

Methods

The light source used in the experiments was a fiber-coupled superluminescent diode (Exalos ESL 1620) with a center wavelength of 1604 nm. The source spectrum is close to Gaussian with a spectral bandwidth of 55 nm (FWHM). The light emitted by the source was collimated with a parabolic mirror and three identical non-polarizing beam-splitter cubes were used to divide the light among the sample and reference arms. A single, partially reflecting mirror placed on a manual translation stage to adjust the optical path length was used as the sample. The reference wave transmitted through beam splitter BS1 was reflected from an additional beam splitter BS2 in order to equalize the dispersion and phase shifts experienced by both beams due to the various optical elements. As a result, any difference between the complex amplitudes of the electric fields in the sample and reference arms before interfering on beam splitter BS3 is caused only by the path difference between the two arms and sample presence. Light at the two output ports of BS3 was coupled to a single-mode fiber using achromatic lenses. The fiber outputs were then placed on top of each other in the object plane of a monochromator (Horiba iHR 550) allowing to measure simultaneously the spectral intensities at the two detectors. On passing through the output slit of the monochromator, light was collected by multimode fibers and intensities were measured by InGaAs amplified diodes (Thorlabs PDA10CS). Lock-in detection was used to improve the signal-to-noise ratio. Wavelength scanning and data acquisition were controlled by a PC.

References

1. Leitgeb, R., Hitzenberger, C. K. & Fercher, A. F. Performance of fourier domain vs. time domain optical coherence tomography. *Opt. Express* **11,** 889 (2003).
2. de Boer, J. F., Cense, B., Park, B. H., Pierce, M. C., Tearney, G. J. & Bouma, B. E. Improved signal-to-noise ratio in spectral-domain compared with time-domain optical coherence tomography. *Opt. Lett.* **28,** 2067 (2003).
3. Fercher, A. F., Drexler, W., Hitzenberger, C. K. & Lasser, T. Optical coherence tomography - principles and applications. *Rep. Prog. Phys.* **66,** 239 (2003).
4. Wojtkowski, M. *et al.* Ultrahigh-resolution, high-speed, fourier domain optical coherence tomography and methods for dispersion compensation. *Opt. Express* **12,** 2404 (2004).
5. Fercher, F. *et al.* Numerical dispersion compensation for partial coherence interferometry and optical coherence tomography. *Opt. Express* **9,** 610 (2001).
6. Banaszek, K., Radunsky, A. & Walmsley, I. Blind dispersion compensation for optical coherence tomography. *Opt. Commun.* **269,** 152 (2007).
7. Erkmen, B. I. & Shapiro, J. H. Phase-conjugate optical coherence tomography. *Phys. Rev. A* **74,** 041601(R) (2006).
8. Gouët, J. L., Venkatraman, D., Wong, F. N. C. & Shapiro, J. H. Experimental realization of phase-conjugate optical coherence tomography. *Opt. Lett.* **35,** 1001 (2010).
9. Lavoie, J., Kaltenbaek, R. & Resch, K. J. Quantum-optical coherence tomography with classical light. *Opt. Express* **17,** 3818 (2009).
10. Mazurek, M. D., Schreiter, K. M., Prevedel, R., Kaltenbaek, R. & Resch, K. J. Dispersion-cancelled biological imaging with quantum-inspired interferometry. *Sci. Rep.* **3,** 1582 (2013).
11. Abouraddy, A. F., Nasr, M. B., Saleh, B. E. A., Sergienko, A. V. & Teich, M. C. Quantum-optical coherence tomography with dispersion cancellation. *Phys. Rev. A* **65,** 053817 (2002).
12. Nasr, M. B., Saleh, B. E. A., Sergienko, A. V. & Teich, M. C. Demonstration of dispersion-canceled quantum-optical coherence tomography. *Phys. Rev. Lett.* **91,** 083601 (2003).

13. Nasr, M. B., Saleh, B. E. A., Sergienko, A. V. & Teich, M. C. Dispersion-cancelled and dispersion-sensitive quantum optical coherence tomography. *Opt. Express* **12,** 1353 (2004).
14. Lajunen, H., Torres-Company, V., Lancis, J. & Friberg, A. T. Resolution-enhanced optical coherence tomography based on classical intensity interferometry. *J. Opt. Soc. Am. A* **26,** 1049 (2009).
15. Zerom, P., Piredda, G., Boyd, R. W. & Shapiro, J. H. Optical coherence tomography based on intensity correlations of quasi-thermal light. In *Conference on Lasers and Electro-Optics/Quantum Electronics and Laser Science Conference (CLEO/QELS), Baltimore, MD,* JWA48 (2009).
16. Shirai, T. & Friberg, A. T. Resolution improvement in spectral-domain optical coherence tomography based on classical intensity correlations. *Opt. Lett.* **38,** 115 (2013).
17. Shirai, T. & Friberg, A. T. Intensity-interferometric spectral-domain optical coherence tomography with dispersion cancellation. *J. Opt. Soc. Am. A* **31,** 258 (2014).
18. Graf, R. N. & Wax, A. Temporal coherence and time-frequency distributions in spectroscopic optical coherence tomography. *J. Opt. Soc. Am. A* **24,** 2186 (2007).
19. Robles, F., Graf, R. N. & Wax, A. Dual window method for processing spectroscopic optical coherence tomography signals with simultaneously high spectral and temporal resolution. *Opt. Express* **17,** 6799 (2011).

Acknowledgements

We thank Tomohiro Shirai for useful discussions and acknowledge the Academy of Finland for financial support (projects 268480 and 267576).

Author Contributions

G.G., J.T. and A.T.F. conceived the original idea. P.R. constructed the experimental setup and conducted all the experiments. G.G. and P.R. designed the experiments. All authors performed the data analysis and contributed to writing the manuscript.

Additional Information

Competing financial interests: The authors declare no competing financial interests.

How to cite this article: Ryczkowski, P. *et al.* Experimental Demonstration of Spectral Intensity Optical Coherence Tomography. *Sci. Rep.* **6**, 22126; doi: 10.1038/srep22126 (2016).

This work is licensed under a Creative Commons Attribution 4.0 International License. The images or other third party material in this article are included in the article's Creative Commons license, unless indicated otherwise in the credit line; if the material is not included under the Creative Commons license, users will need to obtain permission from the license holder to reproduce the material. To view a copy of this license, visit http://creativecommons.org/licenses/by/4.0/

Paper III

Piotr Ryczkowski, Margaux Barbier, Ari T. Friberg,
John M. Dudley and Goëry Genty.

Ghost imaging in the time domain

Nature Photonics / Vol. 10 No. 3, 167–170 / February 1, 2016.

doi: 10.1038/NPHOTON.2015.274

©2016 Macmillan Publishers Limited

Ghost Imaging in the Time Domain

Piotr Ryczkowski,[1] Margaux Barbier,[1] Ari T. Friberg,[2] John M. Dudley,[3] and Goëry Genty[1*]

[1] *Optics Laboratory, Tampere University of Technology, Tampere, Finland*

[2] *Department of Physics and Mathematics, University of Eastern Finland, Joensuu, Finland*

[3] *Institut FEMTO-ST, UMR 6174 CNRS-Université de Franche-Comté, Besançon, France*

Ghost imaging is a novel technique that produces the image of an object by correlating the intensity of two light beams, neither of which independently carries information about the shape of the object[1,2]. Ghost imaging has opened up new perspectives to obtain highly-resolved images[3], even in the presence of noise and turbulence[4]. Here, exploiting duality between light propagation in space and time[5], we demonstrate the temporal analogue of ghost imaging. We use a conventional fast detector that does not see the temporal 'object' to be characterised, and a slow integrating 'bucket' detector that does see the object but without resolving its temporal structure. Our experiments achieve temporal resolution at the picosecond level and is insensitive to temporal distortion that may occur after the object. The approach is scalable, can be integrated on-chip, and offers great promise for dynamic imaging of ultrafast waveforms.

Ghost imaging is based on the correlation between light transmitted through (or reflected by) an object and the spatially-resolved intensity pattern of the incident light and allows the reconstruction of a ghost image of the original object[1]. The principle of spatial ghost imaging is illustrated in Fig. 1(a). The beam from a light source with spatially random intensity pattern is divided between two paths. In one arm (test), the random incident light directly illuminates the object with the scattered light collected by a single-pixel bucket detector which produces only a spatially-integrated signal. In the second arm (reference), the incident light does not see the object at all, but the ran-

dom fluctuations in the beam are measured as a function of spatial position with a high-resolution CCD (Charge-Coupled Device) camera. Neither of the detectors alone can produce an image of the object – yet by correlating the two measurements from the bucket and high-resolution detectors over multiple intensity patterns produced by the source, the object appears like a ghost in the focus plane of the camera. The essential nature of ghost imaging lies in the mutual spatial correlation of the two beams, which may be quantum or classical. Various light sources can be used including spatially-entangled photon sources[2,6–9], classical light sources[2,10–15], or structured light fields programmed by a spatial light modulator to minimise the number of measurements in the time series to obtain an accurate representation of the object[16].

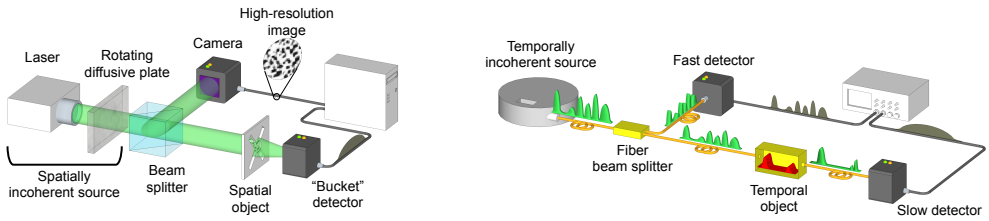

Fig.1. Comparison between spatial (left) and temporal (right) ghost imaging experimental setups.

Many propagation effects in optics first seen in the spatial domain have subsequently been observed in time, exploiting space-time duality - the correspondence between the diffraction of a light beam and the dispersive propagation of a short optical pulse[17–19]. Recently, this duality has successfully enabled major advances in the processing of time-varying signals including all-optical magnification of ultrafast data rates by a thousand fold[20,21], all-optical correlation[5], real-time detection of single-shot spectra at hundreds of MHz speed[22], or temporal cloaking[23]. It has also been suggested theoretically[24] and numerically[25] that this duality may allow the transposition of the concept of ghost imaging to the temporal domain. Here, we confirm this proposal experimentally, demonstrating how intensity correlation measurements from a temporally fluctuating light source allows retrieval of a structure of a rapidly varying temporal object that modulates the amplitude of

the transmitted or reflected light.

We implement temporal ghost imaging using an optical fibre-based system shown in Fig. 1(b). The random intensity fluctuations of a laser diode replace a random spatial beam, and the temporal intensity modulation of the incident light field imposed by an ultrafast optical modulator replaces the scattering from a spatial object. In this sense, the 'structured illumination' used in the ghost imaging arises from the intrinsic randomness in the temporal fluctuations of the light emitted by the laser diode, a quasi-continuous multimode laser operating at $\lambda = 1547$ nm. The bandwidth is $\Delta\lambda = 0.6$ nm, resulting in random intensity fluctuations with a characteristic time $\tau_c = \lambda^2/(c\,\Delta\lambda) \approx 13$ ps where c is the speed of light in vacuum. At the output of the source, the intensity is equally divided between the test and reference arms with a 50/50 fibre coupler which replaces the beam splitter in the spatial setup. In the reference arm, the temporal fluctuations of the source are measured with a 25-GHz photodiode and a 20-GHz real-time oscilloscope, which results in an effective fluctuation time $\tau_c^{\text{eff}} = 50$ ps. Multiple series of intensity fluctuations measured from the reference arm and recorded over a 2-ns time window are plotted in Fig. 2. One can clearly observe the random fluctuations of the intensity with an effective characteristic time of approximately 50 ps. We can also see that the intensity of the source averaged over a large series of consecutive 2-ns segments is constant, which ensures that the retrieved ghost image is directly proportional to the object[24] (see also Methods). In the test arm, the temporal object is an ultrafast electro-optic modulator (EOM) driven by a 10 Gb/s pulse pattern generator which temporally modulates ('scatters') the chaotic light (see Methods). The light transmitted through the object is detected by a slow photodiode with 5-ns response time, which is too slow to resolve the fast variations of the bit sequence.

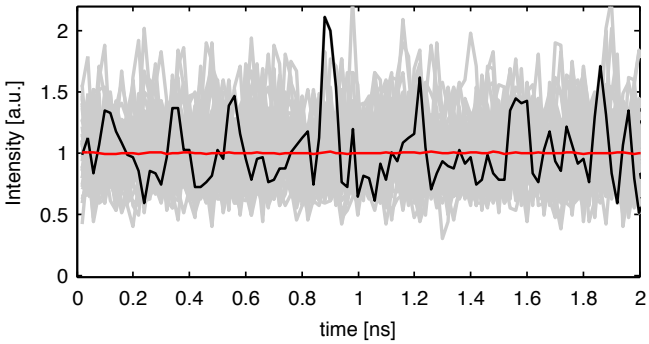

Fig.2. Measured intensity fluctuations of the chaotic laser source. A single realisation (black) is shown together with 50 other realisations (grey). The average intensity of 5 000 realisations is shown as the red line.

The normalised intensity correlation function $C(t)$ (i.e. the ghost image) calculated over a series of time signals measured simultaneously from both arms is defined by:

$$C(t) = \frac{\langle \Delta I_{\text{ref}}(t) \cdot \Delta I_{\text{test}} \rangle_N}{\sqrt{\langle [\Delta I_{\text{ref}}(t)]^2 \rangle_N \, \langle [\Delta I_{\text{test}}]^2 \rangle_N}}. \tag{1}$$

Here, $I_{\text{ref}}(t)$ represents the time-resolved intensity measurement from the reference arm at time t and I_{test} is the integrated intensity from the test arm. $\langle\,\rangle_N$ denotes ensemble average over a series of N realisations, and $\Delta I = I - \langle I \rangle_N$. Figure 3 shows the ghost image obtained from a series of $N = 80\,000$ realisations where the temporal intensity fluctuations of the light source follow a random pattern in each of the realisations. The agreement with the direct image of the object measured with the fast detector is remarkable. Specifically, the temporal object (the transmission of the EOM driven by the bit sequence) is precisely reproduced both in terms of duration and amplitude.

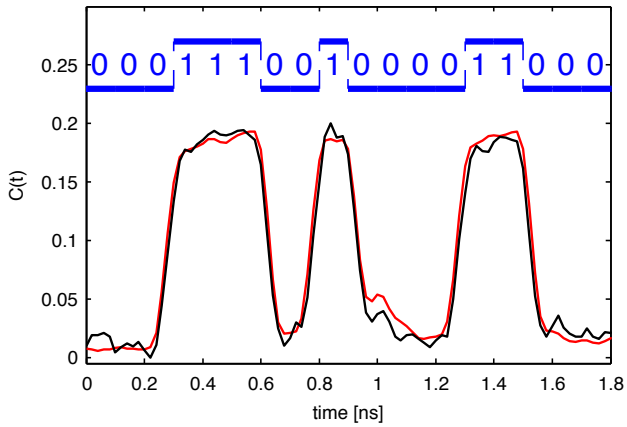

Fig.3. Comparison between the ghost image (black) and direct image measured with the fast detector (red). The bandwidth of the detection is equal to 20 GHz, corresponding to an effective fluctuation time of 50 ps. The number of realisations in the measurement series for the ghost image is equal to N = 80 000.

The performance of the ghost imaging system can be characterised by (i) the temporal resolution and (ii) the signal-to-noise ratio (SNR). The temporal resolution directly corresponds to the effective fluctuation time (i.e. the maximum value between the coherence time of the source and the response time of the fast detector/oscilloscope – see Methods), which must then be shorter than the object variations that one wants to resolve. The SNR is given by[26]:

$$\mathrm{SNR}(t) = \frac{C(t)\,\sqrt{N}}{1 - C^2(t)}, \tag{2}$$

assuming that the noise from the detectors is negligible. The SNR is therefore expected to increase with the number of realisations and this is shown in Fig. 4(a-d) (see also the movie in the Supplementary Material for a full evolution of the ghost image as a function of the number of realisations). Note that the amplitude of the ghost image should be independent of the number of measurements, which can be readily observed in the figure. For a fixed number of realisations, the SNR can be

improved by increasing the effective fluctuation time of the source. In practice, this can be done in two different ways, depending on which parameter limits the value of τ_c^{eff}: either by increasing the coherence time of the source or by decreasing the fast detector bandwidth. As a rule of thumb, in order to obtain a ghost image at fast acquisition rates, yet with a high temporal resolution and optimum SNR, the effective fluctuation time should be equal to half of the fastest time variations that one wants to resolve in the object (Nyquist criterion). For the 100-ps bits that constitute the object here, the effective fluctuation time for optimum SNR and acquisition time is then 50 ps. Lower values may improve the temporal resolution at the expense of the SNR whilst higher values will result in the opposite. Ghost images recorded for a fixed number of measurements (N = 5 000) with the detection bandwidth in the reference arm decreasing from 20 to 3 GHz (and thus the effective fluctuation time increasing from 50 to 300 ps) are shown in Fig. 4(e-h).

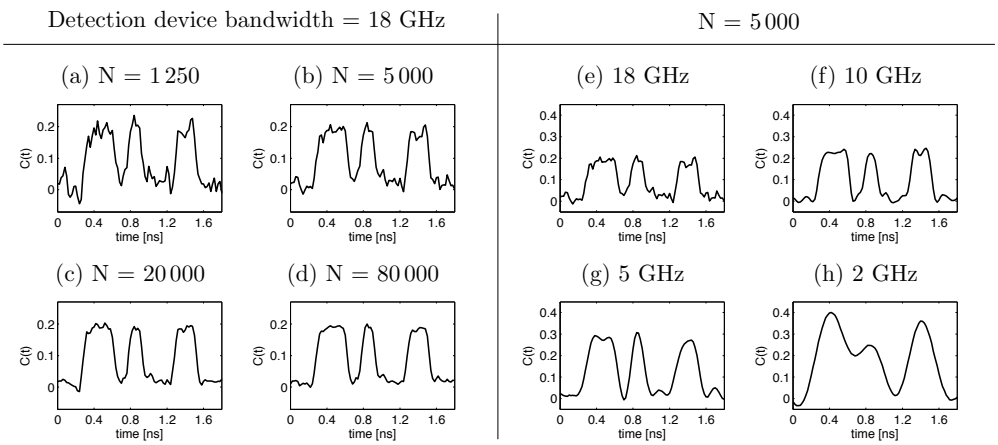

Fig.4. Ghost image as a function of the number of realisations and the effective fluctuation time. In figures (a-d) the number of realisations N increases from 1 000 to 80 000, and in figures (e-h) the effective fluctuation time τ_c^{eff} increases from 50 to 300 ps, as indicated. The temporal object is identical to that in Fig.3.

One can clearly see how the SNR is improved as the effective fluctuation time is increased but that this improvement occurs at the expense of temporal resolution in the ghost image.

Ghost imaging is insensitive to distortion that may occur between the object and the bucket detector. This remarkable particularity has attracted considerable attention in the spatial domain with the possibility of performing high resolution imaging even in the presence of a strong scattering medium or atmospheric turbulence when any direct measurement would result in a poor-quality image. This particularity also applies in the time domain and we demonstrate that the technique allows overcoming the distortion experienced by the modulated light field after the temporal object. For this purpose, a 20-m multimode fibre is inserted after the EOM, which strongly distorts the bit pattern. The results in Fig. 5 clearly show how the intermodal dispersion accumulated in the multimode fibre severely distorts a direct measurement of the temporal object performed with a fast detector. But when the ghost imaging is used, the distortion is washed out and it has no influence on the quality of the ghost image. More generally, ghost imaging in the time domain allows compensating for arbitrary distortion experienced by a temporal object.

These experiments represent the first demonstration of ghost imaging in the time domain. Using an all-fibre setup and a chaotic laser source, our results illustrate how an ultrafast temporal object with structure on a scale of 10 Gb/s can be measured with ~ 50 ps temporal resolution without directly detecting the object. The technique can be adapted to the detection of all-optical data streams by modulating the temporal fluctuations of the light source through e.g. four-wave mixing in a nonlinear fibre. The system is scalable to any data rate and shape by adapting the coherence time of the source. Adjusting the fast detector bandwidth and number of distinct measurements allows for optimising the measurement speed and SNR. We also emphasise that a quantum version of the temporal ghost imaging system can be implemented using entangled photon pairs. The setup can also be modified to include a time lens[27] in the reference arm and thereby magnify the ghost

image[24]. Our results open novel perspectives for dynamic imaging of ultrafast waveforms when the waveform has been severely distorted by the transmission medium, in the presence of high noise or low signal strength and we anticipate applications in communications, remote sensing and ultrafast spectroscopy.

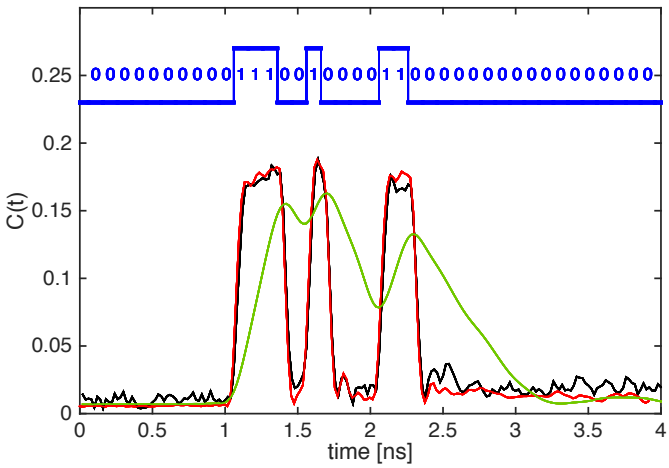

Fig.5. Comparison between the ghost image (in black) and the direct image (in green) in the presence of strong dispersion experienced by the object in a multimode fibre added between the EOM and the detector. For comparison, the direct image obtained without the multimode fibre is also shown in red. Both direct measurements are performed with the fast detector. The bandwidth of the detection is equal to 20 GHz, corresponding to an effective fluctuation time of 50 ps. The number of realisations in the measurement series for the ghost image is equal to $N = 100\,000$.

Methods

In our experiments, the object is created by a zero-chirp 10-GHz bandwidth electro-optic modulator (Thorlabs LN81S-FC) driven by a pulse pattern generator (Advantest D3186). The 10-GHz clock signal was generated by a microwave signal generator (Rohde & Schwarz SMR20) resulting in bits of 100-ps duration. The detector in the test arm is a 1.2-GHz InGaAs photodiode (Thorlabs DET01CFC). Its response is integrated over 5 ns, such that the effective bandwidth is equal to 0.2 GHz only. The detector in the reference arm measuring the intensity fluctuations of the source is a 25-GHz UPD-15-IR2-FC InGaAs photodiode (ALPHALAS). The oscilloscope is a 20-GHz, 50-Gsamples/s real-time oscilloscope (DSA72004 Tektronix). The object was repeated periodically with a period of 50 ns. As a result, the data acquisition time required for 100 000 realisations is of the order of 5 ms only.

The coherence time τ_c of the source is the characteristic time of its intensity fluctuations. If the response time τ_{det} of the fast detection device (detector + oscilloscope) in the reference arm is shorter than τ_c (i.e. if the detection device can resolve the fluctuations of the source), then the temporal resolution of the ghost imaging process is equal to τ_c: object details that are faster that τ_c cannot be resolved. However, if τ_{det} is longer than τ_c (as it is the case in our experiments, with $\tau_c \sim 13$ ps and $\tau_{det} \sim 50$ ps), then the characteristic time of the intensity fluctuations that are effectively recorded by the detection device is $\tau_c^{eff} \sim \tau_{det}$ ($> \tau_c$), and the temporal resolution of the ghost imaging process is thus increased to τ_{det}. As a rule of thumb, one can remember that the temporal resolution is given by τ_c^{eff}, which is the maximum value between τ_c and τ_{det}.

In order to have a direct correspondence between the correlation and the original object it is important that the intensity fluctuations averaged over the number of realisations is constant over the measurement time window of a single realisation. This condition is generally fulfilled in the case of a quasi-CW light source but does not hold if one uses a pulsed light source. In this

latter case, the temporal object would be distorted by the time variation of the average intensity (or average pulse shape)[24].

All the fibres are SMF-28 patch cords of 1-m length with dispersion parameter of 18 ps/(nm.km) at 1550 nm, except the multimode fibre used to add distortion, which is a 29-m FG105LCA fibre. Due to the fact that the SMF-28 fibres are short, the dispersion accumulated during the propagation from the source to the fast detector on the one hand, and from the source to the object (EOM) on the other hand, is negligible. That is why no temporal lens is needed to perform the imaging process – and the magnification factor between the object and the ghost image is simply equal to 1. This situation is equivalent in the spatial case to the near-field regime as described in Ref. 11.

1. Erkmen, B. I. & Shapiro, J. H. Ghost imaging: from quantum to classical to computational. *Adv. Opt. Photonics* **2**, 405 (2010).

2. Bennink, R. S., Bentley, S. J., Boyd, R. W. & Howell, J. C. Quantum and classical coincidence imaging. *Phys. Rev. Lett.* **92**, 033601 (2004).

3. Ferri, F., Magatti, D., Gatti A., Bache, M., Brambilla, E., & Lugiato, L. A. High-resolution ghost image and ghost diffraction experiments with thermal light. *Phys. Rev. Lett.* **94**, 183602 (2005).

4. Meyers, R. E., Deacon, K. S. & Shih, Y. Turbulence-free ghost imaging. *Appl. Phys. Lett.* **98**, 111115 (2011)

5. Salem, R., Foster, M. A. & Gaeta, A. L. Application of space-time duality to ultrahigh-speed optical signal processing. *Adv. Opt. Photon.* **5**, 274 (2013).

6. Klyshko, D. N. A simple method of preparing pure states of an optical field, of implementing the Einstein-Podolsky-Rosen experiment, and of demonstrating the complementarity principle. *Sov. Phys. Usp.* **31**, 74 (1988).

7. Klyshko, D. N. Combine EPR and two-slit experiments: Interference of advanced waves. *Phys. Lett. A* **132**, 299 (1988).

8. Pittman, T. B., Shih, Y. H., Strekalov, D. V. & Sergienko, A. V. Optical imaging by means of two-photon quantum entanglement. *Phys. Rev. A* **52**, R3429 (1995).

9. Abouraddy, A. F., Saleh, B. E. A., Sergienko, A. V. & Teich, M. C. Role of entanglement in two-photon imaging. *Phys. Rev. Lett.* **87**, 123602 (2001).

10. Bennink, R. S., Bentley, S. J. & Boyd, R. W. "Two-photon" coincidence imaging with a classical source. *Phys. Rev. Lett.* **89**, 113601 (2002).

11. Scarcelli, G., Berardi, V. & Shih, Y. Can two-photon correlation of chaotic light be considered as correlation of intensity fluctuations? *Phys. Rev. Lett.* **96**, 063602 (2006).

12. Meyers, R., Deacon, K. S. & Shih, Y. Ghost-imaging experiment by measuring reflected photons. *Phys. Rev. A* **77**, 041801 (2008).

13. Shirai, T., Setälä, T. & Friberg, A. T. Ghost imaging of phase objects with classical incoherent light. *Phys. Rev. A* **84**, 041801 (2011).

14. Zhang, C., Guo, S., Cao, J., Guan, J. & Gao, F. Object reconstitution using pseudo-inverse for ghost imaging. *Opt. Express* **22**, 30063 (2014).

15. Karmakar, S., Meyers, R. & Shih, Y. Ghost imaging experiment with sunlight compared to laboratory experiment with thermal light. in *Proceedings of SPIE 8518 (Quantum Communications and Quantum Imaging X)* 851805 (2012).

16. Sun, B. *et al.* 3D computational imaging with single-pixel detectors. *Science* **330**, 844-847 (2015).

17. Tournois, P. Analogie optique de la compression d'impulsions. *C. R. Acad. Sci.* **258**, 3839 (1964).

18. Kolner, B. H. & Nazarathy, M. Temporal imaging with a time lens. *Opt. Lett.* **14**, 630-632 (1989).

19. Kolner, B. H. Space-time duality and the theory of temporal imaging. *IEEE J. Quant. Electron.* **30**, 1951 (1994).

20. Foster, M. A. *et al.* Silicon-chip-based ultrafast optical oscilloscope. *Nature* **456**, 81-84 (2008).

21. Schröder, J. *et al.* Aberration-free ultra-fast optical oscilloscope using a four-wave mixing based time-lens. *Opt. Comm.* **283**, 2611 (2010).

22. Solli, D. R., Herink, G., Jalali, B. & Ropers, C. Fluctuations and correlations in modulation instability. *Nature Photon.* **6**, 463-468 (2012)

23. Fridman, M., Farsi, A., Okawachi, Y. & Gaeta, A. L. Demonstration of temporal cloaking. *Nature* **481**, 62-65 (2012).

24. Shirai, T., Setälä, T. & Friberg, A. T. Temporal ghost imaging with classical non-stationary pulsed light. *J. Opt. Soc. Am. B* **27**, 2549 (2010).

25. Chen, Z., Li, H., Li, Y., Shi, J. & Zeng, G. Temporal ghost imaging with a chaotic laser. *Opt. Eng.* **52**, 076103 (2013).

26. Soper, H. E. On the probable error of the correlation coefficient to a second approximation waveforms. *Biometrika* **9**, 91 (1913).

27. Salem, R. *et al.* Optical time lens based on four-wave mixing on a silicon chip. *Opt. Lett.* **33**, 1047 (2008).

Acknowledgments G. G. and A. T. F gratefully acknowledge support from the Academy of Finland (project 268480 and 267576). J. M. D. acknowledges the ERC project MULTIWAVE.

Author contributions G. G. and A. T. F. conceived the original idea. P. R. and M. B constructed the experimental setup and conducted all the experiments. G. G. designed the experiments and supervised the project. P. R, M. B, J. M. D and G. G performed the data analysis. All authors contributed to writing the manuscript.

Competing financial interests The authors declare that they have no competing financial interests.

Paper IV

Piotr Ryczkowski, Margaux Barbier, Ari T. Friberg,
John M. Dudley and Goëry Genty.

Magnified Time-Domain Ghost Imaging

submitted to Optica.

doi: tba.

Magnified Time-Domain Ghost Imaging

PIOTR RYCZKOWSKI[1,*], MARGAUX BARBIER[1,2], ARI T. FRIBERG[3], JOHN M. DUDLEY[4], AND GOËRY GENTY[1]

[1] Optics Laboratory, Tampere University of Technology, Tampere, Finland
[2] current affiliation: FOTON Laboratory, CNRS, University of Rennes 1, ENSSAT, 6 rue de Kerampont, F-22305 Lannion, France
[3] Department of Physics and Mathematics, University of Eastern Finland, Joensuu, Finland
[4] Institut FEMTO-ST, UMR 6174 CNRS-Université de Bourgogne-Franche-Comté, Besançon, France
[*] Corresponding author: piotr.ryczkowski@tut.fi

Compiled August 31, 2016

Ghost imaging allows to image an object without directly seeing this object. Originally demonstrated in the spatial domain using classical or entangled-photon sources, it was recently shown that ghost imaging can be transposed into the time domain to detect ultrafast signals with high temporal resolution. Here, using an incoherent supercontinuum light source whose spectral fluctuations are imaged using spectrum-to-time transformation in a dispersive fiber, we experimentally demonstrate magnified ghost imaging in the time domain. Our approach is scalable and allows to overcome the resolution limitation of time-domain ghost imaging. © 2016 Optical Society of America

OCIS codes: (110.1758) Imaging systems, computational imaging; (110.6915) Imaging systems, time imaging; (320.6629) Ultrafast optics, supercontinuum generation.

http://dx.doi.org/10.1364/optica.XX.XXXXXX

1. INTRODUCTION

Ghost imaging allows the indirect retrieval of the image of an object illuminated by a spatially-structured pattern. The image is obtained from the correlation between the spatially-resolved structured illumination pattern and the total intensity transmitted through (or reflected by) the object [1, 2]. Ghost imaging has been extensively studied in the spatial domain since the mid-1990s, using various types of light sources ranging from spatially-entangled photons sources [2–6] to spatially incoherent classical light sources [2, 7–11] and, more recently, pre-programmed illumination by a spatial light modulator [12]. More advanced schemes based on multiplexing have also been demonstrated to reduce the acquisition time [13] or to image objects which vary slowly with time[14]. Compared to standard imaging techniques, a unique property of ghost imaging is its insensitivity to distortions that may occur between the object and the single-pixel detector that only measures the total transmitted (or reflected) intensity [15, 16]. This inherent insensitivity to external perturbations makes ghost imaging particularly appealing for long range applications such as e.g. LIDAR or atmospheric sensing. Recently, exploiting space-time duality in optics [17–20], ghost imaging was transposed into the time domain to produce the image of an ultrafast signal by correlating in time the intensity of two light beams, neither of which independently carried information about the signal [21]. Significantly, it was also demonstrated that the technique is insensitive to distortion that the signal may experience between the object and the detector e.g. due to dispersion, nonlinearity, or attenuation. A potential important limitation of ghost imaging in the time-domain is the finite resolution determined by the fluctuation time of the random light source and/or the speed of the detection system that measures the random intensity fluctuations. Here, we improve significantly the resolution of ghost imaging in the time-domain by reporting a new proof-of-concept experimental setup that allows to generate a magnified ghost image of an ultrafast waveform. Our approach is inspired by shadow imaging in the spatial domain and builds on the dispersive Fourier transform of the fast flucutuations of an incoherent supercontinuum (SC). Dispersive Fourier transform uses the group-velocity dispersion of optical fibers to convert into the time domain spectral fluctuations [22], and it has been successfully applied in the past to single-shot spectral studies of nonlinear instabilities in fiber optics [23], or to perform analog-to-digital conversion and dynamic imaging [22]. By improving significantly the resolution of time-domain ghost imaging, our results open a new avenue to blindly detect and magnified ultrafast signals.

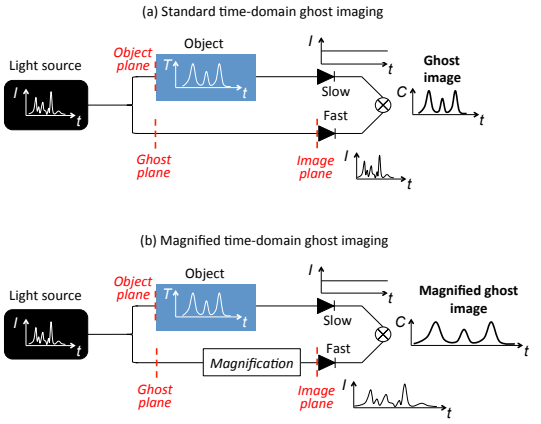

Fig. 1. Operation principle of (a) standard time-domain ghost imaging, and (b) magnified time- domain ghost imaging. The ghost plane is defined in the reference arm as the equivalent of the object plane (which is, by definition, located in the test arm), such that the dispersion accumulated by the light between the source and the ghost plane is equal to the dispersion accumulated between the source and the temporal object. I = light intensity. T = transmission of an intensity modulator (= object). C = correlation function (see Materials and Methods section).

2. MAGNIFIED TIME-DOMAIN GHOST IMAGING USING DISPERSIVE FOURIER TRANSFORM

In time-domain ghost imaging, the fast temporal fluctuations of an incoherent light source are divided between a test arm where a temporal object modulates the intensity fluctuations of the source, and a reference arm where the fluctuations are resolved in real time in the image plane [21] (i.e. the plane of the detector, see Fig. 1). By correlating the time-resolved fluctuations from the reference arm with the total (integrated) power transmitted in the test arm, a perfect copy of the temporal object can be retrieved (see Fig. 1a). The temporally incoherent light source may be a quasi-continuous wave source with a fluctuation time inversely proportional to the source bandwidth, or a pulsed source with large intensity variations within a single pulse and from pulse to pulse [24]. The correlation is calculated from multiple measurement synchronized with the temporal object. Note that the average intensity profile of the source over the measurement time window does not affect the ghost image. However, if the magnitude of the source intensity fluctuations varies over the duration of the temporal object (which can be the case especially for a pulsed source), the ghost image is distorted and requires post-processing correction [24].

In order to obtain a magnified ghost image, the temporal fluctuations of the source in the reference arm must be magnified [24] whilst in the test arm one only needs to measure the total (integrated) intensity with no modification compared to standard time-domain ghost imaging (see Fig. 1b). Magnification of the source fluctuations can be, in principle, obtained using a time lens system [25–27]. However, time lens systems generally require complicated schemes to impose the necessary quadratic chirp onto the signal to be magnified and typically operate only at a fixed repetition rate with limited numerical apertures.

A more straightforward approach consists in using spectrum-to-time transformation of the random shot-to-shot spectral fluctuations of a pulsed incoherent light source as illustrated in Fig. 2. Because the SC is incoherent, the characteristic frequency of the spectral fluctuations is well-approximated by $\Delta\omega_c \approx 1/\Delta T_0$ where ΔT_0 is the average duration of the SC pulse. These spectral fluctuations are first converted into the time domain using a dispersive fiber with total dispersion $\beta_2 L_a$, resulting in pulses with (intra-pulse) temporal fluctuations $\tau_c^{GP} \approx |\beta_2| L_a/\Delta T_0$ at the ghost plane (defined as the equivalent of the object plane in the reference arm, see Fig. 1). These fluctuations are then divided between the test arm where the temporal object is located and the reference arm where they are stretched further in another dispersive fiber with total dispersion $\beta_2 L_b$. The fluctuation time at the image plane (i.e. after propagation in the second dispersive fiber of length L_B) is $\tau_c^{IP} \approx |\beta_2|(L_a + L_b)/\Delta T_0$, such that the temporal fluctuations in the image plane are magnified by a factor $M = (\beta_2 L_a + \beta_2 L_b)/\beta_2 L_a = 1 + L_b/L_a$ compared to the fluctuations in the ghost plane (see Fig. 2a).

By correlating the magnified random fluctuations measured in the reference arm with the total transmitted intensity through the object in the test arm, one then directly obtains an M-time magnified image of the temporal object. The initial duration ΔT_0 of the SC pulses is finite such that each time instant in the ghost plane (and, equivalently in the test arm, each time instant of the temporal object) actually includes the contribution from several spectral components. These spectral components propagate to the image plane with different group-velocities due to dispersion (see Fig. 2b), which results in a "temporal blur effect" that limits the resolution of the imaging system. The temporal blur is defined as the delay τ_s, in the image plane, between the frequencies corresponding to the temporal edges of the initial SC pulses and contributing to the same time instant in the ghost plane (see Supplement 1). Basic geometric considerations in Fig. 2b) show that:

$$\tau_s = \frac{L_b}{L_a}\Delta T_0 = (M-1)\Delta T_0 \qquad \textbf{(1)}$$

For each SC pulse i, the oscilloscope records a pair of measurements: the magnified fluctuations $I_{\text{ref}}^{(i)}(t)$, and the total intensity transmitted through the electro-optic modulator $I_{\text{test}}^{(i)}$. This pair is recorded N times, and the normalized correlation function which produces the ghost image is then calculated according to:

$$C(t) = \frac{\left\langle \Delta I_{\text{ref}}^{(i)}(t) \cdot \Delta I_{\text{test}}^{(i)} \right\rangle}{\sqrt{\left\langle \left[\Delta I_{\text{ref}}^{(i)}(t)\right]^2 \right\rangle \left\langle \left[\Delta I_{\text{test}}^{(i)}\right]^2 \right\rangle}} \qquad \textbf{(2)}$$

where $\langle\rangle$ represents the ensemble average over the N realizations ($i = 1 \ldots N$), and $\Delta I^{(i)} = I^{(i)} - \langle I^{(i)} \rangle$.

3. EXPERIMENTAL SETUP

The experimental setup is illustrated in Fig. 3a). The light source is a spectrally filtered incoherent SC with large shot-to-shot spectral fluctuations. It is generated by injecting 0.5-ns pulses produced by an Erbium-doped fiber laser (Keopsys PEFL-KULT) operating at 1547 nm with 100-kHz repetition rate into the anomalous dispersion regime of a 6-m long dispersion-shifted fiber (Corning ITU-T G.655) with zero-dispersion at 1510

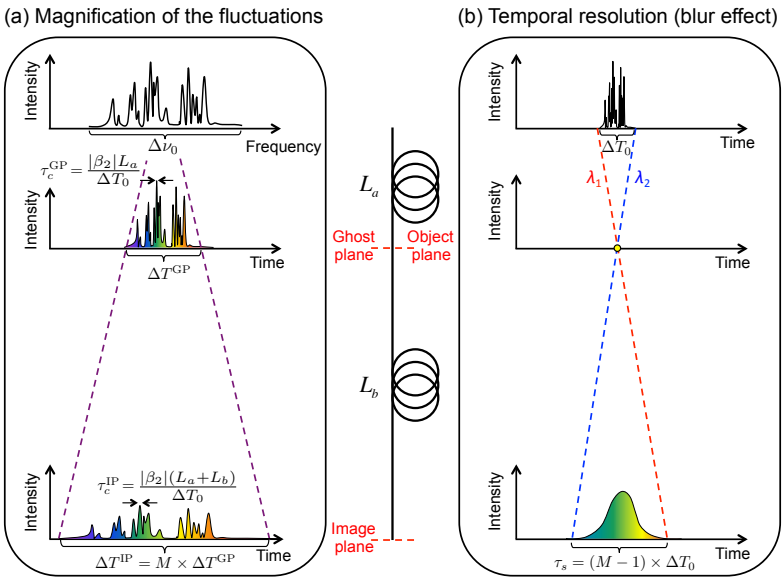

Fig. 2. Spectrum-to-time transformation of the incoherent supercontinuum (SC). (a) Temporal magnification of the intensity fluctuations of the SC. (b) Temporal resolution limit from the finite duration of the SC pulses. ΔT_0 and $\Delta\nu_0$ represents the initial duration and bandwidth of the SC pulses, respectively. ΔT^{GP}, and ΔT^{IP} represent the duration of the SC pulses at the ghost and image planes, respectively. τ_c^{GP} and τ_c^{IP} denote the characteristic fluctuation time within each SC pulse at the ghost and image planes, respectively. τ_s is the temporal blur resulting from the different spectral components λ_1 and λ_2 that corresponds to the temporal edges of the initial SC pulses and temporally overap in the ghost plane.

nm. The spectral components of the resulting SC below 1550 nm are filtered out with a long-pass filter to obtain a relatively flat specturm. The average power of the SC is then reduced with an attenuator (Thorlabs VOA50-FC) to avoid any nonlinear processes that may occur during further propagation in an optical fiber.

The spectral fluctuations are converted into the time domain using an SMF-28 fiber of length $L_a = 2.5$ km and dispersion parameter $\beta_2 = -20$ ps^2/km at 1550 nm. They are then split between the test and reference arm with a 50/50 coupler. In the test arm, the temporal object is the transmission of a zero-chirp 10-GHz-bandwidth electro-optic modulator (Thorlabs LN81S-FC) driven by a programmable nanosecond pulse generator (iC-Haus iC149). It consists of two 0.75-ns pulses with different amplitudes, spanning a total duration of 3.5 ns. In the reference arm, the temporal fluctuations are magnified with an additional SMF-28 fiber of length $L_b = 10$ km.

The detector in the test arm is a 5-GHz InGaAs photodiode (Thorlabs DET08CFC/M) whose response is integrated over 5 ns, such that the effective bandwidth is equal to 0.2 GHz only and the temporal profile of the object cannot be resolved in the test arm. The detector in the reference arm is a 1.2-GHz InGaAs photodiode (Thorlabs DET01CFC). The intensities measured by the two detectors are recorded by a real-time oscilloscope (Tektronix DSA72004). The detection bandwidth was intentionally limited to 625 MHz (with a sampling rate of 6.25 GS/s). Thus, the effective response time of the detection system that measures the fluctuations in real time in the reference arm is τ_d = 1.6 ns.

4. RESULTS AND DISCUSSION

Initially (i.e. immediately after the spectral filtering stage), the SC has a bandwidth of 80 nm and the average duration of the SC pulses ΔT_0 was measured to be less than 200 ps. Note that the duration of the SC after filtering is shorter than the original pump pulses. At the ghost and object planes (i.e. after the first 2.5-km dispersive stage), the average duration of the SC pulses ΔT^{GP} was measured to be c.a. 4 ns. The standard deviation of the magnitude of the fluctuations is nearly constant over this time span (see the dotted black curve in the inset of Fig. 3b), such that the ghost image will not be distorted. At the image plane (i.e. after the second 10-km dispersive stage), the average duration of the SC pulses ΔT^{IP} was measured to be c.a. 20 ns, a 5 times increase compared to the original duration, as expected.

The correlation $C(t)$ calculated over $N = 100\,000$ SC pulses allows us to construct a ghost image magnified by a factor of $M = 5$, as shown in Fig. 4. In this figure, we compare the ghost image with the original temporal object measured directly with a continuous-wave laser and 5-GHz photodiode (Thorlabs DET08CFC/M) and magnified 5 times through post-processing. We can see excellent agreement, both in terms of duration and amplitudes ratio of the object pulses, confirming the 5-time magnification factor of the object duration in the ghost imaging configuration.

There are some constraints which needs to be considered for optimum resolution of the temporal object. Firstly, the time span of the fluctuations in the ghost plane (i.e. the duration of the SC pulses after the first dispersive fiber ΔT^{GP}) needs to be longer or equal to that of the temporal object to be retrieved. This criterion is actually satisfied in our experiment, since $\Delta T^{\mathrm{GP}} \approx 4$ ns and the total duration of the object is only 3.5 ns. Secondly, the characteristic fluctuation time within each SC pulse at the ghost plane τ_c^{GP} needs to be shorter than the shortest object detail that one wishes to resolve. The temporal resolution τ_R of the imaging scheme is then determined by the combination of (i) the time response τ_d of the detection system, (ii) the characteristic time τ_c^{GP} of the random intensity fluctuations in each SC pulse at the ghost plane, and (iii) the initial durationΔT_0 of each SC pulse (i.e. before the spectrum-to-time transformation) which induces a temporal blur $\tau_s = (M-1)\Delta T_0$ in the image plane, as discussed in the previous section (see Fig. 2b). The overall resolution can then be approximated as

$$\tau_R = \sqrt{\left(\frac{\tau_d}{M}\right)^2 + \left(\tau_c^{\mathrm{GP}}\right)^2 + \left(\frac{\tau_s}{M}\right)^2} \qquad (3)$$

The resolution of the magnified ghost imaging system is illustrated in Fig. 5 as a function of the initial SC pulse duration ΔT_0 and for different values of the magnification factor. We can see that, for short initial durations (≤ 1 ps), it is the fluctuation time at the ghost plane τ_c^{GP} that determines the overall resolution of the imaging system. In contrast, for long SC pulse durations (≥ 100 ps), it is the time delay τ_s between the SC frequencies at the image plane that sets the temporal resolution. The response time of the detection system τ_d only has an effect for small magnification factors. The temporal resolution τ_R in the results of Fig. 4 is estimated to be 360 ps, determined both by the resolution of the detection system in the reference arm $\tau_d = 1.6\ ns$ and by the temporal spreading of the SC frequencies in the image plane $\tau_s \approx 0.8$ ns, the fluctuation time of the SC pulses at the ghost plane $\tau_c^{\mathrm{GP}} \approx 0.3$ ps having a negligible influence. The resolution of the imaging system is therefore improved by a factor τ_d/τ_R approximately equal to the magnification factor M compared to the standard ghost imaging setup.

5. CONCLUSIONS

Using dispersive spectrum-to-time transformation of the fluctuations of an incoherent supercontinuum we have demonstrated ghost imaging with magnification in the time domain. This approach can pave the way for overcoming the limited resolution of the standard time-domain ghost imaging whilst requiring only simple modifications of the experimental setup. We emphasize that the magnified approach demonstrated here is also insensitive to any distortion that would affect the light field after the object. Our results open novel perspectives for dynamic imaging of ultrafast waveforms with potential applications in communications and spectroscopy.

FUNDING INFORMATION

G. G. and A. T. F gratefully acknowledge support from the Academy of Finland (project 132279). J. M. D. acknowledges the ERC project MULTIWAVE.

See Supplement 1 for supporting content.

REFERENCES

1. B. I. Erkmen and J. H. Shapiro, "Ghost imaging: from quantum to classical to computational." Adv. Opt. Photonics **2**, 405–450 (2010).
2. R. S. Bennink, B. I. Bentley, R. W. Boyd, and J. C. Howell, "Quantum and classical coincidence imaging." Phys. Rev. Lett. **92**, 033601 (2004).
3. D. N. Klyshko, "A simple method of preparing pure states of an optical field, of implementing the einstein-podolsky-rosen experiment, and of demonstrating the complementarity principle." Sov. Phys. Usp. **31**, 74–85 (1988).

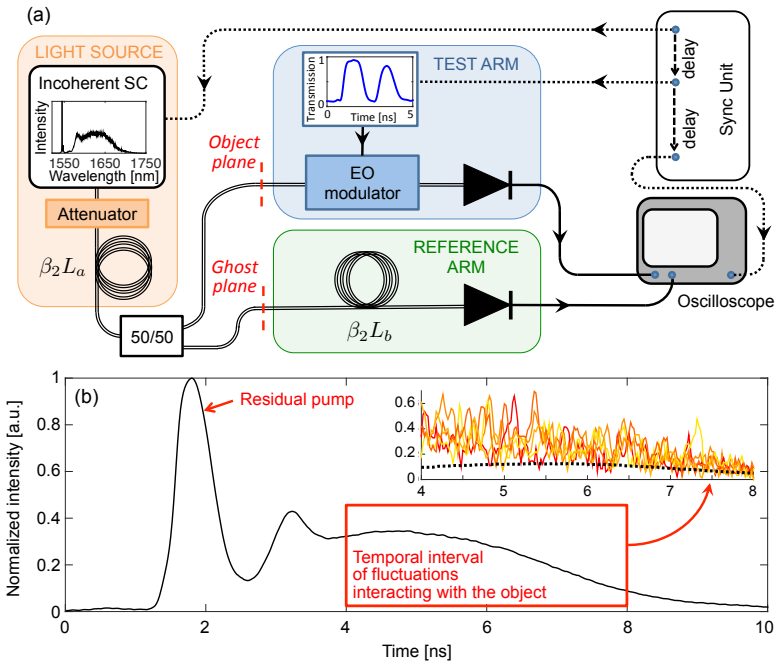

Fig. 3. Magnified time-domain ghost imaging experimental setup. (a) Setup. The synchronization unit allows to synchronize the electric signal driving the transmission function of the electro-optic (EO) modulator with the arrival time of the SC pulse at the modulator and trigger the oscilloscope. The inset in the "Light source" box shows the average SC spectrum as measured with an optical spectrum analyzer with 0.1-nm resolution. (b) Average of 10 000 temporal traces recorded (with a 12.5-GHz InGaAs photodiode, Electro-Optics Technology ET-3500F) at the ghost plane, showing that, after propagating in the 2.5-km fiber, the temporal profile of the SC reproduces its spectral shape (spectrum-to-time transformation). Inset: Examples of 5 distinct SC pulse traces recorded at the ghost plane together with the standard deviation (dotted black line) calculated over 10 000 realizations.

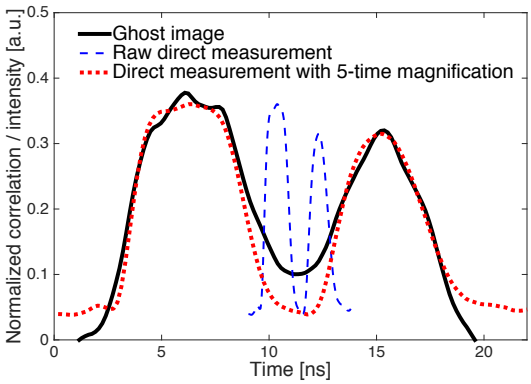

Fig. 4. Magnified ghost image obtained by correlating the signals of the test and reference arms over 100 000 supercontinuum pulses (solid black line). For comparison, the direct measurement of the temporal object (with a 5-GHz detector) is shown before (dashed blue line) and after (dotted red line) post- processed 5-time magnification.

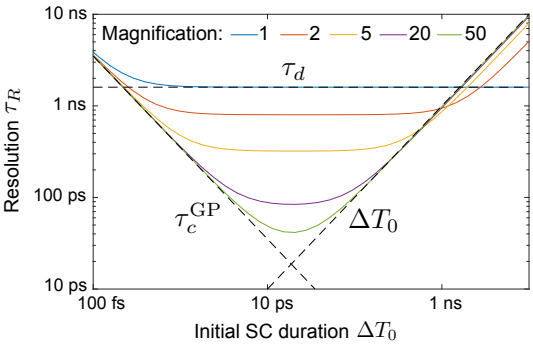

Fig. 5. Resolution of the magnified ghost imaging setup as a function of the supercontinuum initial duration and for various magnification factors. The time response of the detection system in the reference arm τ_d is taken to be 1.6 ns, and the characteristic fluctuation time of the supercontinuum pulses in the ghost plane τ_c^{GP} is set equal to 50 $ps^2/\Delta T_0$ (consistent with our experimental parameters). The dashed lines illustrates the different factors that limit the resolution (detector speed τ_d, characteristic time of fluctuations at the ghost plane τ_c^{GP} and initial duration of the SC pulses ΔT_0.

4. D. N. Klyshko, "Combine epr and two-slit experiments: Interference of advanced waves." Phys. Lett. A **132**, 299–304 (1988).
5. T. B. Pittman, Y. H. Shih, D. V. Strekalov, and A. V. Sergienko, "Optical imaging by means of two-photon quantum entanglement." Phys. Rev. A **52**, R3429 (1995).
6. A. F. Abouraddy, B. E. A. Saleh, A. V. Sergienko, and M. Teich, "Role of entanglement in two-photon imaging." Phys. Rev. Lett. **87**, 123602 (2001).
7. R. Bennink, S. J. Bentley, and B. R. W., ""two-photon" coincidence imaging with a classical source." Phys. Rev. Lett. **89**, 113601 (2002).
8. G. Scarcelli, V. Berardi, and Y. Shih, "Can two-photon correlation of chaotic light be considered as correlation of intensity fluctuations?" Phys. Rev. Lett. **96**, 063602 (2006).
9. R. Meyers, K. S. Deacon, and S. Y., "Ghost-imaging experiment by measuring reflected photons." Phys. Rev. A **77**, 041801 (2008).
10. T. Shirai, T. Setälä, and A. T. Friberg, "Ghost imaging of phase objects with classical incoherent light." Phys. Rev. A **84**, 041801 (2011).
11. C. Zhang, S. Guo, J. Cao, J. Guan, and F. Gao, "Object reconstitution using pseudo-inverse for ghost imaging." Opt. Express **22**, 30063–30073 (2014).
12. B. Sun, M. P. Edgar, R. Bowman, L. E. Vittert, S. Welsh, A. Bowman, and M. J. Padgett, "3d computational imaging with single-pixel detectors," Science **340**, 844–847 (2013).
13. D.-J. Zhang, H.-G. Li, Q.-L. Zhao, S. Wang, H.-B. Wang, J. Xiong, and K. Wang, "Wavelength-multiplexing ghost imaging," Phys. Rev. A **92**, 013823 (2015).
14. F. Devaux, P.-A. Moreau, S. Denis, and E. Lantz, "Computational temporal ghost imaging," Optica **3**, 698–701 (2016).
15. F. Ferri, D. Magatti, A. Gatti, M. Bache, E. Brambilla, and L. A. Lugiato, "High-resolution ghost image and ghost diffraction experiments with thermal light," Phys. Rev. Lett. **94**, 183602 (2005).
16. R. E. Meyers, K. S. Deacon, and Y. Shih, "Turbulence-free ghost imaging," Applied Physics Letters **98**, 111115 (2011).
17. P. Tournois, "Analogie optique de la compression d'impulsions." C. R. Acad. Sci. **258**, 3839 (1964).
18. B. H. Kolner and M. Nazarathy, "Temporal imaging with a time lens," Opt. Lett. **14**, 630–632 (1989).
19. B. H. Kolner, "Space-time duality and the theory of temporal imaging." IEEE J. Quant. Electron. **30**, 1951–1963 (1994).
20. R. Salem, M. A. Foster, and A. L. Gaeta, "Application of space–time duality to ultrahigh-speed optical signal processing," Adv. Opt. Photon. **5**, 274–317 (2013).
21. P. Ryczkowski, M. Barbier, A. T. Friberg, D. J. M., and G. G., "Ghost imaging in the time domain." Nat. Photon. **10**, 167–170 (2016).
22. K. Goda and B. Jalali, "Dispersive fourier transformation for fast continuous single-shot measurements." Nat. Photon. **7**, 102–112 (2013).
23. D. R. Solli, G. Herink, B. Jalali, and C. Ropers, "Fluctuations and correlations in modulation instability." Nature Photon. **6**, 463–468 (2012).
24. T. Shirai, T. Setälä, and F. A. T., "Temporal ghost imaging with classical non-stationary pulsed light." J. Opt. Soc. Am. B **27**, 2549–2555 (2010).
25. R. Salem, M. A. Foster, A. C. Turner, D. F. Geraghty, M. Lipson, and A. L. Gaeta, "Optical time lens based on four-wave mixing on a silicon chip," Opt. Lett. **33**, 1047–1049 (2008).
26. M. A. Foster, R. Salem, D. F. Geraghty, A. C. Turner-Foster,

M. Lipson, and A. L. Gaeta, "Silicon-chip-based ultrafast optical oscilloscope." Nature **456**, 81–84 (2008).
27. J. Schröder, F. Wang, A. Clarke, E. Ryckeboer, M. Pelusi, M. A. Roelens, and B. J. Eggleton, "Aberration-free ultra-fast optical oscilloscope using a four-wave mixing based time-lens," Optics Communications **283**, 2611 – 2614 (2010).

Tampereen teknillinen yliopisto
PL 527
33101 Tampere

Tampere University of Technology
P.O.B. 527
FI-33101 Tampere, Finland

ISBN 978-952-15-3815-5
ISSN 1459-2045